UNIVERSITÀ
DEGLI STUDI
DI PADOVA

University of Padova, Italy

Department of Industrial Engineering

SCHOOL OF DOCTORAL RESEARCH IN: Industrial Engineering

Address : Energy Engineering

CYCLE : XXVII°

Wireless Power Transfer for Electric Vehicle

Director of the School : **Ch.mo Prof. Paolo Colombo**

Coordinator : **Ch.ma Prof.ssa Luisa Rossetto**

Supervisor : **Ch.mo Prof. Giuseppe Buja**

Co-Supervisor : **Dr. Manuele Bertoluzzo**

PhD Student : **Kishore Naik Mude**

UNIVERSITÀ
DEGLI STUDI
DI PADOVA

Sede Amministrativa: Università degli Studi di Padova, Italy

Dipartimento di Ingegneria Industriale

SCUOLA DI DOTTORATO DI RICERCA IN : Ingegneria Industriale
INDIRIZZO: Ingegneria dell' Energia
CICLO: XXVII°

Wireless Power Transfer for Electric Vehicle

Direttore della Scuola	: Ch.mo Prof. Paolo Colombo	
Coordinatore d'indirizzo	: Ch.ma Prof.ssa Luisa Rossetto	
Supervisore	: Ch.mo Prof. Giuseppe Buja	
Co-supervisore	: Dr. Manuele Bertoluzzo	
	Dottorando	**: Kishore Naik Mude**

ABSTRACT

Wireless Power Transfer (WPT) systems transfer electric energy from a source to a load without any wired connection. WPTs are attractive for many industrial applications because of their advantages compared to the wired counterpart, such as no exposed wires, ease of charging, and fearless transmission of power in adverse environmental conditions. Adoption of WPTs to charge the on-board batteries of an electric vehicle (EV) has got attention from some companies, and efforts are being made for development and improvement of the various associated topologies. WPT is achieved through the affordable inductive coupling between two coils termed as transmitter and receiver coil. In EV charging applications, transmitter coils are buried in the road and receiver coils are placed in the vehicle. Inductive WPT of resonant type is commonly used for medium-high power transfer applications like EV charging because it exhibits a greater efficiency.

This thesis refers to a WPT system to charge the on-board batteries of an electric city-car considered as a study case. The electric city-car uses four series connected 12V, 100A·h VRLA batteries and two in-wheel motors fitted in the rear wheels, each of them able to develop a peak power of 4 kW to propel the car. The work done has been carried out mainly in three different stages; at first an overview on the wired EV battery chargers and the charging methodologies was carried out. Afterwards, background of different WPT technologies are discussed; a full set of Figures of Merit (FOM) have been defined and are used to characterize the resonant WPTs to the variations in resistive load and coupling coefficient. In the second stage, the WPT system for the study case has been designed. In the third stage, a prototypal of the WPT system has been developed and tested.

Design of the WPT system is started by assessing the parameters of the various sections and by estimating the impact of the parameters of the system on its performance. The design process of the coil-coupling has come after an analysis of different structures for the windings, namely helix and spiral, and different shapes for the magnetic core; further to the preliminary results that have shown the advantages of the spiral structure, a more detailed analysis has then been executed on this structure. The coil design has encompassed the determination of the inductive parameters of the two-coil coupling as a function of the coil distance and axial misalignment. Both the analysis and the design was assisted by a FEM-approach based on the COMSOL code.

Design of the power supply stages of the WPT system has consisted of the assessment of values and ratings of a) the capacitors that make resonant the coil-coupling, b) the power devices of the PFC rectifier and of the high frequency inverter (HF) that feeds the transmitting coil, c) the power devices of the converters supplied by the receiver coil: the rectifier diode and the in-cascade chopper that feeds the battery in a controlled way. For the converters that operate at high frequency (inverter and the rectifier in the receiver section), power electronic devices of the latest generation (the so-called Wide Band Gap (WBG) devices) have been used in order to maximize the efficiency of the WPT system.

A prototypal WPT battery charger was arranged by using available cards with the power and signal circuits. Relevant experimental activities were: a) measurement of the parameters of the coils, b) desk assembling of the prototype, and c) conducting tests to verify proper operation of the prototype.

The thesis work includes also a brief overview of i) emerging topics on WPT systems such as on-line electric vehicle (OLEV), ii) shielding of the magnetic fields produced by a WPT system, and iii) standards on WPT operation. These three issues play a significant role in the advancement of the WPT technology.

The thesis work has been carried out at the Laboratory of "Electric systems for automation and automotive" headed by Prof. Giuseppe Buja. The laboratory belongs to the Department of Industrial Engineering of the University of Padova, Italy.

SOMMARIO

I sistemi per il trasferimento di potenza wireless (WPT) trasferiscono energia elettrica da una sorgente ad un carico senza alcuna connessione via cavo. I sistemi WPT sono attraenti per molte applicazioni industriali grazie ai loro vantaggi rispetto alla controparte cablata, come l'assenza di conduttori esposti, la facilità di ricarica e la trasmissione senza rischi della potenza in condizioni ambientali avverse. L'adozione di sistemi WPT per la carica delle batterie di bordo di un veicolo elettrico (EV) ha ricevuto l'attenzione di alcune aziende, e sforzi sono stati fatti per lo sviluppo e il miglioramento delle varie topologie ad essi associate. Il WPT è ottenuto tramite l'accoppiamento induttivo tra due bobine, definite bobina trasmittente e bobina ricevente. Nelle applicazioni per la carica delle batterie, le bobine trasmittenti sono installate sotto il manto stradale mentre le bobine riceventi sono poste a bordo del veicolo. Il WPT induttivo di tipo risonante è comunemente utilizzato nelle applicazioni per il trasferimento di potenze medio-alte, come la carica degli EV, perché presenta una maggiore efficienza.

Questa tesi tratta un sistema WPT per caricare le batterie di bordo di una city-car elettrica considerato come caso di studio. La city-car elettrica utilizza quattro batterie da 12V, 100A·h VRLA collegate in serie e due motori-ruota montati sull'assale posteriore, ognuno in grado di sviluppare una potenza di picco di 4 kW per la propulsione del veicolo. Il lavoro svolto è stato effettuato principalmente in tre fasi diverse; in un primo momento è stata effettuata una panoramica sui caricabatteria cablati per EV e sulle metodologie di ricarica. Successivamente, sono stati discussi i principi base di diverse tecnologie WPT; è stato definito un insieme di figure di merito (FOM) che sono state utilizzate per caratterizzare il comportamento dei WPT risonanti rispetto alle variazioni di carico resistivo e al coefficiente di accoppiamento. Nella seconda fase, è stato progettato il sistema WPT per il caso di studio. Nella terza fase, è stato sviluppato e sperimentato un prototipo del sistema WPT.

La progettazione del sistema WPT è stata iniziata con una valutazione dei parametri delle varie sezioni e stimando l'impatto dei parametri del sistema sulle sue prestazioni. La progettazione della bobina di accoppiamento è stata effettuata dopo l'analisi di avvolgimenti con strutture diverse, ovvero elica e spirale, e con forme differenti del nucleo magnetico; a seguito dei risultati preliminari che hanno mostrato i vantaggi della struttura a spirale, è stata poi eseguita un'analisi più dettagliata su questa struttura. Il progetto della bobina ha compreso la determinazione dei parametri induttivi dell'accoppiamento in funzione della distanza e del disallineamento assiale delle bobine. Sia l'analisi che la progettazione sono state assistite da un approccio FEM basato sul codice COMSOL.

La progettazione degli stadi di alimentazione del sistema WPT è consistita nella valutazione dei valori e dei dati di targa di a) i condensatori che rendono risonante l'accoppiamento tra le bobine, b) i dispositivi di potenza del raddrizzatore PFC e dell'inverter ad alta frequenza (HF) che alimenta la bobina di trasmissione, c) i dispositivi di potenza dei convertitori alimentati dalla bobina ricevente, segnatamente il raddrizzatore a diodi e il chopper collegato a valle che carica la batteria in modo controllato. Per i convertitori che operano ad alta frequenza (l'invertitore e il raddrizzatore della sezione ricevente), sono stati utilizzati dispositivi elettronici di potenza di ultima generazione (i cosiddetti dispositivi Wide Band Gap (WBG)) al fine di massimizzare l'efficienza del sistema WPT.

E' stato realizzato un caricabatteria WPT prototipale utilizzando schede elettroniche disponibili in Laboratorio con i circuiti di potenza e di segnale. Le relative attività sperimentali sono state: a) misurazione dei parametri delle bobine, b) assemblaggio a banco del prototipo, e c) esecuzione di prove sperimentali per verificare il corretto funzionamento del prototipo.

Il lavoro di tesi comprende anche una breve panoramica su temi emergenti in materia di sistemi WPT come i) IL WPT dinamico, chiamato anche “on-line electric vehicle” (OLEV), ii) la schermatura dei campi magnetici prodotti da un sistema WPT, e iii) la normativa sui sistemi WPT. Questi tre temi svolgono un ruolo significativo nello sviluppo della tecnologia WPT.

Il lavoro di tesi è stato effettuato presso il Laboratorio di “Sistemi elettrici per l'automazione e la veicolistica” diretto dal Prof. Giuseppe Buja. Il Laboratorio fa parte del Dipartimento di Ingegneria Industriale dell'Università degli Studi di Padova, Italia.

Dedicated to my parents

Acknowledgement

I would like to express my deepest gratitude to each and every one who helped me with their continuous support during my doctoral work. Even though it is not possible to wrap the support of my supervisors with words, I take this opportunity to thank Prof. Giuseppe Buja, who has been constant source of inspiration and guidance, without whom successful completion of the work for the thesis would not have been feasible. I am also grateful to my co-supervisor Dr. Manuele Bertoluzzo for his invaluable guidance, motivation, support, advice. Their meticulous guidance, constructive and valuable suggestions, timely discussions and clarifications of my doubts increased my cognitive awareness and helped me for making a deeper analysis of the subject.

I am grateful to Cassa di Risparmio Padova e Rovigo (CARIPARO) foundation for the financial support throughout the course. My sincere appreciations to Prof. Colombo, Prof. Luisa Rosetto, Prof. Martinelli, and administrative staffs of the department and the University for their support. I have always found them responsive and supportive not only to me but to all the students, contributing towards an excellent world class research environment. I am also thankful to all the non-teaching technical staffs of the department for their assistance bestowed.

I am grateful to my colleague Dr. Ritesh Keshri who inspired me in so many ways. I truly appreciate his patience, helpfulness and encouragement in every aspect of life. I would like to extend my salute and thanks to all my colleague students, Nicola Ganeo, Davide, Nima Zabihi, Cristian, Marco, Syamnaresh, Kundan and Hemanth for their professionalism, company and respect during group work and social activities. I acknowledge an appreciation that extends beyond any words for the love and support of my friends, particularly all CARIPAROs. I extend my deep sense of gratitude towards them. Also I wholeheartedly thank the Indian community who made my stay at Padova memorable and pleasant.

In addition, I would like to thanks all my Italian friends specially Maria Chiara Sisino (Mary), who always remained supportive and caring during my stay at Padova. I am especially indebted to my family members for their patience and moral support during my doctoral work. Last but not the least, I am beholden to all those who helped me directly and indirectly in my work.

Contents

Chapter 1

Introduction

1.1. Background

Growing concern in the reduction of the polluting emissions due to the transportation means has led to the adoption of vehicles powered by comparatively cleaner sources of energy, such as batteries, fuel cells and so on, in place of internal combustion engine (ICE) based vehicles. Differently from ICE vehicles, electric vehicles (EVs) are not a matured technology in terms of vehicle autonomy, and a lot of research efforts is being carried out by academia and industries to improve the overall performance of the these vehicles. Various solutions are being adopted to increase the autonomy of the vehicles such as conceiving batteries of higher energy density, relaxing the batteries during acceleration and regeneration by supplying and absorbing the current peaks by means of supercapacitors, arranging fast chargers, charging while on move etc. On-board batteries are typically recharged at home or at stations/parking places through conductive battery chargers. Generally two types of conductive battery chargers are used: off-board and on-board. On-board chargers can be used to charge from the utility outlet at home or at charging stations during the day time. Off-board chargers operate like a gas station and are designed to manage high powers in order to perform a fast charge.

In most of the battery chargers the power flows only from the utility grid to the battery, and for this reason they are often termed as unidirectional battery chargers (UBCs); beside circuital simplicity, UBCs enjoy a reduced grid interconnection and lower battery degradation. On other hand, some battery chargers manages power flowing in both directions and are able to perform ancillary operation in favor of the grid, such as peak power shaving or reactive power compensation. These battery chargers are called bidirectional battery chargers (BBCs).

Charging of an electric vehicle can be performed by either conductive (or wired) charging or wireless charging. Wired charging uses connection means between electric supply and charge inlet of the vehicle. Even though wired charging is popular, the problems with messy wires and safety matter in wet environment are a major drawback of this charging. Since a few years, a large interest is growing for the supply of the electric loads through a field to dispense from any wired connection with the grid. The apparatuses that actuate the through-the-field supply are termed as wireless power transfer systems (WPTSs). Their deployment has started for the recharge of the batteries that are fitted in grid-detachable equipment. Recharging is executed while the equipment is standing in an on-purpose set but the long-time perspective is the supply of equipment while moving, with the purpose of removing the batteries or at least of reducing their capacity. Wireless charging of the EV batteries offers a number of advantages compared to the wired counterpart; indeed, wireless charging makes it i) unnecessary any plug, cable or outlet, ii) friendly the charging process, iii) fearless the transfer of energy in any environmental condition, and so on. For these reasons, WPTSs are expected to play a major role in the future charging process for the EVs.

Three different technologies can be utilized to arrange a WPTS, exploiting the properties of the electric, magnetic and electromagnetic fields. Magnetic-field technology, adopted in the so-called inductive WPTSs, is the most convenient one because it transfers much higher energy per unit of volume than the electric-field technology, and does it with much higher efficiency than the electromagnetic-field technology. As a matter of fact, low-power inductive WPTS with closely coupled coils are around since a few years. In recent times,

however, interest is arisen in transferring energy at medium-high power to an equipment at a somewhat far distance. For these applications, inductive WPTSs with resonant topology (shortly, resonant WPTSs) are used. This, for instance, is the case of the wireless charging of the EV batteries.

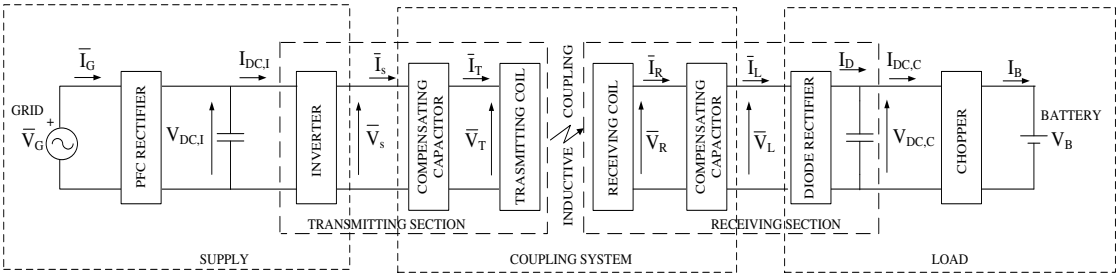

Fig.1.1. General scheme of a resonant WPTS.

The general scheme of a resonant WPTS is shown in Fig.1.1. It consists of two sections: transmitting and receiving, each of them including a coil that is coupled to the other one with a large air-gap in between. Both the WPTS sections are equipped with power conversion circuitry. On the transmitting section, the grid feeds the relevant coil through a diode rectifier with output capacitor and an in-cascade inverter operating at high frequency. Grid, rectifier and battery constitute the supply of the transmitting coil and are equivalent to a sinusoidal generator with an in-series resistance, where the frequency of the generator is the inverter frequency. To achieve a good power factor, the diode rectifier is normally substituted for by a PFC rectifier. On the receiving section, the voltage induced across the receiving coil charges the battery pack through another capacitor-output diode rectifier and an in-cascade chopper, which adapts its output current/voltage to the battery charging requirements. Rectifier, chopper and battery constitute the load of the receiving coil and are equivalent to a resistance.

Coupling structure crucially affects the performance of a WPT system. Various coil arrangements are documented in literature but two arrangements are frequently used in EV charging applications, namely helix and spiral. Spiral coils can take many forms with rectangular and circular turns, and offer more flexibility for optimizing the coil geometry, what makes them particularly attractive for EV charging applications. Coil alignment is one of the major issue for WPT. Because of the tolerance in the vehicle parking maneuver, the receiving coil may be not perfectly aligned with the transmitting coil during EV charging process. This reduces the coupling coefficient compared to that one in aligned conditions with a consequent decrease of the efficiency in the power transfer.

By the resonant topology, the inductances of the coils are compensated for by capacitors inserted either in series or in parallel to the coils and tuned to make resonant the coil-capacitor branches at the supply frequency. Four basic topologies of resonant WPTSs can be found: series-series (SS), series-parallel (SP), parallel-series (PS) and parallel-parallel (PP), depending on the connection (series or parallel) of the capacitors with respect to the coils in the two sections of the WPTS.

Operation of a WPTS requires power electronics circuitry. The power circuitry supplying the transmitting coil includes a high-frequency inverter and a diode rectifier that also works at high frequency. High-frequency operation is conveniently implemented by

using new generation devices like SiC/GaN to keep high the efficiency of the system. DC voltage across the output capacitor of the rectifier in the receiving section is controlled by acting on the magnitude of the output voltage of the inverter placed in the transmitting section.

Emerging issues in wireless power charging of the EVs are i) dynamic (or on-line) charging, ii) shielding the magnetic fields nearby the WPTSs, and iii) standards under issue to regulate the setup of the WPTS. Online charging is a technique to charge the battery of an EV while the vehicle is in motion, with the transmitter that is formed by tracks embedded in the ground. The Korean Advanced Institute of Science and Technology (KAIST) introduced dynamic charging, termed by its researchers as OnLine EV (OLEV) charging technology, in a commercial application (the zoo of Seoul). Shielding of the magnetic field out of the transmitting coil is a significant issue to be faced in a WPTS to protect the biological organs from its effects; two types of shielding are commonly used for this purpose, i.e. passive and active shielding.

1.2. Objective of the thesis

- Development of WPT charger for an electric city-car situated in the Laboratory of Electric Systems for Automation and Automotive of the Department of Industrial Engineering, University of Padova, where I have developed my thesis. The electric city-car was taken as the study case.
- Design and analysis of coil system with helix and spiral coil and with different shapes for the magnetic core to evaluate their inductive characteristics.
- Study of the power circuitry for the WPTS.
- Demonstration of the WPT charger for city-car by building a prototype.

1.3. Organization of thesis

The thesis is organized in eleven Chapters whose outline is given below.

This Chapter summarizes background and objective of thesis.

Chapter 2 presents today's and future scenarios of EVs and the characteristics of the lithium batteries used in the EVs. Moreover, it illustrates the battery charging modes and the conventional battery chargers. At last the WPT charging for the EVs is introduced.

Chapter 3 deals with the potential technologies for the WPT, showing the convenience of the inductive one. Four figure of merits (FOMs) for inductive and resonant WPTS are then formulated and, from the formulation, impact of the parameters of the WPTS on its performance is derived.

Chapter 4 is concerned with the analysis, assisted by FEM code, of the inductive characteristics of the helix and spiral coil-coupling, and on their dependence on the coil misalignment. Further to the analysis, the coil-coupling for the study case is designed.

Chapter 5 considers three different shapes of core (I, C and E) made of ferrite and analyzes their influence on the inductive characteristics for the spiral coil designed in the chapter 4. This chapter also investigates the magnetic field around the coils.

Chapter 6 finds out the FOM expressions and values for the four resonant topologies. Study of FOMs with varying load and varying coupling coefficient is also executed.

Chapter 7 refers to power requirements for the WPTS. It describes the advantages of the WBG devices over the conventional ones. Topology and control of the high-frequency inverter and the PFC rectifier in the transmitting section and of the chopper in the receiving section are described.

Chapter 8 reports the implementation and experimental results of the WPTS prototype.

Chapter 9 gives an overview on the on-line wireless charging.

Chapter 10 discusses about the two types of magnetic shielding.

Chapter 11 addresses the existing standards on WPTS.

A review on magnetic materials for the coil core, data on the electric city-car and an outline on the inductive sensing technology are reported in Appendixes A, B and C, respectively.

Chapter 2

Electric vehicles and battery chargers

Summary

Purely Electric Vehicles (EV) can be operated by battery or fuel cell. When operated by battery, it is recharged by grid supply. In the present global scenario, EVs have most encouraging support because of the facts that these ensure zero-emission with lower operating and maintenance cost, and apart from the grid energy these are able to use recovered energy during regenerative braking for range extension. In an electric vehicle energy required for propulsion as well as for supporting other on-board utilities is carried in on-board batteries, so has major consequences for the vehicle design and performance around it [1].

Battery chargers play an important role in the development of EVs. Charging time and battery life are linked to the characteristics of the battery charger. A battery charger must be efficient and reliable, with high power density, low cost, low volume and weight. Its operation depends on components, control and switching strategies, specific integrated circuits, rating, cost, and types of converter. An EV charger must ensure that the utility current is drawn with low distortion to minimize power quality impact and at high power factor to maximize the real power available from a utility outlet. IEEE-1547 [2], SAE-J2894 [3].

For energy storage, it is clear that the energy density of fossil fuels is order of magnitude greater than that of the battery technologies available today. For the batteries a utilization factor has to be taken into account, as it is good practice to limit the depth of discharge to 80% of the nominal battery capacity in order to achieve an acceptable life. The efficiency of the all-electric cars is much better than that of a petrol or diesel internal combustion engine (ICE), about a factor of four.

Current scenario on electric vehicles and battery chargers provides many important conclusions. Many prominent automotive manufacturers are currently engaged in the research and development of new electric vehicles. Research conducted by Pearre [4] suggests that current EV technology is already sufficient to meet the driving needs of a large portion of drivers, although Franke [5] indicates that range limitations of current EV models are still a psychological barrier to public acceptance on a large scale. In this chapter overview of electric vehicle and conventional battery chargers is reported.

2.1 Introduction to Electric vehicle

Electric vehicles are not a new and have been around since the beginning of early 19^{th} century. However with the advent of internal combustion engine and cheap oil in the early 20^{th} century, the EVs went out of mass production. The EVs also grew unpopular because of their very limited driving range. But the idea of an environment friendly, and affordable EV has not vanished. Limited range and cost have been major obstacles that limit the use of EVs on a large scale. However, with the development of Li-ion batteries, fast charging infrastructure and lower cost of production, EVs can become a realistic alternative to conventional vehicles. Charge replenishment of EVs has been traditionally done via conductive charging.

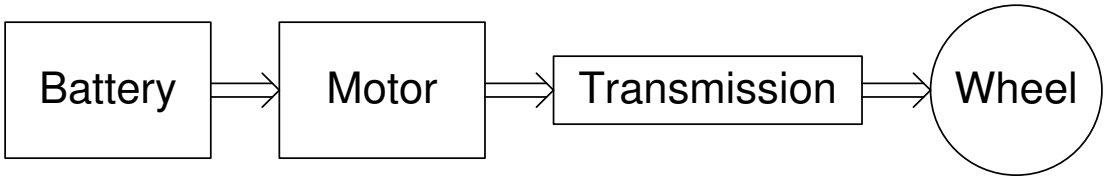

Figure.2.1 Schematic diagram of EV system

In present years, a good improvement in electric vehicle (EV) has arisen globally due to the stressing of the environmental concerns and increasing price of oil. These vehicles with on-board energy storage devices and electric drives allow power to be recovered, thus improving fuel economy and reducing pollutants. As a product of advanced design philosophy and component technology, maturing and commercialization of EV technologies demand extensive research and developments.

2.1.1 Present & future scenario of electric vehicle

Currently, electric vehicles represent a small part of all passenger vehicles in most jurisdictions globally. However, it has become widely accepted that rapid growth in the electric vehicle market will take place within the coming decades [6]. A 2009 study conducted by JP Morgan estimated that 11 million electric vehicles could be sold worldwide by 2020; this growth would represent a nearly 20% share in North America's passenger vehicle market and 13% globally at that point in time. Hybrid gasoline-electric vehicles (HEVs), like Toyota Prius, are gaining a foothold in the current automotive market, with several models offered by most mainstream vehicle manufacturers.

Despite the low environmental impact and high energy efficiency, EVs have not been widely accepted by people to date. The lack of charging infrastructure is one of the reasons. The charging infrastructure requires a major investment on the part of both the government and the private sector. There are some barriers to infrastructure installation such as codes and standards, installation costs, utility infrastructure planning, construction, consumer knowledge, metering, contractor role, and permitting procedures, etc. There is much uncertainty on the impact of the smart grid on EV batteries and EV charging infrastructure.

Home charging will be important for achieving high rates of EV development, public charging is more important for moving past the very early stages of EV adoption. This infrastructure is the most economical because it does not need a wall inlet. The need for recharging in the community and on highways with preferably fast charging mode is essential for mass commercialization. The extra cost of redundant power electronics is likely to drive continued innovation in integrated charging. Topologies that cannot develop motor torque are probably essential, as extra mechanical complexity will preclude any approach that does. Economic questions, such as data-exchange standards for billing, must be addressed in the future to allow vehicles to charge at flexible locations, with integrated charging, metering and billing data exchange must be built into the vehicle as well. While many observers mention bidirectional chargers, unidirectional configurations support nearly the same functionality without issues of back feed, safety, and islanding protection [7], [8]. It is likely that unidirectional charging

will be the primary avenue for development in the near future, even though many integrated charging configurations support bidirectional energy flow. Developing a charging infrastructure and associated electric vehicle supply equipment (EVSE) is perhaps the most important consideration. Necessary parts include conductors, EV connectors, attachment plugs, devices, power outlets. Charging systems that can accommodate high-power charging will provide more flexibility and choices to the EV.

2.1.2 Advantages & Disadvantages of Electrical vehicle (EV)

The demand for electrical vehicle is growing day by day as it offers most advantages than conventional vehicle (CV)

Advantages

(a) Lower energy consumption: If one considers only the vehicle itself, EVs are far more energy efficient than CVs. For the electrical vehicle about 86% of the electricity used to charge the battery is used to power the cars motor [6]. Most CVs however convert only about 20% of the energy in gasoline into engine output energy. On the other hand, loss of energy for generating electricity from a primary source of energy (such as hydroelectric plant or a coal plant) and transporting it to an electrical outlet is much greater than the energy loss from extracting, refining and delivering petroleum fuel to a car.

(b) Lower the fuel dependency: EVs can reduce fuel costs dramatically because of the low cost of electricity relative to conventional fuel. As they rely in whole or part on electric power, their fuel economy is measured differently than in conventional vehicles. Electrification of transport would help reduce this dependency.

(c) Environment friendly: The increasing use of EV would have significant positive impact on the environment because of the reduction of overall energy consumption and air pollution.

(d) Recyclable: Almost 100 percent of these batteries can be recycled, which keeps old batteries from becoming a disposal problem.

(e) No noise: Electrical motors provide, quiet, smooth operation and stronger acceleration and necessitate fewer maintenance compared to internal combustion motors.

Disadvantages

(a) Wastage of fossil fuels: The electricity used to recharge EV batteries has to come from somewhere (coal, hydro) and, right now most electricity is generated by burning fossil fuels.

(b) Consumption of time: Electrical vehicles consume more time to recharge battery. Battery can charge overnight, still it is not convenient as much as conventional vehicles

(c) More weight and space: Batteries have certain weight. Because they need to do more

than traditional engine-starting car batteries, traction batteries need to be linked together into arrays, or battery packs, to provide additional power. These collections of batteries are heavy, and require space.

2.2 Overview of batteries

The challenge of transforming EVs from concept to reality is to make it safe, convenient and easy for consumers to charge batteries. As an EV is usually parked at home or a storage site at night, the battery charger in the vehicle can be connected into the domestic single-phase AC plug for slow night-time charging. Depending on the battery capacity and depth of discharge, the charging time takes about 6-8 h, and the charging current is usually limited to 15 A.

Battery is a key component for any kind of pure electric vehicle, since to date it is, together with fuel cell supply, the only device that can store enough electric energy to give the vehicle a reasonable driving range. In simple terms, a battery is a device that converts chemical energy to electric energy. The basic element of any battery is called a "cell", and is typically constituted by two electrodes and the electrolyte; the chemical reaction between the electrodes and the electrolyte is responsible for the generation of electricity. In most batteries (secondary batteries, or re chargeable batteries), the chemical reaction can be reversed, and electrical energy can be stored into chemical form, charging the battery. For traction applications, the most important functional parameters for a battery are specific energy, specific power, cell voltage, efficiency, operating temperature, self-discharging rate, life time, lifecycle, recharging rate, and mass (unit of volume).

In addition to the functional requirements, safety and cost also play a key role in the choice of the most suitable battery for a particular application. The best known and most widely used battery for traction systems is the lead acid battery. Although those batteries have a long history and their technology is quite mature, achievable performance does not quite match the requirements of an electric vehicle. In particular, specific energy is typically limited to about 30 Wh/kg, making it virtually impossible to achieve a driving range of few hundred kilometers for an EV that would use such a battery as main energy storage. Moreover, the cycle life of lead acid batteries is relatively poor, if deep discharge is required. On the other hand, cost is quite low and no particular safety issues exist related to the use of those batteries for high power, traction applications.

2.2.1 Types of batteries

There are several different types of electric car batteries as below [6]

(a) Lead-acid batteries: These are the most widely available, as both battery product and manufacturing process are proven, economical and reliable. There are concerns however, over their disposal. Lead-acid battery recycling is popular although an effective pollution control system is needed to reduce emissions, but due to their larger weight, it cannot support portability

(b) Nickel metal hydride batteries: These have a higher energy density than lead-acid batteries. The energy density for nickel metal hydride batteries is approximately 69.4 Wh/kg and these batteries have been used in many all-electric plug-in vehicles including the Toyota RAV4 EV, General Motors EV1 and Honda EV Plus. They have also been used in hybrid vehicles including Toyota Prius and Honda Civic Hybrid. Generally they have a lower environmental impact than nickel-cadmium batteries due to the absence of the toxic cadmium. Most industrial nickel is also recycled due to its high value.

(c) Lithium-ion batteries: Lithium-ion batteries are widely preferred for electric car use due to their superior range per charge. They are also less expensive than nickel and they have a low discharge rate of approximately five per cent per month compared to 30 per cent per month from nickel-metal hydride batteries. To prolong the life of a lithium-ion batteries, they should be charged early and often they should never be depleted below their minimum voltage and they should be kept cool. Different battery chargers compared in Tab 2.1

Table 2.1. Comparison of different batteries [6]

Parameters	Lead acid	NiMH	Li-ion
Nominal cell voltage (V)	2.1	1.2	3.6
Specific energy (Wh/kg)	30-40	50-80	150-250
Specific power (W/kg)	250	<1000	<2000
Energy density (Wh/l)	50-90	150-200	150-250
Charge/discharge efficiency (%)	70-92	66	98

2.3 Power electronic converters for battery chargers

The power electronics circuitry for battery chargers consist of an AC-DC converter followed by a DC-DC converter. The AC-DC converter rectifies the AC voltage from the power grid to a DC voltage. The DC-DC controls the voltage/current supplied to the battery according to its charging profile. In most of commercially available battery charger (BC), the two stages are separated by an insulation stage formed by a high-frequency inverter, a coupling transformer and a high-frequency rectifier, as shown in Fig. 2.2.

The simplest AC-DC power converter uses diodes as rectifying components. It is simple, cheap and can be realized both in single phase and three phase versions, however, the currents drawn from the grid are highly distorted and additional input filters are required to comply with the rules about harmonic injection in the grid. For high power battery charger the use of input filters is not viable and hence more sophisticated AC/DC converter must be used.

Power Factor Correction (PFC) circuits, shown in Fig. 2.3, are used for the single-phase BCs. They control the current absorbed from the grid to be nearly sinusoidal and in phase with the voltage and, at the same time, regulates the output voltage of the rectifier. They suf-

fer the draw backs of needing an output voltage higher than peak grid voltage and of being unable to manage bidirectional power flow.

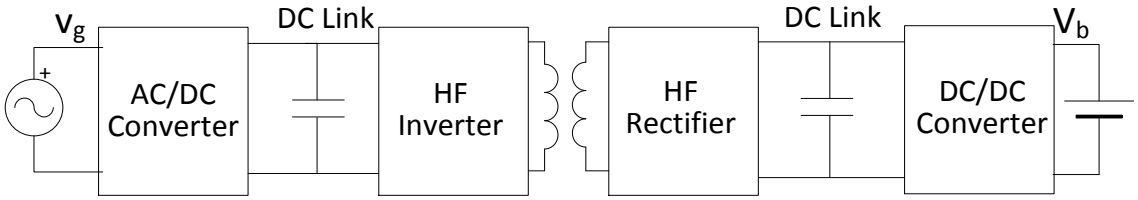

Fig. 2.2. Scheme of principle for battery chargers

For three phase BC the input state is usually formed by an active rectifier. It is capable of managing bidirectional power flows and absorbs sinusoidal current with adjustable power factor so that it can be used for BBC and to perform V2G operations.

2.3.1 Conventional Battery Chargers (CBCs)

There are mainly two types of CBCs are available: unidirectional battery chargers and bi-directional battery chargers.

(a) Unidirectional battery chargers

These battery chargers charge the battery in single direction only. EVs with unidirectional batteries can be charged, but cannot inject the power to grid. These chargers normally use a diode bridge together with a filter and dc-dc converters. These converters are only implemented in single phase supply to lower the cost and size of the equipment.

(b) Bi-directional battery chargers

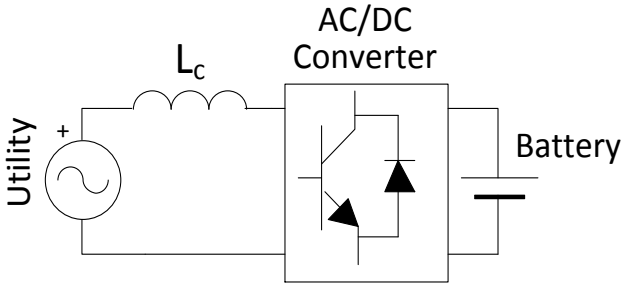

Figure 2.3. Schematic of bidirectional battery chargers [8]

Typical bidirectional charger has two stages an active grid-connected bidirectional ac-dc converter that enforces power factor, and a dc-dc converter to match battery voltage [7], [8]. These chargers can use isolated (or) non-isolated circuit configurations. When operating in charge mode, they draw a sinusoidal current. In discharge mode, the charger should return current in a similar sinusoidal form [9], [10]. A bidirectional charger supports charge from

the grid, battery energy injection back to the grid, referred to as vehicle-to-grid (V2G) operation mode, and power stabilization.

While most studies have focused on bidirectional power flow, there are serious challenges for adoption [11]. Bidirectional power flow must overcome battery degradation due to frequent cycling, the premium cost of a charger with bidirectional power flow capability, metering issues, and necessary distribution system upgrades. Customers are likely to require an energy guarantee to ensure that vehicle state-of-charge is predictable (and high) when it is time to drive. Successful implementation of bidirectional power flow will require extensive safety measures. Anti-islanding protection and other interconnection issues must also be addressed.

2.4 Modes of charging

Depending on the supplied power level and on the charging time, EV charging is classified into Mode1, Mode 2, Mode 3 and Mode 4 [12]

Mode 1: This is the cheapest and most convenient home-based charging method, but it is also the slowest. EVs are equipped with on-board battery charger, as well as with cords that allow the vehicle users to plug their car into an outlet in their garage. According to mode 1, EVs can be charged from standard 230 V household outlet but the supplied current is limited to 16 A. Charging times vary greatly from vehicle to vehicle, but generally take around 7-15 hours for a fully depleted battery of a compact electric car to recover its full capacity. Mode 1 uses standard industrial plugs and sockets for the connection of the EV to the outlet. In USA this mode of charging is prohibited because it requires earth connection that is not a standard feature in USA domestic electric plants.

Mode 2: This charging method relies on 230 V or 440 V, single phase or three phase ac mains not exceeding 32 A. Like Mode1, dedicated plugs and socket are not required to connect EVs to wall boxes installed in the garages or to charging stations located in public places, such as at the shopping mall, restaurant, city park, or even workplaces. Charging boxes and/or charging stations and the on-board battery charger contain the circuitry needed to perform safety functions such as i) verification that the vehicle is properly connected, ii) continuous checking of the continuity of the protective earth conductor, iii) energization of the system iv) de-energization of the system. Mode 2 charging is generally referred to as “opportunity charging” because vehicle user usually use this type of charging whenever they have the chance. Mode 2 charging takes around 3-5 hours for a full charge of a compact car.

Mode 3: It typically operates with three phase 440 V ac mains and supplies up to 63 kW to the on board battery charger by means of dedicated plugs and sockets. Besides safety functions of Mode 2, charging stations and on board battery chargers implement suitable protocols to synchronize their operation. As a result of the higher available power, a mode 3 charge provides a compact vehicle with a full charge in less than an hour. Mode 3 charge is used large vehicles like electric buses, and is available in public and commercial areas, airports, and transportation corridors [9].

Mode 4: In Mode 4 ac mains voltage is converted in dc voltage by a rectifier installed in the charging station. An off-board battery chargers supplies up to 400 A to the EV by means of a dedicated plug. The Japanese standard "CHAdeMO" is the most diffused implementation of mode 4 charging. It charges a compact car in less than 30 minutes supplying a power of up to 50 kW.

2.5 WPTS technology for electric vehicle

General Motors in 1996 and in 1997 introduced two EVs namely EV1 and Chevrolet S-10 EV were using Magne Charger, also known as J1773 that used the principle of inductive power transfer. Instead of a plug, a "pad" as containing the primary coil is inserted in slot in the EV. The slot contains the secondary coil and together with the pad, a Wireless Power Transfer (WPT), transformer was formed. The performance of these pads was not too promising. These pads also had to be manually inserted in the EV and hence were as inconvenient as the traditional plugs. However, with increasing interest in e-mobility in recent times, a lot of research interest is being shown to make EVs a good option for future transportation. WPT charging technology has the potential to bring about a positive change in mindset of people regarding EVs. It is expensive with limited driving range, inconvenient with respect to the charging process. However, with introduction of WPT technology for charge replenishment, EVs can become an attractive option. WPT charging has the advantage that it can make the charging process automated, convenient and safe for users and large scale introduction of WPT charging infrastructure can help reduce the battery pack size and in turn make the EVs more efficient. However, all this cannot be accomplished by using traditional inductive chargers and WPT charging through large air gaps and least possible human interaction are required. In recent years, some of the major manufacturers GM, Qualcomm halo, Delphi, Toyota etc. have shown interest in wireless charging technology and recently Qualcomm introduced WPT technology to EV. Also different research groups in various universities are pursuing research in this field. Fig 2.4 shows WPT charging system for EV application. The primary winding of the WPT system is connected to grid via converter system, is buried in the ground, and transfers the power to secondary winding of WPT system. The secondary is located in electrical vehicle and, charging circuit performs the charging battery.

2.6 Conclusion

This chapter deals with the basic overview of present and future scenario of electric vehicles. After discussing the scenario, various concerns about types of battery and charging methodologies were discussed. Basics of CBC's used for battery charging are also discussed and at last the need of WPT technology for EV is studied.

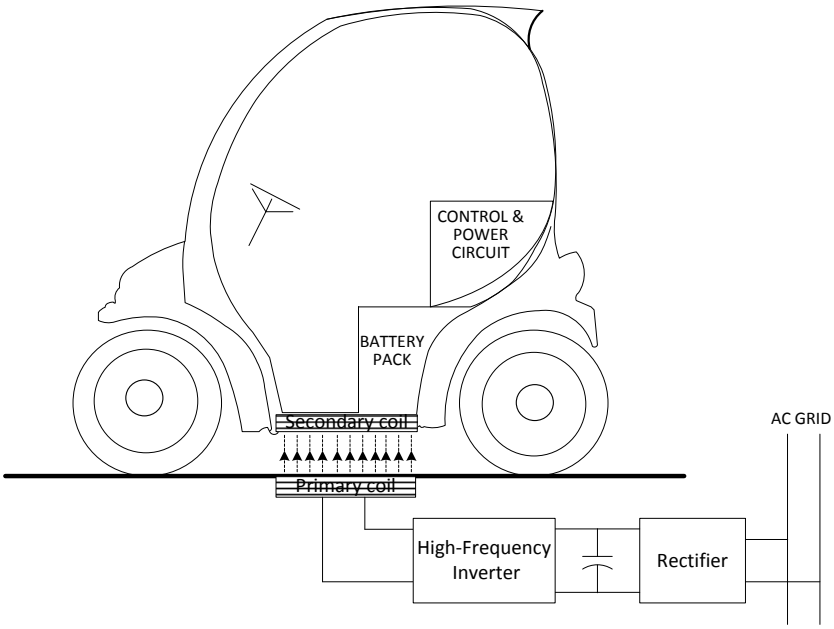

Figure 2.4 Schematics of WPT for electrical vehicle battery charging

2.7 References

[1] C.C.Chan, ‘‘The state of the art of electric, hybrid, and fuel cell vehicles,” *Proc of IEEE*, vol. 95, no. 4, pp. 704-718, 2007

[2] IEEE for Interconnecting Distributed Resources with Electric Power Systems, IEEE-1547, 2003.

[3] Power Quality Requirements for Plug-in Vehicle Chargers - Part 1: Requirements, SAE International, Standard J2894, 2011.

[4] N.S.Pearre, W.Kempton, R.Guensler, and V.V.Elango “Electric vehicles: How much range is required for a day’s driving?,” Transportation Research Part C, vol.19, no.6, pp.1171-1184, Dec 2011.

[5] T.Franke, I.Neumann, F.Bühler, P.Cocron, and J.F.Krems “Experiencing range in an electric vehicle - understanding psychological barriers,” Applied Psychology: An International Review, pp.1-6, August 2011.

[6] ec.europa.eu/clima/policies/transport/vehicles/docs/d1_en.pdf.[online], Accessed: 27/09/2012,

[7] Portland General Electric, “Plug-in Vehicle Charging Stations Electric Vehicle Charging Stations,” [online], Accessed: 05/10/2012.

[8] M.Bertoluzzo, N.Zabihi, and G.Buja “Overview on Battery Chargers for Plug-in Electric Vehicles,” Proc. of 15th International Power Electronics and Motion Control Conference (EPE-PEMC 2012 ECCE), 2012, pp.1-7.

[9] H.Chen, X.Wang, and A.Khaligh, “A Single Stage Integrated Bidirectional AC/DC and DC/DC Converter for Plug-in Hybrid Electric Vehicles,” Proc. IEEE Vehicle Power

and Propulsion Conference, 2011, pp.1-6.

[10] J.Tomic and W. Kempton, “Using fleets of electric-drive vehicles for grid support,” Power Sources, vol. 168, no. 2, pp. 459–468, 2007.

[11] M.C.Kisacikoglu, B.Ozpineci and L.M.Tolbert, “Examination of a PHEV bidirectional charger system for V2G reactive power compensation”, Proc. of IEEE Applied Power Electronics Conf. and Exposition, 2010, pp. 458-464.

[12] http://en.wikipedia.org/wiki/SAE_J1772. Retrieved on 13/10/2012.

Chapter 3

Wireless Power Transfer System (WPTS): Background

Summary

A WPTS has the structure of Fig 3.1. It is made of two power sections electrically insulated: the transmitter and the receiver. The transmitter is buried into the pavement and is fed by the mains, the receiver is embedded into the electric vehicle and delivers power to the battery pack on board the vehicle, the latter one constitutes the load of the WPTS and is represented by a resistor in Fig 3.1. Each section of WPTS consists of a coupling device and a power converter. The coupling device of the transmitter (briefly, the transmitting device) generates an alternating field that can be either electric or magnetic or electromagnetic. Actually, any alternating electric field is associated to an alternating magnetic field and vice-versa so that the above distinctions may not seem correct, in practice, when the frequency of the oscillations is relatively low, quasi-static field conditions prevail and the field can be considered either electric or magnetic depending on the transmitting device. On the other side, the coupling device of the receiver (briefly, the receiving device) is intersected by the alternating field generated by the transmitting device and, acting as a pick-up, takes the energy transported by the field.

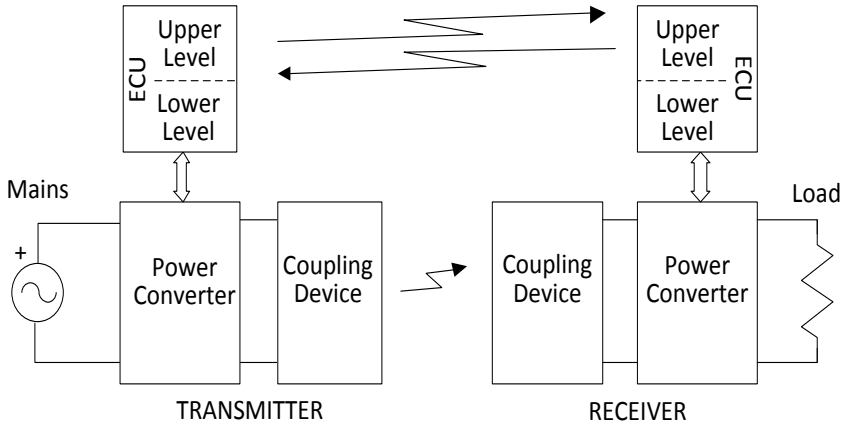

Fig 3.1 WPTS structure

The power converter of the transmitter (shortly, the transmitter converter) comprises of front-end PFC rectifier cascaded by an inverter that feds the transmitting device with an alternating voltage. The power converter of the receiver (shortly, the receiver converter) draws the energy from the receiving device, working as a rectifier that recharges the batteries with the required values of voltage and current.

Each power section of a WPTS includes one electronic control unit (ECU). The two ECUs govern the WPTS operation. The governing tasks are divided into two layers: the upper level provides to the management of the power section whilst the lower level controls the power converter. The upper levels of the two ECUs exchange the information needed for the management of the power sections through wireless communication ports.

3.1 WPTS technologies

Three technologies differing in the type of the involved field are used to transfer electric energy. These three technologies are termed as capacitive, inductive and radiant; they exploit the coupling property of the electric, the magnetic, and the electric and magnetic fields combined together into an electromagnetic wave respectively.

A common feature of the WPTSs is that the transmitting device energizes the surrounding space. In capacitive and inductive power transfers, the respective energy stored in a unitary volume of space is

$$W_e = \frac{1}{2}\varepsilon_0 E^2$$
$$W_m = \frac{1}{2}\mu_0 H^2 \qquad (3.1)$$

where E and H are the intensity of the electric and magnetic fields and, ε_0 and μ_0 are the permittivity and the permeability of the free space. On account of the values of ε_0 and μ_0, and the acceptable voltages across and current into the coupling devices, the energy density achievable with the magnetic field in the free space is about 10^4 times greater than with the electric field. In the radiant power transfer, the energy is concentrated along the transmission path where the electromagnetic field reaches very high values.

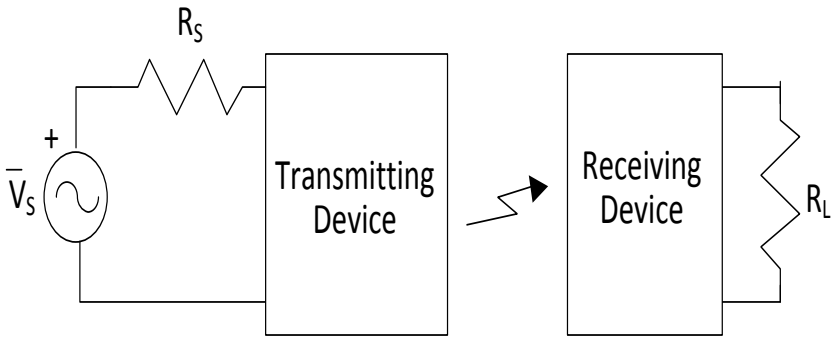

Fig 3.2 WPTS equivalent electric circuitry

3.1.1 Capacitive WPTSs

The coupling devices of the capacitive WPTSs are two plane capacitors with the plates on the transmitter side facing the plates on the receiver side as indicated in Fig.3.3 (a) [1]. The main advantages of the capacitive WPTSs are low losses, insignificant electromagnetic emissions, and ability to transfer power through metal shields without originating eddy currents [2]. On the other hand, the energy density that can be stored in the free space between the plates is comparatively low and consequently the use of the capacitive WPTSs is limited to very low power applications.

3.1.2 Inductive WPTSs

The coupling devices of the inductive WPTSs are two coils mutually coupled as shown in Fig.3.3 (b). The transmitting coil is excited by an alternating current at high frequency, generally between 10 kHz and 150 kHz. Because of the greater energy density of the magnetic field in the free space, inductive WPTSs are able to handle much higher power than the capacitive

ones and can operate at higher power levels. In contrast to these advantages, they suffer from losses in the coils resistances, do not operate if a metallic body is interposed between the coils, and produce appreciable electromagnetic interferences. The inductive WPTSs utilize two topologies for transferring power and the relevant systems are termed as inductive coupling and resonant coupling WPTS.

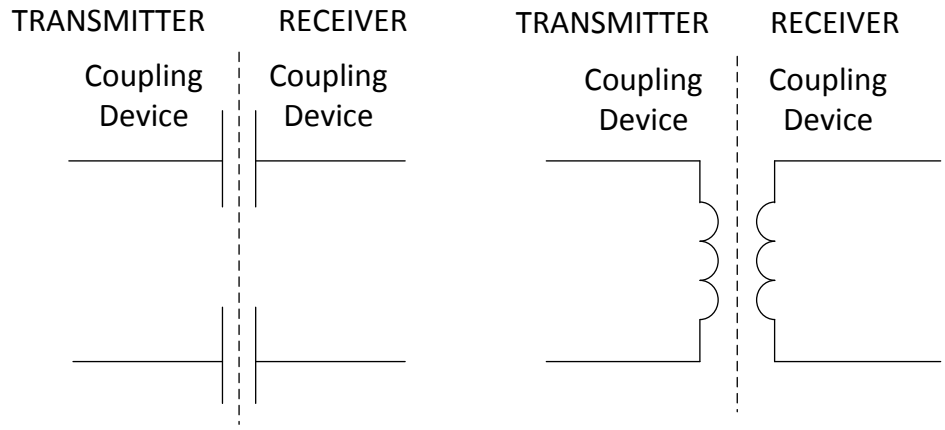

Fig 3.3 Coupling devices for (a) capacitive WPTS and (b) inductive WPTS

3.1.3 Radiant WPTSs

Radiant WPTSs are able to transfer power with high efficiency over a distance several times longer than the size of the coupling devices. This is obtained by executing a directional transmission of the electromagnetic waves [3]. In the radiant WPTSs, the size of the coupling devices is proportional to the wavelength of the electromagnetic waves and hence, in order to maintain it within practical limits, high-frequency waves are used such as microwaves and lasers [4].

Power transmission via radio waves can be made more directional, allowing longer distance power beaming, with shorter wavelengths of electromagnetic radiation, typically in the microwave range. A rectenna is used to convert the microwave energy back into electricity. The microwave source consists of a microwave oven magnetron with electronics to control the output power. The output microwave power ranges from 50 W to 300 W at about 3GHz. A coaxial cable connects the output of the microwave source to a coax-to-waveguide adapter. This adapter is connected to a waveguide ferrite circulator which protects the microwave source from reflected power. The circulator is connected to a tuning waveguide section to match the waveguide impedance to the antenna input impedance.

In the case of radiant WPTS closer to visible region of spectrum (10s of microns (um) to 10s of nm), power can be transmitted by converting electricity into a laser beam that is then pointed at a solar cell receiver. This mechanism is generally known as "power beaming" because the power is beamed at a receiver that can convert it to usable electrical energy. There are quite a few unique advantages of laser based power transfer that outweigh the disadvantages.

(a) Collimated monochromatic wave front propagation allows narrow beam cross-section area for energy confinement over large ranges.
(b) Compact size of solid state lasers-photovoltaic semiconductor diodes allows ease of integration into products with small form factors.
(c) Ability to operate with zero radio-frequency interference to existing communication devices i.e. Wi-Fi and cell phones.
(d) Control of Wireless Power Access, instead of omnidirectional transfer where there can be no authentication before transferring power.
(e) These allow laser-based wireless power transfer concept to compete with conventional power transfer methods.

and Its drawbacks are:

(a) Conversion to light, such as with a laser, is moderately inefficient
(b) Conversion back into electricity is moderately inefficient, with photovoltaic cells achieving 40%-50% efficiency.
(c) Atmospheric absorption causes losses.
(d) As with microwave beaming, this method requires a direct line of sight with the target.

3.2 Figures of Merit

Key figures of merit (FOM) of a WPTS are defined in (3.2): they are the efficiency η, the power supply sizing factor α, the receiving coil sizing factor β and the p.u. magnitude of the load current $I_{L,pu}$, expressed as a fraction of the base current $V_S/\omega M$ [5]. The variables in (3.2) are P_L, which is the active power absorbed by the load, P_S and A_S, which the active and apparent powers are delivered by the power supply, and A_R, which is the apparent power of the receiving coil.

$$\eta = \frac{P_L}{P_S};\ \alpha = \frac{A_S}{P_L}\ ;\ \beta = \frac{A_R}{P_L};I_{L,pu} = \frac{I_L}{V_S/\omega M} \qquad (3.2)$$

Significance of the FOMs are as follows: the efficiency is an index of the power lost in the power transfer process whilst the power source supply factor is an index of the sizing power of the voltage source for a given power absorbed by the power source and similarly reciving coil sizing factor is sizing of the receiver coil across load. p.u. magnitude of load current is expression of load current in terms of p.u values.

3.3 Inductive WPTS

Inductive WPTS uses magnetic fields that are a natural part of current movement through wire. When electrical current moves through a wire, it creates a circular magnetic field around the wire. In this system, alternating voltage applied to one part of coil induces a different terminal voltage of the counterpart at the same frequency.

3.3.1. Theory of operation

Inductive coupling is based on Faraday's law of electromagnetic induction. The electric circuitry of an inductive coupling WPTS is shown in Fig.3.4, where L_T and L_R are the self-

inductances of the transmitting and the receiving coils, M is their mutual inductance, and R_S and R_L are the coil resistances.

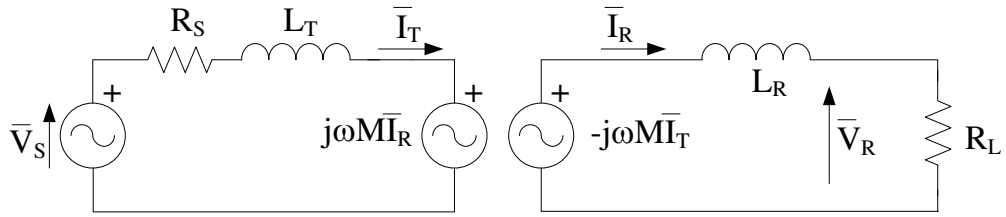

Fig. 3.4. Circuital scheme of inductive WPTSs.

Voltage equations of the transmitter and receiver sections are

$$\begin{cases} \bar{V}_S = \dot{Z}_T \bar{I}_T + j\omega M \bar{I}_R \\ -j\omega M \bar{I}_T = \dot{Z}_R \bar{I}_R \end{cases} \quad (3.3)$$

where $\dot{Z_T}$ and $\dot{Z_R}$ are the impedances of the transmitter and receiver sections, given by

$$\begin{aligned} \dot{Z}_T &= R_S + j\omega L_T \\ \dot{Z}_R &= R_L + j\omega L_R \end{aligned} \quad (3.4)$$

and ω is the angular frequency of $\bar{V_S}$, from (3.4), the currents flowing in the transmitter and receiver sections are derived as

$$\begin{cases} \bar{I}_T = \frac{\bar{V}_S \dot{Z}_R}{\dot{Z}_T \dot{Z}_R + \omega^2 M^2} \\ \bar{I}_R = -\frac{\bar{V}_S j\omega M}{\dot{Z}_T \dot{Z}_R + \omega^2 M^2} \end{cases} \quad (3.5)$$

By (3.4)-(3.6), the complex power $\bar{S_S}$ delivered by the voltage source and the quantities A_S and P_L can be calculated as

$$\bar{S}_S = \bar{V}_S \bar{I}_T^* = \frac{|\bar{V}_S|^2}{|\dot{Z}_T \dot{Z}_R + \omega^2 M^2|^2} \dot{Z}_R^* \left(\dot{Z}_T \dot{Z}_R + \omega^2 M^2\right) \quad (3.6)$$

$$A_S = \frac{|\bar{V}_S|^2 |\dot{Z}_R|}{|\dot{Z}_T \dot{Z}_R + \omega^2 M^2|} \quad (3.7)$$

$$P_L = R_L \|\bar{I}_R\|^2 = \frac{R_L V_S^2 \omega^2 M^2}{\|\dot{Z}_T \dot{Z}_R + \omega^2 M^2\|^2} \quad (3.8)$$

3.3.2. Advantages & disadvantages of inductive WPTS

Advantages:

(a) Simple method of power transfer

(b) Higher efficiency for small distances

Disadvantages:

(a) Efficient operation only for very small distances

(b) Low value of mutual inductance and coupling

(c) Increased resistive heating

(d) It also requires drive electronics and coils that increase manufacturing complexity and cost.

3.3.3. FOMs of inductive WPTS

It is evident the convenience of having WPTSs characterized by i) high efficiency, to reduce the power losses, ii) low PSSF, to reduce the volt-ampere sizing of the power supply, iii) low RCSF, to reduce the volt-ampere sizing of the receiving coil, and iv) high PUMLRC, to reduce the voltage requirements for the power supply with an equal value of ωM.

To simplify the calculation of the FOMs, the resistances of the coils are neglected. Thus, the efficiency can be written as

$$\eta = \frac{R_{TR}}{R_S + R_{TR}} \tag{3.9}$$

where R_{TR} is the resistance of the receiving section referred to the transmitting section. It is given by

$$R_{TR} = \omega^2 M^2 \Re e\left[\frac{1}{\dot{Z}_R}\right] \tag{3.10}$$

Observing that

$$\Re e\left[\frac{1}{\dot{Z}_R}\right] = \frac{\Re e[\dot{Z}_R]}{|\dot{Z}_R|^2} \tag{3.11}$$

the efficiency can be calculated as

$$\eta = \frac{\omega^2 M^2 \Re e[\dot{Z}_R]}{|\dot{Z}_R|^2 R_T + \omega^2 M^2 \Re e[\dot{Z}_R]} \tag{3.12}$$

By similar manipulations of the equations of the circuital scheme in Fig.3.4, the figures of merit PSSF and RCSF are calculated as

$$\alpha = \frac{|\dot{Z}_R||\dot{Z}_T \dot{Z}_R + \omega^2 M^2|}{\omega^2 M^2 \Re e[\dot{Z}_R]} \tag{3.13}$$

$$\beta = \frac{|\dot{Z}_R - j\omega L_R|}{\Re e[\dot{Z}_R]} \tag{3.14}$$

$$I_{L,pu} = \frac{\omega^2 M^2}{|\dot{Z}_T \dot{Z}_R + \omega^2 M^2|} \tag{3.15}$$

The FOMs are conveniently written in terms of the adimensional quantities in (3.16)-(3.18), where Q_T and Q_R are termed as the quality factors respectively of the transmitting section and of receiving section, and k is the coupling coefficient of the coils.

$$Q_T = \frac{\omega L_T}{R_S} \tag{3.16}$$

$$Q_R = \frac{\omega L_R}{R_L} \tag{3.17}$$

$$k = \frac{M}{\sqrt{L_T L_R}} \tag{3.18}$$

By substituting (3.4) into (3.12)-(3.15) and using (3.16) -(3.18), the FOMs of the inductive WPTSs result in

$$\eta_I = \frac{k^2 Q_R Q_T}{1+Q_R^2+k^2 Q_R Q_T} \tag{3.19}$$

$$\alpha_I = \frac{\sqrt{(1+Q_R^2)[(1+(k^2-1)Q_R Q_T)^2+(Q_R+Q_T)^2]}}{k^2 Q_R Q_T} \tag{3.20}$$

$$\beta_I = 1 \tag{3.21}$$

$$I_{L,pu,I} = \frac{k^2 Q_R Q_T}{\sqrt{[1+(k^2-1)Q_R Q_T]^2+(Q_R+Q_T)^2}} \tag{3.22}$$

As shown by (3.19) efficiency inductive coupling WPTSs can be enhanced by increasing the coupling coefficient and the quality factors of the coils, especially the transmitting coil. Regarding the coupling coefficient, an inductive coupling WPTS behaves like a transformer but, differently from a conventional arrangement, here the coils do not share a common core; hence *k* is far from 1 and usually does not exceed 0.6, depending on the coil shape and size. Furthermore, it decreases approximately with the cube of the distance of the coils. Regarding the quality factors, (3.16) and (3.17) suggests that they can be increased by working at high angular frequencies. This is true up to certain frequencies, roughly around 1 MHz, above which parasitic effects such as the skin effect arises in the coils, producing an increment in their effective resistances and making not convenient a further increase in the working frequency.

Low coupling coefficient and quality factors calls for high values of active and apparent powers required for the voltage source in relation to the power absorbed by the load. Therefore, the inductive coupling WPTSs are effective in transferring power when the distance between the coils is shorter than their size (short-range applications).

3.4 Resonant WPTS

Resonant coupling WPTSs, add capacitors to the coupling coils with the aim of reducing the amount of voltage and/or current required to feed the WPTS. At resonance condition, collapsing magnetic field of the inductor generates an electric current in its windings that charges the capacitor, and then the discharging capacitor provides an electric current that builds the magnetic field in the inductor. In resonance mode power is transferred between inductor and capacitor and they are equal.

3.4.1. Theory of operation

Resonant coupling operates on the principles of the works on the principle of resonance between the coils. Resonant coupling also called the resonant inductive coupling which was proposed by MIT [6]. A number of topologies are possible, with the capacitor inserted in se-

ries and/or in parallel to the transmitting and/or receiving coil. Each topology has a different impact on the WPTS performance [7], [8].

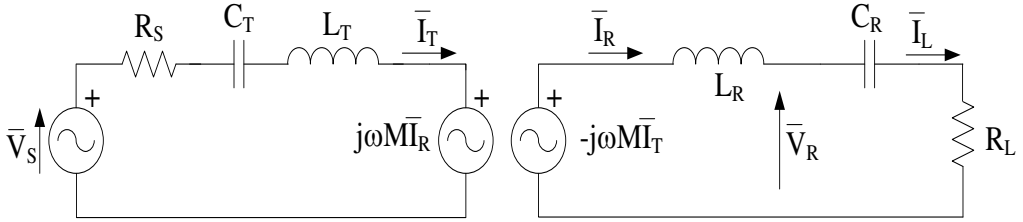

Fig. 3.5. Circuital scheme of inductive WPTSs.

3.4.2. Advantages & disadvantages of resonant WPTS

Advantages:

1. Compared to the Inductive WPTS, resonant WPTS are more efficient in terms of quality factor and power factor
2. Can transfer power to more distance compared to inductive WPTS

Disadvantage:

1. Can't transfer power more than 1 or 2 meters

3.4.3. FOMs of resonant WPTS

The efficiency of a resonant coupling WPTS obtained by inserting a capacitor in series to the coils. As an example, Fig.3.5 shows the circuitry of a resonant coupling WPTS when the capacitor C_R is inserted in series to the receiving coil. In this case, the capacitor modifies the receiver section impedance in

$$\dot{Z_R} = R_L + j\left(\omega L_R - \frac{1}{\omega C_R}\right) \qquad (3.23)$$

If the capacitor C_T is inserted in series to the transmitting coil, it modifies the transmitter section impedance as

$$\dot{Z_T} = R_S + j\left(\omega L_T - \frac{1}{\omega C_T}\right) \qquad (3.24)$$

Resonant WPTSs are operated in order that the LC branches both at the primary and at the secondary resonate at the supply frequency of the voltage generator. Then it is

$$\begin{aligned} \omega^2 C_T &= \frac{1}{L_T} \\ \omega^2 C_R &= \frac{1}{L_R} \end{aligned} \qquad (3.25)$$

At this frequency, the receiver section impedance is minimum and equal to

$$\dot{Z}_T = R_S \qquad \dot{Z}_R = R_L \tag{3.26}$$

And the efficiency of a resonant coupling WPTS, obtained by substituting (3.26) into (3.12), becomes

$$\eta_R = \frac{\omega^2 M^2}{\omega^2 M^2 + R_L R_S} \tag{3.27}$$

where the subscript *R* stands for resonant on the receiver section. By (3.16)-(3.18), so (3.22) can be rewritten as

$$\eta_R = \left(\frac{k^2 Q_T Q_R}{1 + k^2 Q_T Q_R}\right) \tag{3.28}$$

The efficiency has an expression similar to (3.19) but, because of the missing term Q_R^2 at the denominator, it takes higher values than in an inductive WPT

And calculating the remaining FOMs for resonant case as follows

$$\alpha_R = \frac{1 + k^2 Q_R Q_T}{k^2 Q_R Q_T} = \frac{1}{\eta_{SS}} \tag{3.29}$$

$$\beta_R = \sqrt{1 + Q_R^2} \tag{3.30}$$

$$I_{L,pu,R} = \frac{k^2 Q_R Q_T}{1 + k^2 Q_R Q_T} = \eta_{SS} \tag{3.31}$$

From the equations (3.29)-(3.31) it emerges that (1) PSSF is inverse of efficiency (2) RCSF is depends only on quality factor of receiver (3) PULC is same as the efficiency.

3.5 Conclusion

The chapter has presented a preliminary study on the WPTSs for the recharge of the electric vehicle batteries considering three different technologies. Four FOMs are introduced and their enhancement in characteristics of the resonant WPTSs over the inductive ones has been demonstrated.

3.6 References

[1] L.Chao, A.P.Hu and M.Budhia, "A generalized coupling model for capacitive power transfer systems," Proc. of IEEE Industrial Electronics Conference, 2010, pp. 274-279.

[2] C.Y.Xia, C.W.Li and J.Zhang, "Analysis of power transfer characteristic of capacitive power transfer system and inductively coupled power transfer system," Proc. of Int. Conference on Mechatronic Science, Electric Engineering and Computer, 2011, pp. 1281-1285.

[3] R.J.Parise, "Model to predict performance of all electric transportation with wireless power beams," Proc. of Energy Conversion Engineering Conference, 2002, pp.731-736.

[4] W.C.Brown, "The history of power transmission by radio waves," *IEEE Trans. on microwave theory and techniques*, vol. MTT-32, n. 9, pp. 1230-1242, 1984.

[5] K.N.Mude, M.Bertoluzzo and G.Buja, “Design of contactless battery charger for electrical vehicle,” Proc. of IEEE International Conference of AFRICON 2013, 2013, pp.1091-1096.

[6] A.Kurs, A.Karalis, R.Moffatt, J.D.Joannopoulos, P.Fisher and M. Soljacic, “Wireless power transfer via strongly coupled magnetic resonances,” Sci. Exp., vol. 317, no. 5834, pp. 83–86, June 2007.

[7] O.H.Stielau and G.A.Covic, ”Design of loosely coupled inductive power transfer systems,” Proc. of International Conference on Power System Technology, 2000, vol. 1, pp. 85-90.

[8] R.R.Harrison, “Designing Efficient Inductive Power Links for Implantable Devices,” Proc. of IEEE Int. Symposium on Circuits and Systems, 2007, pp. 2080-2083.

Chapter 4
Coil Design of Wireless Power Transfer Systems (WPTS)

Summary

Wireless power transfer system consists of coupling device, made of two coils whose setup is a crucial issue in building up a WPTS. This chapter deals with the design procedure of the coils of a WPTS intended to charge the battery pack of electric city car. Two coupling structures analysed namely helix and spiral. The analysis, carried out by help of a FEM code, encompasses the determination of the inductive parameters as a function of the coil distance, turn number, turn distance (for spiral coil only) and axial misalignment

4.1 Basics of electro magnetics

The basics of electromagnetic are derived from the Maxwell equations, both in time independent and time dependent cases. The four Maxwell equations are as follows

$$\oint \vec{E} . \overrightarrow{dl} = -\frac{\overrightarrow{\partial B}}{\partial t} \quad (4.1)$$

$$\oint \vec{H} . \overrightarrow{dl} = \vec{J} + \left(-\frac{\overrightarrow{\partial D}}{\partial t}\right) \quad (4.2)$$

$$\oint \vec{D} . \overrightarrow{ds} = \rho_v \quad (4.3)$$

$$\oint \vec{B} . \overrightarrow{ds} = 0 \quad (4.4)$$

The quantities $\vec{E}, \overrightarrow{H}, \vec{D}$ and $\vec{B}$ are the electric field, magnetic intensity, electric displacement and magnetic flux density respectively.

There are four laws associated with the Maxwell: they Faraday's law of electro magnetism, Ampere's law, the third and fourth are Gauss laws for the electric and magnetic fields. They are explained as follows [1]

i. *Faraday's Law of electromagnetism*
   The line integral of the electric field around a closed loop is equal to the negative of the rate of change of the magnetic flux density through the area enclosed by the loop.
ii. *Ampere's Law*
   This law states that current is a source of the magnetic field, thus the magnetic field is related to the current density.
iii. *Gauss law for electric field*
   This law states that the amount of total electric flux displacement through a given closed surface is proportional to the amount of volume charge ρ_v in the volume contained by that surface.
iv. *Gauss law for magnetic field*

This states that all magnetic field lines which enter a particular closed surface must eventually leave the surface, thus there are no magnetic monopoles or sources of magnetic charge.

4.2 Coil parameters

4.2.1. Coil resistance

It is important to calculate the resistance of the primary and secondary coils in WPTS, as they represent the main limitation for the power that can be transferred. Actually, if resistances were zero, the efficiency of the transformer would be 100 %. Coil resistances generate joule effect and this heat has to be remain at an acceptable level. Minimizing the Joule losses is then a crucial point while designing WPTS, in terms of efficiency and transferable power.

$$R = \frac{\rho l}{A_{wire}} \qquad (4.5)$$

where l is length of the coil, A_{wire} is area of the wire, ρ is resistivity of the coil

4.2.2. Coil Inductance and magnetic flux density

An inductor is a passive two-terminal electrical component that stores energy in its magnetic field. Inductance (L) results from the magnetic field forming around a current-carrying conductor and linked with it. Electric current through the conductor creates a magnetic flux proportional to the current. A change in this current creates a corresponding change in magnetic flux which, in turn, by law generates an electromotive force (EMF) in the conductor that opposes this change in current. Thus inductors oppose changes in current through them. Inductance is a measure of the amount of electromotive force generated per unit change in current.

The magnetic flux density is a field that is created by a current in a conductor. It is related to the magnetic field H through the magnetic permeability that characterizes the medium in which the conductor is situated.

One of the key factors that define the performance of a WPTS is the coupling coefficient of the coils. It depends on the size and the shape of the coils and on the distance between them. In some cases, it can be analytically calculated starting from the Biot-Savart law

$$d\vec{B} = \frac{\mu_0}{4\pi} I \frac{d\vec{l}\times\vec{r}}{r^3} \qquad (4.6)$$

that gives, for any point P in the free space, the magnetic induction contribution $d\vec{B}$ generated by the current I flowing in the infinitesimal portion $d\vec{l}$ of an electric circuit at distance r from P. The magnetic induction is calculated by integrating along the full circuit. For example, in a point belonging to the axis of a circular coil formed by n turns and lying at

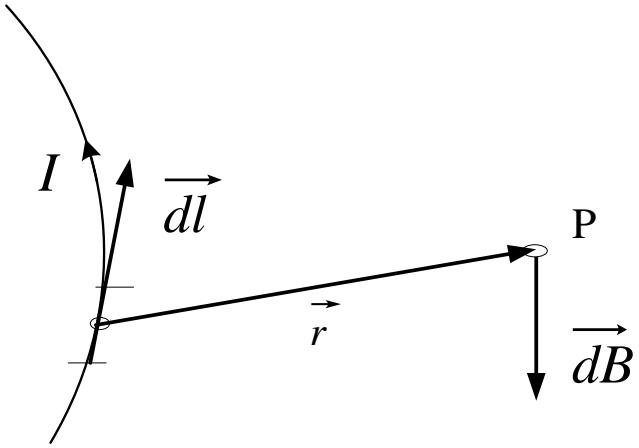

Fig 4.1. Biot-Savart Law

a distance d from the center of the coil, the magnetic induction has the same direction of the axis and magnitude equal to

$$B = \frac{\mu_0}{4\pi} nI \frac{2\pi R^2}{(R^2+d^2)^{\frac{3}{2}}} = \frac{\mu_0}{2\pi} nI \frac{A}{(R^2+d^2)^{\frac{3}{2}}} \approx \frac{\mu_0}{2\pi} nI \frac{A}{d^3} \quad (4.7)$$

where R is the radius of the coil, A is its cross-section and d is the distance between coils. The last expression of B in (4.7) holds when the distance from the coil is much longer than the coil radius. If the magnitude of the magnetic induction is constant across the coil cross-section, the self-inductance of the coil is given by [2].

$$L = \mu_0 N^2 R \left[ln\left(\frac{8R}{r}\right) - 2 \right] \quad (4.8)$$

where r is radius of wire

4.2.3. Mutual inductance

It is the phenomenon in which a change of current in one coil causes an induced emf in another coil placed near to the first coil. This parameter is most dependable for design of WPT system.

4.2.4. Skin effect and proximity effect

If the conductor is composed of one or more concentric circular elements, then the center portion of the conductor will be enveloped by a greater magnetic flux than those on the outside. Consequently the self-induced back emf will be greater towards the center of the conductor, thus causing the current density to be less at the center than at the conductor surface. This extra concentration at the surface is known as skin effect, and results in an increase in the effective resistance of the conductor.

The skin depth, δ, is defined as the depth at which the current density falls to 1/e, (about 0.37), of the current density at the surface. This is given by

$$\delta = \sqrt{\frac{2\rho}{\omega\mu}} \qquad (4.9)$$

where ρ is the resistivity of the material and is related to the conductivity as 1/σ, μ is the permeability of the material and ω is angular frequency of the electrical solicitation.

The proximity effect also increases the effective resistance and is associated with the magnetic fields of two conductors which are close together. If each carries a current in the same direction, the halves of the conductors in close proximity are cut by more magnetic flux than the remote halves. Consequently the current distribution is not even throughout the cross-section, a greater proportion being carried by the remote halves. If the currents are in opposite directions, the halves in close proximity will carry the greater density of current.

4.3 Coil design

Coil-coupling structures are analysed with the view of building up a WPT system with resonant topology for charging the battery pack of the electric city-car of the study case. Its data, given in Appendix B, to determine the WPT specifications listed in Table 4.1.

Nominal supply voltage follows from the request of charging the electric city-car from a single-phase domestic socket at 230 V. Maximum output power follows from the charging current (10 A) and maximum voltage (56 V) of the battery pack. Receiver coil radius and coil distance follow from the city-car dimensions. Instead, the specification regarding the operating frequency follows from the recent resolution of the SAE International J2954 Task Force for WPT to fix at 85 kHz the nominal frequency of operation of the WPT systems for light-duty plug-in vehicles.

The transmitting coil of the WPTS is supplied by a high frequency (HF) inverter that, in turn, is fed by a rectifier connected to the grid. The receiving coil supplies a diode rectifier cascaded by a DC-DC converter that adjusts the rectified voltage to the battery requirements. In order to maintain a high overall efficiency, the amplitude of the output voltage of the HF inverter should not be much lower than the rectified grid voltage and, on the other side of the WPTS, the rectified voltage at the input of the DC-DC converter should not be much higher than the battery voltage.

Table 4.1. WPT specifications

Parameter	Symbol	Value
Nominal supply voltage	V_N	230 V_{rms}
Nominal output power	P_N	560 W
WPT system operating frequency	f	85 kHz
Coil radius	R	0.19 m
Distance between coils	d	0.15 m

From this quantity, from the battery charging characteristics and considering an efficiency of 95% for the DC-DC converter, the equivalent resistance R_O seen at the output of the rectifier has been computed. From it, the equivalent resistance at the input of the HF rectifier, i.e. R_L, has been obtained according to

$$R_L = \frac{8}{\pi^2} R_O \qquad (4.10)$$

Given the equivalent R_L and the working frequency, the specification for Q_R can be easily translated into specification for L_R by means of (3.17). From the given values of Q_T and Q_R, normalized load current($I_{R,L}$) can be calculated by (4.1.1) terms in brackets, as in this stage we don't have the value of M

$$\bar{I}_{R,L} = \frac{\bar{V}_S}{j\omega_r M}\left(\frac{k^2 Q_T Q_R}{1+k^2 Q_T Q_R}\right) = \frac{\bar{V}_S}{j\omega_r M}\eta_r \qquad (4.11)$$

According to the above requirements and making allowance for the variations in the grid voltage and the voltage drops across the circuitry, the minimum and maximum values of V_s should be less than or equal to 280 V. so the consideration of preliminary values of V_{DC} is 65 V and minimum and maximum values of resistance of battery is 5.8 Ω to 580 Ω. with this preliminary values, the peak values of rectified current can be evaluated from (4.12)

$$I_{R,pk} = \frac{4}{\pi}\frac{V_{DC}}{R_L} \qquad (4.12)$$

the value comes to be 0.142 A≤ $I_{R,pk}$≤14.2 A.

In the resonance condition , by neglecting equivalent series resistance (ESR) , $V_{s,pk}$ can be

$$V_{s,pk} \le \omega M I_{R,pk} = \frac{4}{\pi}\frac{V_{DC}}{R_L}\omega M \qquad (4.13)$$

considering the nominal resonant frequency, V_{DC}, $V_{s,pk}$ and minimum value of R_L the value of mutual inductance can be calculated from (4.13) for the minimum distance of 0.1m should not exceed 35 μH. With this constraint the transmitter peak current can be calculated as

$$I_{T,pk} = \frac{4}{\pi}\frac{V_{DC}}{\omega M} \qquad (4.14)$$

and the value comes out to be 4.42 A.

From the manipulation of electrical equations and the data of mutual inductance, self-inductance of transmitter and secondary comes out to be around 120 μH. In the resonance condition inductive and capacitive voltages are equal and according to (3.25), capacitance (C_T and C_R) becomes 29.71 nF. The numerical values obtained from above designed procedure are reported in Table 4.2.

Table.4.2

Parameter	Symbol	Value
Minimum battery voltage	$V_{B,m}$	36 V
Maximum battery voltage	$V_{B,M}$	56 V
Battery charging current	I_B	10 A
Coils diameter	D	0.38 m
Distance between coils	d	0.15 m
HF inverter frequency	f	85 kHz
Efficiency of coupling	η	>0.95
Minimum HF voltage	$V_{S,m}$	280 V
HF rectifier output voltage	V_{DC}	65V
Minimum equivalent R_L	$R_{L,m}$	5.8 Ω
Maximum load current	$I_{RL,M}$	10 A

4.4 Coil Types

Mainly two types of coil structures are used in WPT. They are helix and spiral coil, and hereafter, assumption is made that the transmitter and receiver coils have equal geometry, dimension and turn number, the latter one being denoted with *N*.

4.4.1. Helix coil

The left half of Fig. 4.2 (a) sketches the arrangement of the helix coil (wire radius is not in scale with the coil dimension). The turns are packed together in a rectangular section, having base *b* and height *h*, and their mean distance from the coil axis is R_m. The self-inductance of each coil can be formulated as [14]

$$L_{Helix} = \frac{0.31\,(R_m N)^2}{6R_m + 9h + 10b} \qquad (4.15)$$

where N is the number of turns. By repeatedly using (4.15) and adjusting its parameters accounting for a plausible wire radius of 2.5 mm, it resulted that a coil with 15 turns, arranged in a 5x3 pattern, satisfy the requirement of having a self-inductance.

4.4.2. Spiral coil

The arrangement of two aligned spiral coils is shown in Fig.4.2 (b). The self-inductance of a spiral coil can be formulated as [3]

$$L_{spi} = C_1 \mu_0 N^2 R_{avg} \left[ln\left(\frac{C_2}{\emptyset}\right) + C_3 \emptyset + C_4 \emptyset^2 \right] \qquad (4.16)$$

where the average coil radius R_{avg} and the fill factor ϕ are expressed as

$$R_{avg} = \frac{(R_o + R_i)}{2};\ \emptyset = \frac{(R_o - R_i)}{(R_o + R_i)} \qquad (4.17)$$

where d, Ri and Ro are the coil distance, and the coil inner and outer radii, respectively and the coefficients C_i with i=1, 2, 3, 4 depend on the circular coil layout; according to [3], the

following values apply to the coefficients with the layout in Fig.4.2 (b): C_1 = 1.00, C_2 = 2.46, C_3 = 0.00, and C_4 = 0.20. By putting the inner coil radius at 0.08 m, the turn number needed to obtain a coil with the requested inductance results in N=18.

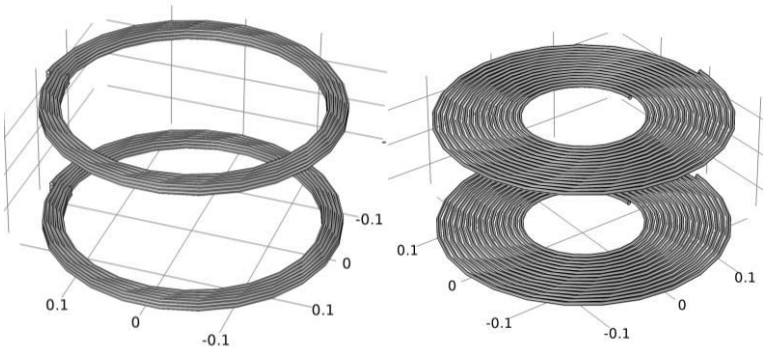

(a) (b)

Fig.4.2. (a) helix and (b) spiral coils.

4.5 Coil coupling arrangement analysis

Further to the preliminary sizing, an accurate analysis of the helix and spiral coil arrangements is here developed to compare their inductive performance for the study case of Appendix B.

Both helix and spiral coils have been considered and, for each of them, the inductive parameters have been calculated with the end of identifying the set of geometric data that give the better achievements in terms of coupling coefficient. Calculations have been executed with the help of COMSOL FEM code

(a) *Helix coil-coupling*

At first, coil misalignment has been set to zero and the FEM analysis [4] has been used to investigate the impact of turn number and coil distance on the self and mutual inductances and on the coupling coefficient. Fig.4.3 shows the magnetic flux density lines of helix coil.

The main outcomes of the analysis are illustrated in Figs. 4.4-4.6. Fig. 4.4 plots the self- and mutual inductances against the turn number for different coil distances, where the turn number ranges around the value found by the preliminary sizing. Figs. 4.5 (a) and (b) plot the coupling coefficient respectively as a function of the turn number for coil distance of 0.15 m and as a function of the coil distance for N=15. Fig. 4.6 (a) gives the magnetic flux density on the surface of a helix coil with N=15 and current of 1 A.

Inspection of the figures show that: i) both the self- and mutual inductances increase about proportionally to the square of the turn number so that the coupling coefficient results marginally influenced by N, ii) the self-inductance does not vary with the two-coil distance because the structure has no magnetic core, iii) the coupling coefficient, like the mutual inductance, decreases as the coil distance increase, iv) the magnetic flux density is high only

on a small portion of the coil surface since the turns are packed together and span only a negligible part of the coil radius

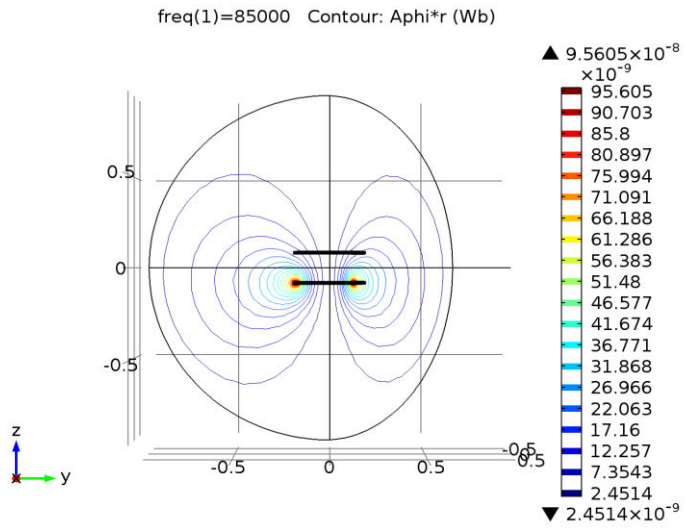

Fig.4.3. Magnetic flux lines of helix coil

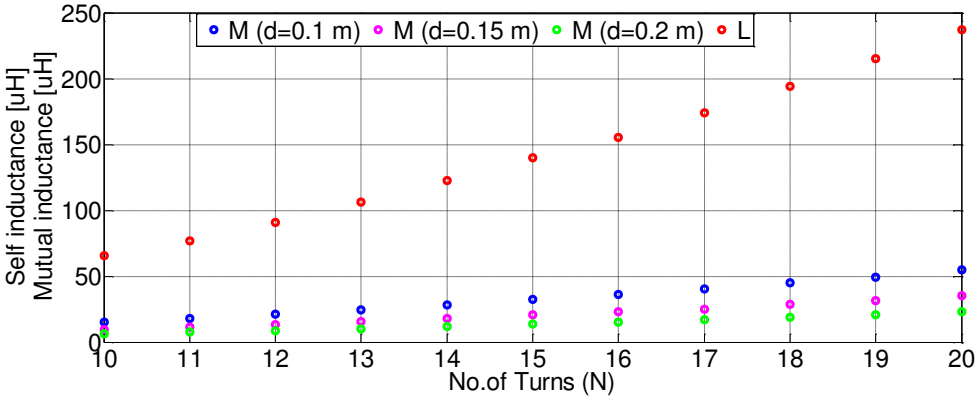

Fig. 4.4. Helix coil-coupling self- and mutual inductance vs. turn number for different coil distances in m.

The impact of the coil misalignment on the coupling coefficient is analysed for the coils laying on two planes 0.15 m far each other. The outcome of the analysis, plotted in Fig. 4.7, shows that the coil misalignment has a lower influence in the coupling coefficient than the coil distance. For example, increasing the coil distance of 0.1 m (from 0.1 to 0.2 m), causes a decrease of k of about 94% as a percentage of its value at 0.15 m while a coil misalignment of 0.1 m (from 0 to 0.1 m), causes a decrease of k of about 22%.

(b) Spiral coil coupling

The spiral coil-coupling is analysed in the same way as the helical one. The main outcomes of the analysis, calculated for the turn distance t_d set at the reasonable value of 7 mm, are illustrated in Figs. 4.8 and 4.5 (b). Fig. 4.8 plots the self- and mutual inductances against the turn number for different coil distances. Figs. 4.5 (a) and (b) plot the coupling coefficient respectively as a function of the turn number for coil distance of 0.15 m and as a

function of the coil distance for N=15. Fig. 4.6 (b) gives the magnetic flux density on the surface of the spiral coil with the current of 1 A.

The outcomes can be discussed starting from the inspection of Fig. 4.6 (b). Indeed, the magnetic flux density is only 38% compared to the helix coil and the surface of the inner turns is much smaller than the surface of the outer turns so that the flux linked by the inner turns is less. Therefore, the self- and mutual inductances of the spiral-coil coupling are lower than those of the helix counterpart. Nevertheless, the flux density is more uniform across the coil surface and this yields a coupling coefficient that is about 18% greater than the helix counterpart This feature grants a higher efficiency to a WPT system with spiral coil-coupling.

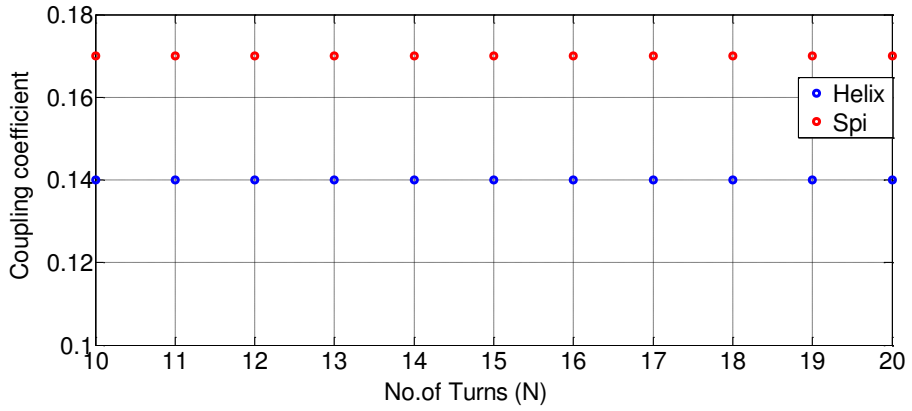

(a)

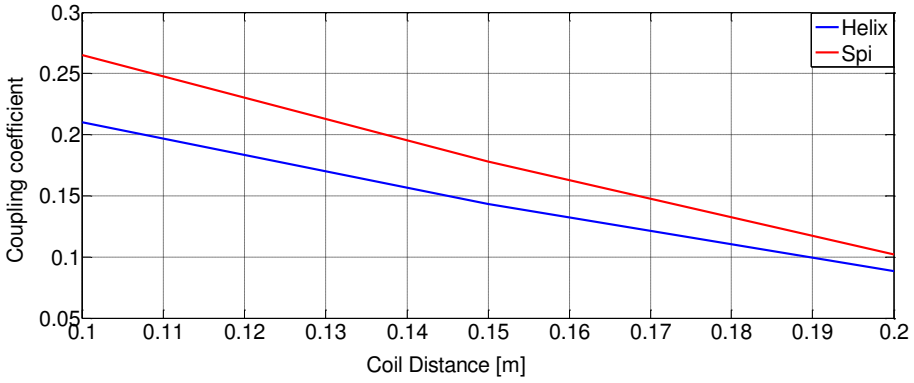

(b)

Fig. 4.5. Coupling coefficient vs. (a) turn number (d=0.15 m), and (b) coil distance (N=15) for helix and spiral coil-couplings (td=7 mm for the spiral coil-coupling).

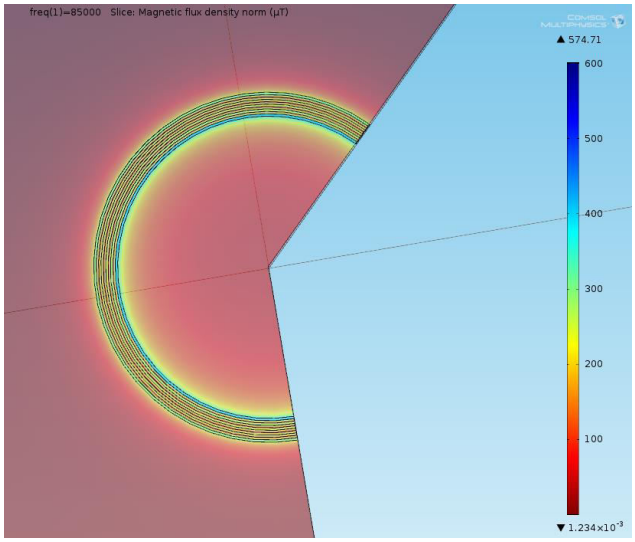

(a)

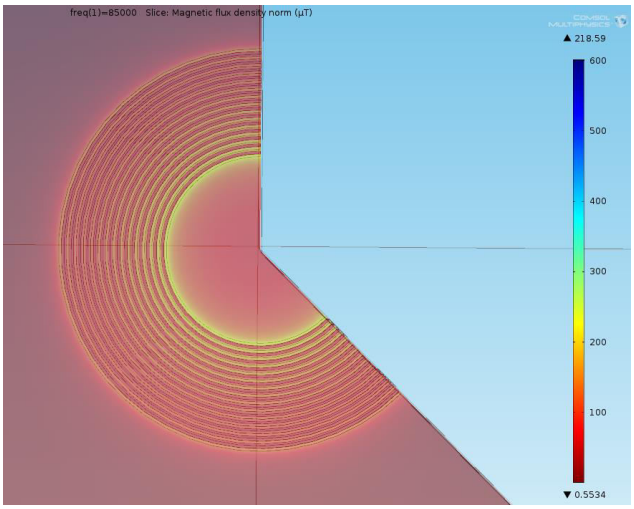

(b)

Fig. 4.6. Magnetic flux density in μT on the surface (a) of a helix coil and (b) of a spiral coil (N=15, 1 A, t_d=7 mm for the spiral coil-coupling).

The impact of the coil misalignment is analysed for the coils lying on planes 0.15 m far. The outcome of the analysis, plotted in Fig. 4.7, shows that the spiral coil-coupling exhibits a larger coupling coefficients than the circular one even in misalignment conditions. Sensitivity of the coupling coefficient of the spiral coil-coupling to the coil distance is not much less than for the circular one while its sensitivity to the coil misalignment becomes greater as the misalignment increases. For example, increasing the coil distance of 0.1 m (from 0.1 to 0.2 m) causes a decrease of *k* of about 85% whilst a coil misalignment of 0.1 m (from 0 to 0.1) causes a decrease of *k* of 30%; instead, a coil misalignment of 0.2 m (from 0 to 0.2) causes *k* to fall down to 70%. This because the distributed arrangement of a spiral coil hampers a coil to link the flux produced by the faced coil under a large misalignment. Besides turn number and coil distance, the inductive parameters of the spiral coil-coupling

depend on the turn distance. The relationship, plotted in Fig. 4.9, shows that a decrease in the turn distance increases the self- and mutual inductances as it can be readily explained by the fact that such a decrease makes the coil arrangement more similar to a circular one. The coupling coefficient, instead, is practically unaffected by the turn distance. Fig.4.10 and Fig.4.11 shows Magnetic flux density lines of spiral coil and in misalignment.

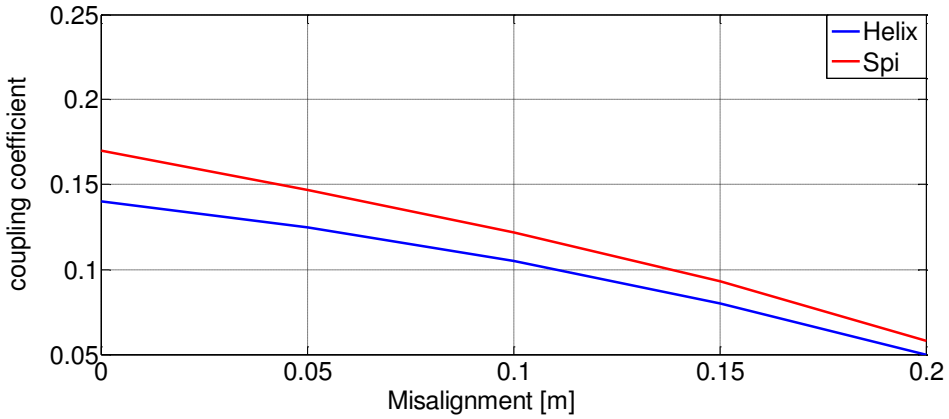

Fig. 4.7. Coupling coefficient vs. misalignment for helix and spiral coil-couplings (N=15, t_d =7 mm for the spiral coil-coupling).

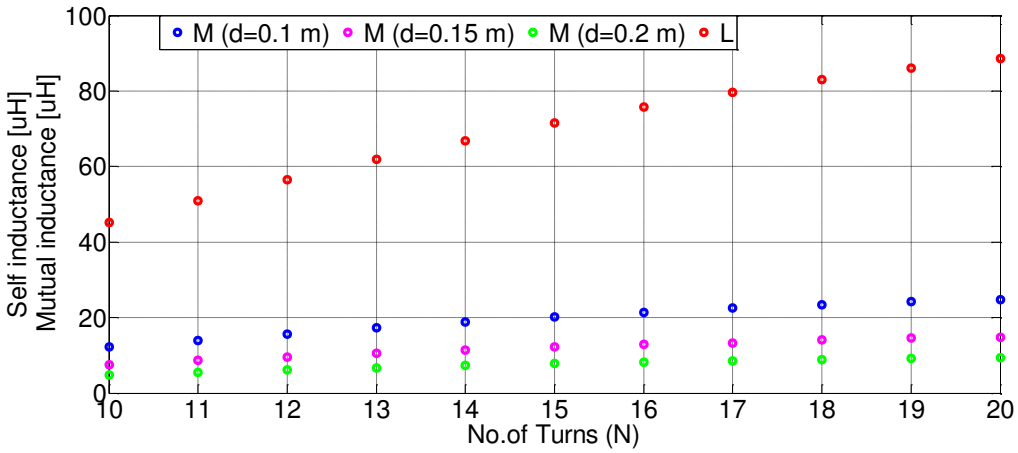

Fig. 4.8. Spiral coil-coupling self- and mutual inductance vs. turn number for different coil distances (t_d =7 mm).

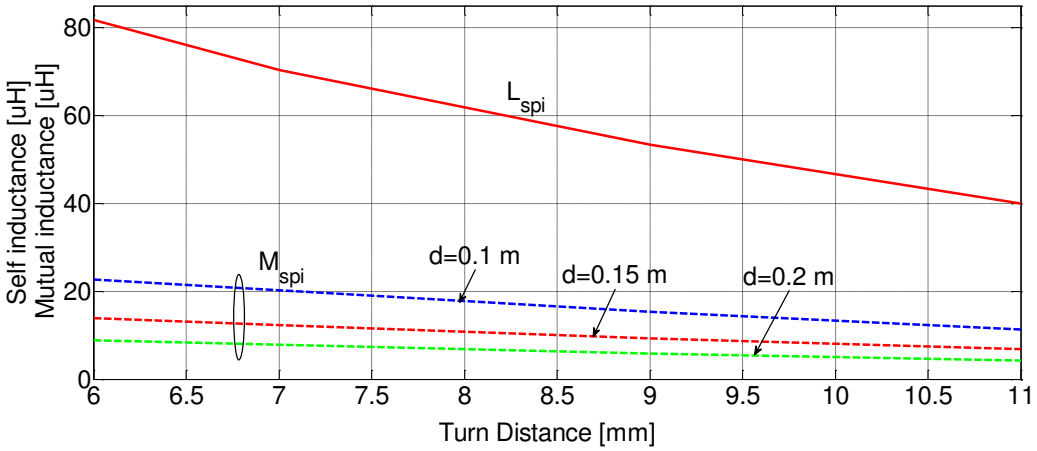

Fig. 4.9. Self- and mutual inductances of the spiral coil-coupling vs. turn distance for different coil distances (N=15).

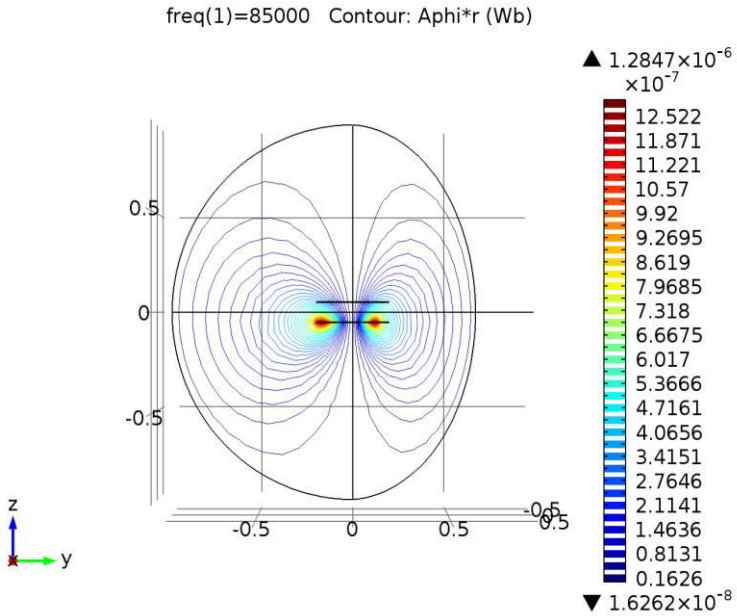

Fig.4.10. Magnetic flux lines of spiral coil

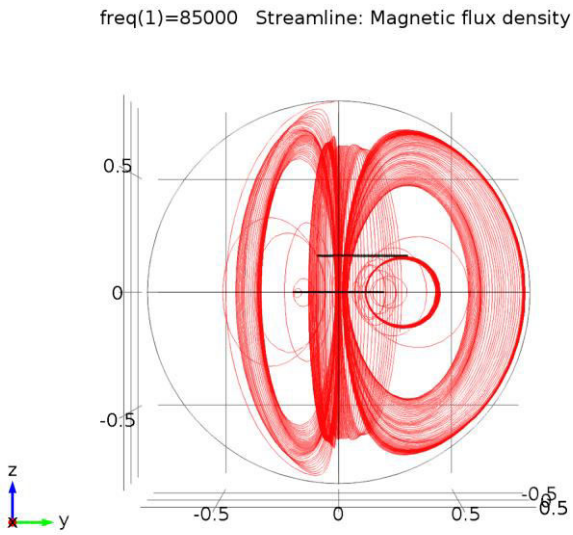

Fig.4.11. Misalignment of coil system.

4.6 Conclusion

This chapter has dealt with the coil-coupling of a WPT system intended to charge an electric city-car. At first design of coil system is presented and by analysis carried out how different coil arrangements affect the performance of the coil-coupling in terms of inductive parameters. It has been found that, for a given outer diameter and distance of the coils, the spiral coil-coupling has an higher coupling coefficient compared to the helix one despite its lower self and mutual inductances.

4.7 References

[1] G.D.Jeffrey and R. College.”Introduction to electrodynamics,”,Vol. 3, NJ: Prentice hall, 1999.

[2] H.W.Grover, “Inductance Calculations: Working Formulas and Tables,” Dover Pub., New York, 1962.

[3] S.Mohan, M.Hershenson, S.P.Boyd, and T.H.Lee, “Simple accurate expressions for planar spiral inductances," IEEE Journal of Solid State Circuits, Vol. 34, pp. 1419-1424, 1999.

[4] Comsol Multiphysics, “Documentation Set”, version 4.3, www. comsol.com.

Chapter 5

Core structures for WPTS

Summary

The presence of a ferrite core for WPTS can add advantages due to the improved conduction of magnetic flux and the lower reluctance of the magnetic circuit. The coupling between the coils increases and less turns of wire are needed to get the same inductance than in coreless. This chapter deals with influence of core structures on design of WPTS system and different parametric studies are carried out for determine best suitable core structure.

5.1. Introduction

Magnetic materials have been so extensively used in a diverse range of applications, that the advancement and optimal utilization of magnetic materials have been significantly improved. Magnetic materials are classified in terms of their magnetic properties and their uses. If a material is easily magnetized and demagnetized then it is referred to as a soft magnetic material, whereas if it is difficult to demagnetize then it is referred to as a hard (or permanent) magnetic material.

Most of pure elements in the periodic table are either diamagnetic or paramagnetic at room temperature. Since they present very small magnetism under the influence of an applied field, they are normally termed as non-magnetic. Another type of magnetism is called antiferromagnetic, and the only pure element presenting this characteristic is Cr in natural environment. Fe, Co, and Ni are called ferromagnetic because very high levels of magnetism can be observed if one apply a field to these materials. Actually, pure single element ferromagnetic materials are seldom seen as magnets or cores. In practical applications, alloys composed of these elements and other ingredients are more widely used. Therefore, all of these alloys are also categorized as ferromagnetic. Although they cannot be observed in any pure element, they can be found in compounds, such as the mixed oxides, known as ferrites. In general ferromagnetic exhibit better loss performance but lower saturation flux density, compared with ferrimagnetic [1].

5.2. Ferrite core structure and their need

Since the most of the times, ferrite materials have been developed for high-frequency applications because of their high electrical resistivity and low eddy current losses. The wide range of possible geometries, the continuing improvements in the material characteristics and their relative cost-effectiveness make ferrite components the choice for both conventional and innovative applications [2], [3]. Ferrites have a paramount advantage over other types of magnetic materials: high electrical resistivity and resultant low eddy current losses over a wide frequency range. Additional characteristics such as high temperature stability have expanded ferrite uses into quality filter circuits, high frequency transformers, wide band transformers, adjustable inductors, delay lines, and other high frequency electronic circuitry. As the high frequency performance of other circuit components continues to be improved, ferrites are routinely designed into magnetic circuits for both low level and power applications. For the most favorable combination of low cost, high Q, high stability, and

lowest volume, ferrites are the best core material choice for frequencies from 10 KHz to 50 MHz. Ferrites offer an unmatched flexibility in magnetic and mechanical parameters.

5.3. Cored coupling

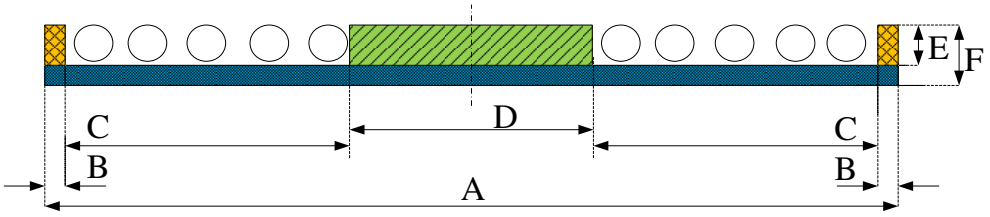

A	B	D	E	F
0.40 m	0.01 m	f(N,t_d)	0.01 m	0.015 m

Fig. 5.1. Sections and dimensions of the cores.

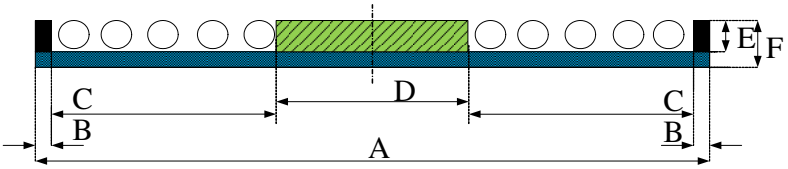

(a)

A	B	D	E	F
0.40 m	0.01 m	f(N,t_d)	0.01 m	0.015 m

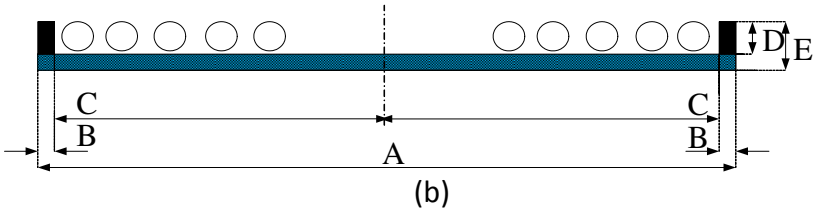

(b)

A	B	D	E
0.40 m	0.01 m	0.01 m	0.015 m

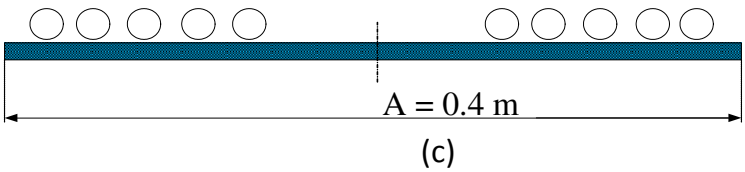

(c)

Fig. 5.2. Sections and dimensions of the three core structures (a) E core (b) C core (c) I core

To improve the coupling coefficient of a WPT system, structures with coils placed ferrite cores of different shapes (I, C and E) have been explored. Ferrite cores are utilized because of their property of high magnetic permeability associated with that of low electrical conductivity that mitigates the magnetic losses under high-frequency flux cycles. Sections and dimensions of the cores are shown in Fig. 5.1, which can be used as a general representation of different shapes. Each one of the shapes can be deducted from the general representation are shown in Fig. 5.2. Dimension D is set to 0 for the I- and C-cores whilst it is adjusted according to the turn number and their distance for the E-core. The I-core is simply a thin disk over which the coil lays, and is represented by the blue rectangle with dotted pattern. The C-core has the same base disk plus a rim around the perimeter, represented by the yellow parts with crossed pattern. The E-core has an additional central nucleus, represented by the green rectangle with oblique line pattern. Further to the chapter 4, where it has been demonstrated that the coupling coefficient of the spiral coil-coupling is greater, only this coupling has been considered in studying the core effects.

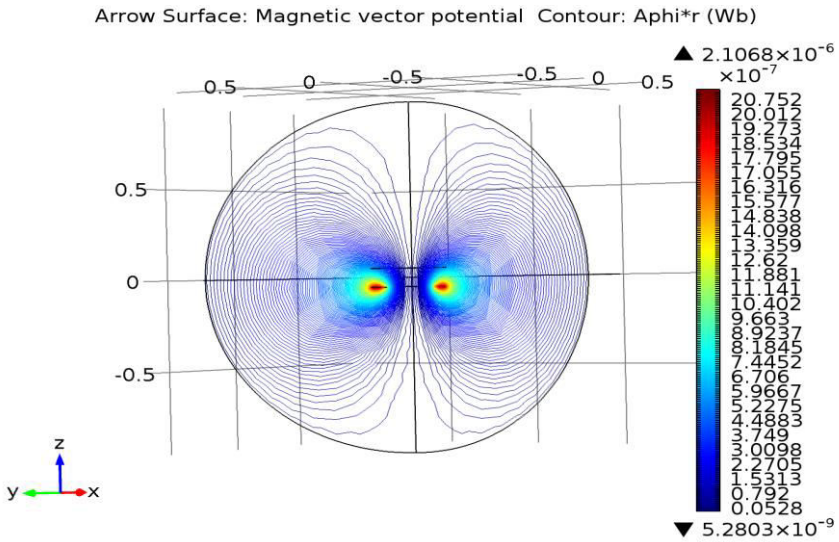

Fig. 5.3. Magnetic flux linkage with core for spiral coil (I-Core)

The inductive parameters of the cored spiral coil-coupling are also investigated to compare the performance achievable with the different cores. The plots of Figs. 5.4 and 5.5 give the self- and mutual inductance and the ensuing coupling coefficient obtained with the three core shapes as a function of the coil distance. It can be observed that i) self-inductance, mutual inductance and coupling coefficient of a cored coil-coupling are about 38%, 56% and 35% greater than the coreless one, ii) this feature is maintained over all the coil distances of interest, and iii) the self-inductance varies with the core shapes, even if in a marginal way, while mutual inductance is almost unaffected by them.

As a return, the usage of a core causes the self-inductances to be dependent on the coil distance *d*. Indeed, *L* decreases of about 5% when *d* passes from 0.1 m to 0.2 m. In the resonant WPT systems, to maximize efficiency and minimize sizing of the supply, the

operating frequency makes the coils resonating with capacitor banks connected in series or in parallel to them. Then, when *d* changes with respect to the designed value, the WPT systems with cored coil-coupling either work at a less efficiency or need tuning of the operating frequency to the actual inductance.

The effects of turn distance on a cored coil-coupling for the three core shapes are illustrated in Fig. 5.6. The plots show that the coupling coefficient i) is not much influenced by the turn distance, and ii) is almost constant for the higher values of t_d.

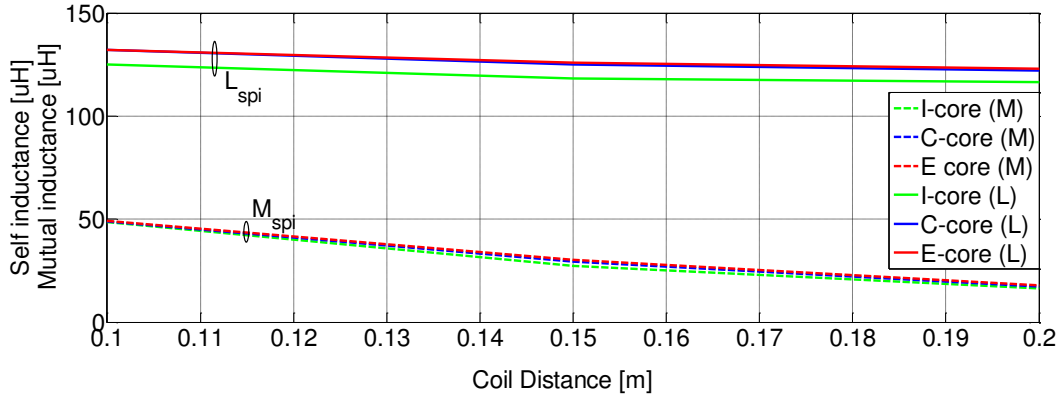

Fig. 5.4. Self- and mutual inductance vs. coil distance for cored spiral coil-coupling (N=15, t_d=7 mm).

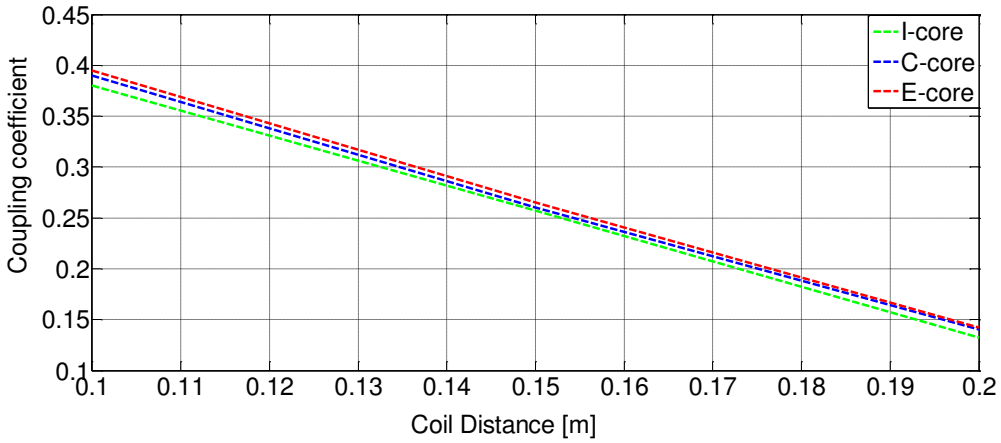

Fig. 5.5. Coupling coefficient vs. coil distance for cored spiral coil-coupling (N=15, t_d=7 mm).

5.3.1. Comparison

From the analysis of the spiral coil-coupling with the three core shape, it appears evident that i) a cored structure largely outperforms its coreless counterpart with regards the inductive parameters, and ii) the core shape marginally affects the coupling coefficient as shown by Figs. 5.5 and 5.6. Then, to reduce the cost of the coil-coupling, the I core is selected for the coil-coupling of the study case.

The impact of the misalignment on the inductive parameters of a spiral coil-coupling with I core is then investigated. The outcomes, plotted in Fig. 5.7 and Fig. 5.8, show that, despite its sensibility to the coil distance, the self-inductance is almost constant even at an high

misalignment. Instead, M decreases with the increase of the misalignment but its value remains of about 38% greater than the coreless counterpart. Correspondingly, the coupling coefficient also decreases but it exceeds more than twice the coreless counterpart when the misalignment is below 0.1 m. For higher values of the misalignment the advantage of the cored coil-coupling decreases up to become negligible when the misalignment reaches 0.2 m.

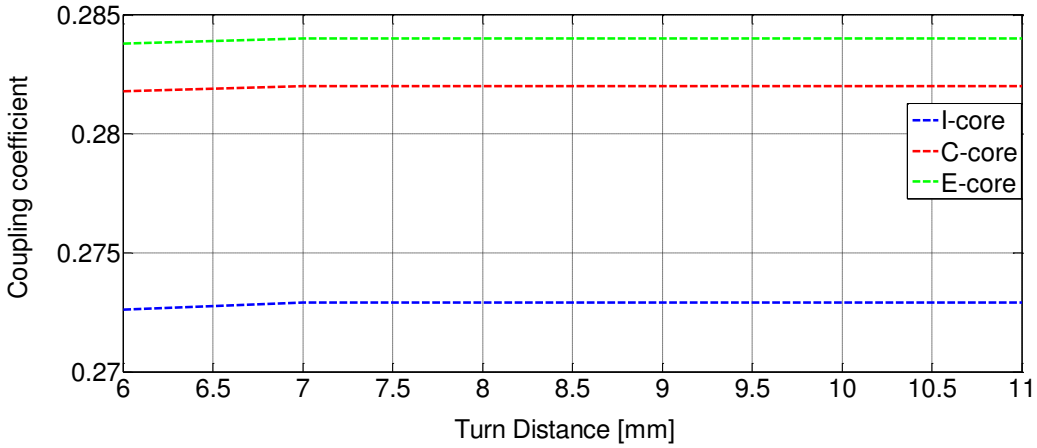

Fig. 5.6. Coupling coefficient vs. turn distance for the cored spiral coil-coupling (N=15).

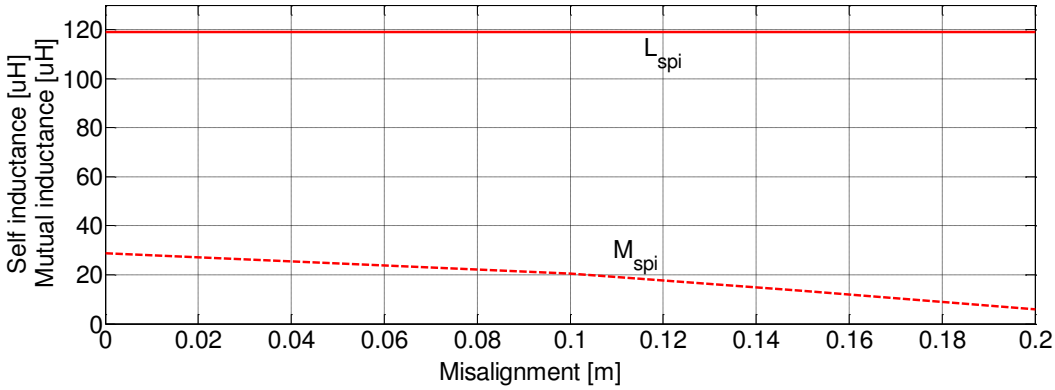

Fig. 5.7. Self and mutual inductances vs misalignment for spiral coil-coupling with I-core

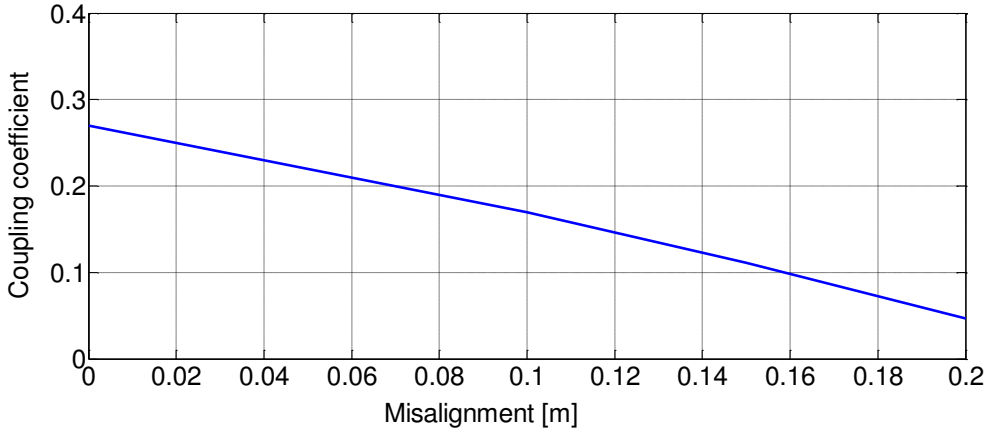

Fig. 5.8. Spiral coil-coupling coefficient vs. misalignment for I-core

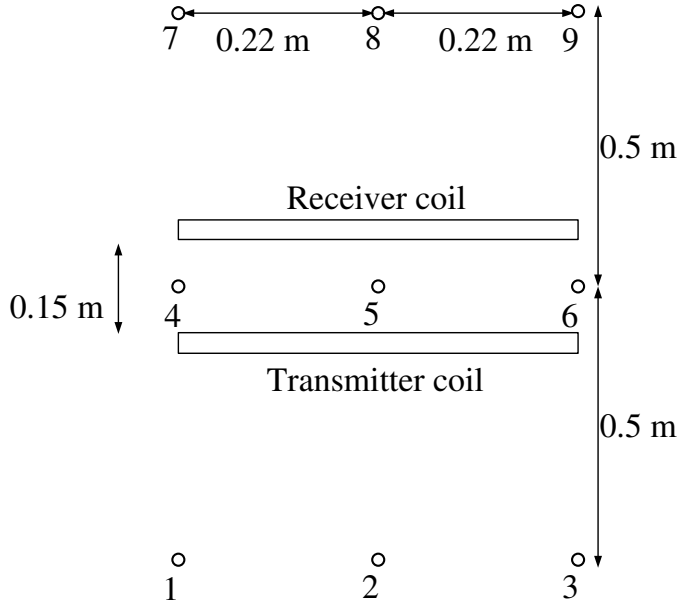

Fig. 5.9. Position of the points for electromagnetic measurements; the points lay on a vertical plane 0.3 m far from the coil edges.

5.3.2. Electromagnetic field

At present there are no standardized procedures to assess the human exposure to the electromagnetic fields generated by WPT battery chargers and a specific IEC rule is under development. It is taking into account the standard IEC 62233:2005 "Measurement methods for electromagnetic fields of household appliances and similar apparatus with regard to human exposure" as the WPT battery chargers fall within it. According to this standard, the electromagnetic field must be evaluated at 9 points laying on a vertical plane placed 0.3 m from the edges of the coils (testing plane); the position of the points in the plane is shown in Fig. 5.9. In each of these points, the maximum intensity of the field must be less than the limits prescribed for the humans by the directive 2013/35/EU of the European Parliament, where the limits are 100 μT and 170 V/m for the magnetic flux density and the electric field, respectively.

From the electrical equations of the WPT system entered with the inductive parameters found above, the maximum currents for the two coils are obtained: they are 10 A_{rms} for the receiver and 3 A_{rms} for the transmitter. A FEM analysis of the electromagnetic fields on the testing plane shows that the fields are within the allowed limits. As an example, Fig. 5.10 gives the magnetic flux density on that plane.

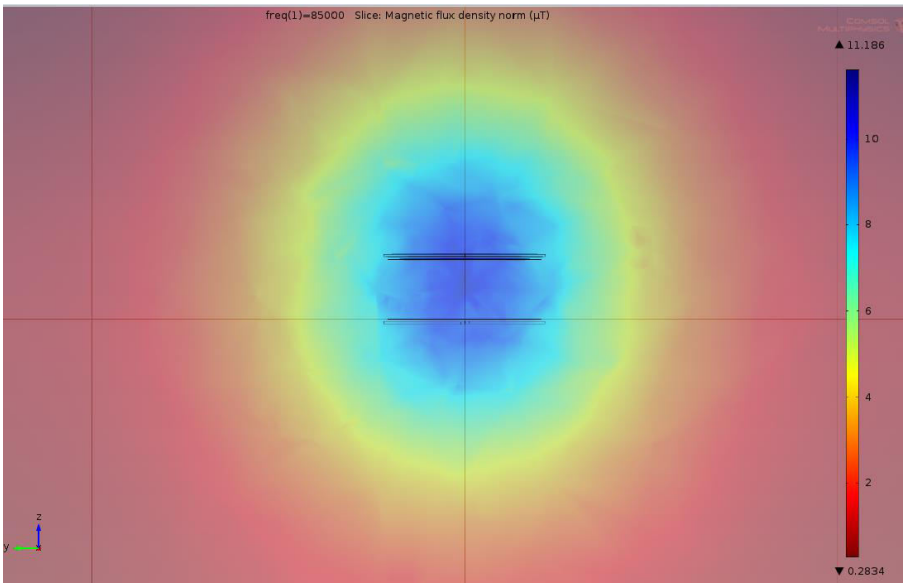

Fig. 5.10. Magnetic flux density in μT of the I-cored spiral coil-coupling on the testing plane.

5.4. Conclusion

This chapter dealt with analysis of inductive parameters of spiral coil with three shapes I-, C- and E-cores. Furthermore, it has been found that the I-, C- and E-cores give to the spiral coil-coupling about the same performance in terms of values of the inductive parameters and of their variation as a function of the coil distance and the coil misalignment. It has been also found that the electromagnetic fields are within the established limits for the human exposure. Further to the results of the analysis, a spiral coil-coupling setup with I core has been constructed and subjected to a campaign of measurements. They have substatiated the analysis carried out on the magnetic structure of the coil-coupling and have demonstrated that the fulfilment of the European directive on the human exposure to the electromagnetic fields.

5.5. References

[1] http://nptel.ac.in/courses/Webcourse Accessed online , 04/08/2014.

[2] http://www.mouser.com/pdfDocs/TI-Designing-a-Qi-compliant-receiver-coil.pdf. Accessed online , 04/08/2014.

[3] C.M.Zierhofer and E.S.Hochmair, “High-efficiency coupling-in sensitive transcutaneous power and data transmission via an inductive link,” *IEEE Trans. on Biomed. Eng,* vol. 37, no. 7, pp. 716–722, 1990.

Chapter 6

Resonant topologies of WPTS

Summary

In wireless power transfer system coils are separated by the distance. So the mutual inductance and coupling coefficient are greatly affected. This results in a large leakage inductance and small mutual inductance between two coils. This limits the power transfer capability of the primary coil to secondary coil.

To obtain higher mutual inductance, compensation of leakage inductance is required. This further helps to operate at resonance frequency so that impedance is purely resistive in nature. The compensation can be performed by inserting a capacitor with the primary and secondary inductances.

To compensate coil inductance and achieve a greater transfer of energy, capacitors are inserted in series or in parallel to the primary and secondary coils and are tuned to resonate at the supply frequency. Hence four fundamental topologies of resonant WPTS can be set up: series-series (SS), series-parallel (SP), parallel-series (PS) and parallel-parallel (PP). The main issue of this chapter deals with figures of merit for considered topologies.

6.1. Compensation and its need

In the wireless power transfer systems, large leakage inductances are associated with both the primary and secondary coils. To transfer power efficiently, requirement of large primary current is necessary. This large primary current generates the losses in the system, which leads to poor efficiency. A method to overcome this problem is to compensate the reactive elements by using capacitors. So that only resistive element remains in the system, which reduces the losses, thereby efficiency will increase [1].

6.2. Behavior of the compensation capacitance

Behavior of capacitor depends on the placement in the circuit and different possible compensation topologies can be classified as Series-Series (SS) compensation, Series-Parallel (SP) compensation, Parallel-Series (PS) compensation, Parallel-Parallel (PP) compensation. Selection of both primary and secondary compensation capacitances are based on two criterions [2].

1. The secondary capacitance is chosen as the first step. This is done in such a manner so as to compensate the secondary leakage inductance and the mutual inductance. This type of compensation would lead to an improvement in the power transferred to the load.
2. The primary capacitance is then chosen such that it considers the WPTS inductance of the entire circuit.

6.3. Analysis of compensation topology structures

The choice among the topologies is different for various applications and parameters. Each different topology has its own advantages and drawbacks. The choice has to be made according to the specifications of the type of application to be developed. The computational analysis for different topologies is explained as follows [3].

6.3.1. SS Topology

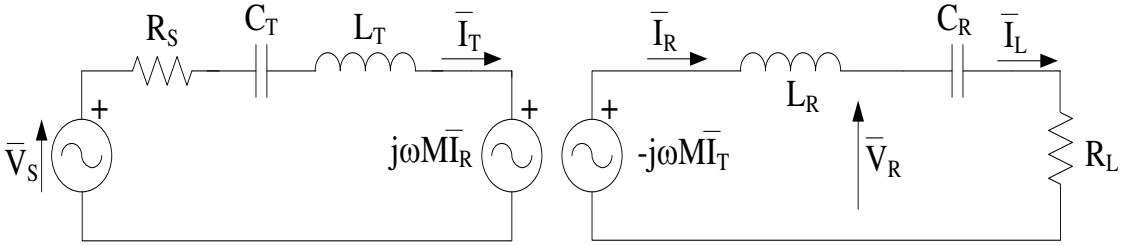

Fig.6.1. Series-Series (SS) topology

The figures of merit for the SS topology is already discussed in (3.28)-(3.31) in the Chapter 3, so discussion continued with other topologies.

6.3.2. SP Topology

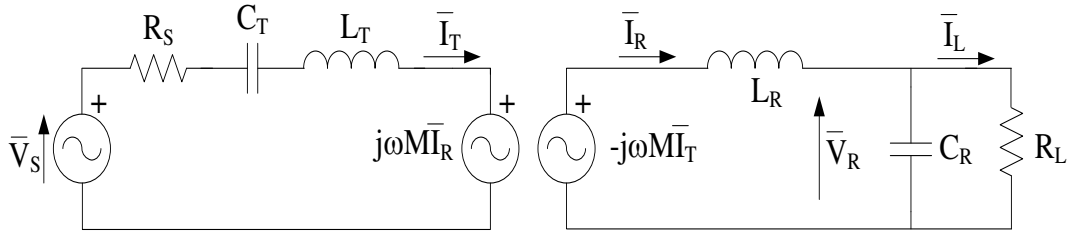

Fig.6.2. Series-Series (SP) topology

By Fig.6.2, the impedances of the transmitting and receiving sections of the resonant WPTSs with SP topology are

$$\begin{aligned} \dot{Z}_{T,sp} &= R_S + j\omega L_T - j\frac{1}{\omega C_T} \\ \dot{Z}_{R,sp} &= j\omega L_R + \frac{1}{\frac{1}{R_L}+j\omega C_R} \end{aligned} \qquad (6.1)$$

Resonant condition for the transmitting section is still given by the first of (3.25) while two resonance conditions can be envisaged for the receiving section, each of them leading to a different expression of the secondary impedance. One condition is given by the second of (3.25) and the other one, obtained by imposing that the impedance of the receiving section is purely resistive, is given by

$$L_{R,sp} = \frac{C_R R_L^2}{1+\omega^2 C_R^2 R_L^2} \tag{6.2}$$

Under the second of (6.1), $\dot{Z}_{R,sp}$ results in

$$\dot{Z}_{R,sp} = \frac{R_L}{1+\omega^2 C_R^2 R_L^2} + j\frac{\omega L_R}{1+\omega^2 C_R^2 R_L^2} \tag{6.3}$$

Under (6.2), $\dot{Z}_{R,sp}$ results in

$$\dot{Z}_{R,sp} = \frac{R_L}{1+\omega^2 C_R^2 R_L^2} \tag{6.4}$$

Condition (6.2) is depending on the load. In applications where the load is variable, such as in EV battery charging, meeting of (6.4) entails that i) the supply frequency must be continuously tuned to maintain the resonance condition in the receiving section, and ii) if the resonance condition is maintained in the receiving section, this can be not done in the transmitting section where the resonance frequency is fixed and established by the first of (3.25). For this reason, the second of (3.25) is here taken as the resonance condition for the receiving section, and the expressions of $\dot{Z}_T$ and $\dot{Z}_R$ given by the first of (3.26) and by (6.3) are hereafter used.

It is worth to note that the quality factors of the receiving and transmitting sections in the resonance conditions can be expressed as

$$Q = \frac{1}{\omega C R} \tag{6.5}$$

Substitution of the first of (3.26) and (6.3) into (3.2) yields

$$\eta_{SP} = \frac{k^2 Q_T}{Q_R + k^2 Q_T} \tag{6.6}$$

$$\alpha_{SP} = \frac{\sqrt{k^4 Q_R^2 Q_T^2 + (Q_R + k^2 Q_T)^2}}{k^2 Q_T} \tag{6.7}$$

$$\beta_{SP} = \frac{\sqrt{1+Q_R^2}}{Q_R} \tag{6.8}$$

The PUMLRC results in

$$I_{L,pu,SP} = \frac{k^2 Q_R Q_T}{\sqrt{k^4 Q_R^2 Q_T^2 + (Q_R + k^2 Q_T)^2}} \tag{6.9}$$

6.3.3. PS topology

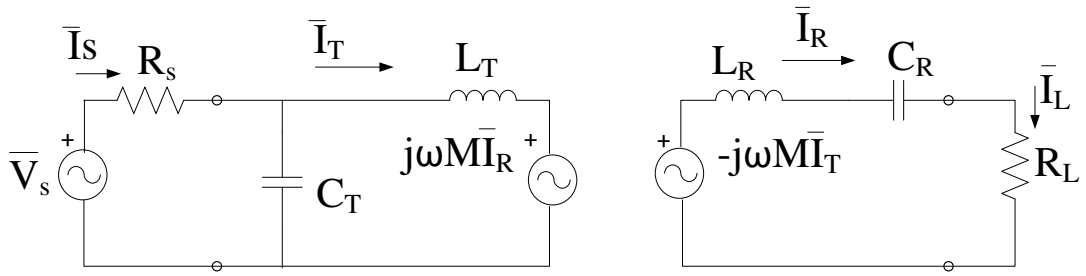

Fig.6.3. Parallel-Series (PS) topology

By application of superposition theorem, transmitter current $\bar{I}_{T,ps}$ and source current $\bar{I}_{s,ps}$ are expressed as

$$\bar{I}_{T,ps} = \frac{-j\left(\frac{\bar{V}_S}{\omega L_T}\right)(R_S+j\omega L_T)\dot{Z}_2}{[\dot{Z}_2 R_S+\omega^2 M^2(1+\omega^2 C_T^2 R_S^2)]+j\omega L_T} \qquad (6.10)$$

$$\bar{I}_{s,ps} = \frac{j(\omega M)^2\left(\frac{\bar{V}_S}{\omega L_T}\right)(R_S+j\omega L_T)(1-j\omega C_T R_S)}{[\dot{Z}_2 R_S+\omega^2 M^2(1+\omega^2 C_T^2 R_S^2)]+j\omega L_T} \qquad (6.11)$$

Receiver current $\bar{I}_{R,ps}$ is expressed as

$$\bar{I}_{R,ps} = \frac{-(\omega M)\left(\frac{\bar{V}_S}{\omega L_T}\right)(R_S+j\omega L_T)}{[\dot{Z}_2 R_S+\omega^2 M^2(1+\omega^2 C_T^2 R_S^2)]+j\omega L_T} \qquad (6.12)$$

Then figures of merit for PS topology are expressed as

$$\eta_{ps} = \frac{(Q_T^2+1)/Q_T}{Q_T+\left(\frac{1}{Q_T}\right)(1+k^2 Q_R(1+Q_T/Q_T))} \qquad (6.13)$$

$$\alpha_{ps} = \frac{\sqrt{\left[k^2 Q_R(Q_T^2+1)/Q_T\right]^2+\left[Q_T+\left(\frac{1}{Q_T}\right)(1+k^2 Q_R(Q_T^2+1)/Q_T)\right]^2}}{(Q_T^2+1)/Q_T} \qquad (6.14)$$

$$\beta_{ps} = \sqrt{1+Q_R^2} \qquad (6.15)$$

$$I_{L,pu,pS} = \frac{k^2 Q_R\sqrt{(Q_T^2+1)}}{\sqrt{\left[1+k^2 Q_R(Q_T^2+1)/Q_T\right]^2+Q_T^2}} \qquad (6.16)$$

6.3.4. PP topology

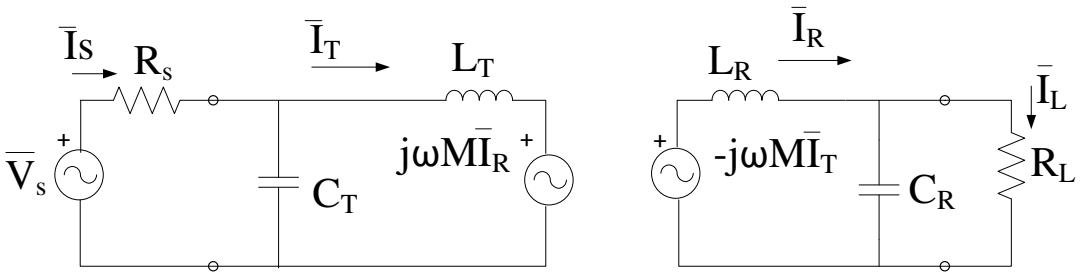

Fig.6.4. Parallel-Series (PP) topology

In PP topology $\bar{I}_R$ and $\bar{I}_L$ are different, so $\bar{I}_L$ is given by

$$\bar{I}_L = \frac{\bar{I}_R}{|1+j\omega C_R R_L|} \tag{6.17}$$

Then figures of merit for PP topology are expressed as

$$\eta_{pp} = \frac{(Q_T^2+1)/Q_T}{Q_T+\left(\frac{1}{Q_T}\right)\left(1+\frac{k^2(Q_R^2+1)(Q_T^2+1)}{Q_T Q_R}\right)} \tag{6.18}$$

$$\alpha_{pp} = \frac{\sqrt{\left[\frac{k^2(Q_R^2+1)(Q_T^2+1)}{Q_T Q_R}\right]^2+\left[Q_T+\left(\frac{1}{Q_T}\right)\left(\frac{k^2(Q_R^2+1)(Q_T^2+1)}{Q_T Q_R}\right)\right]^2}}{(Q_T^2+1)/Q_T} \tag{6.19}$$

$$\beta_{pp} = \frac{\sqrt{1+Q_R^2}}{Q_R} \tag{6.20}$$

$$I_{L,pu,pp} = \frac{k^2\sqrt{(Q_R^2+1)}\sqrt{(Q_T^2+1)}}{\sqrt{\left[1+k^2(Q_R^2+1/Q_R)(Q_T^2+1/Q_T)\right]^2+Q_T^2}} \tag{6.21}$$

6.4. Characteristic evaluation of topologies

The characteristics of the resonant WPTSs with all topologies have been evaluated and compared by help of the above-found expressions for the figures of merit, in the view of using the WPTSs to charge the batteries of the EVs. For this application, the final load is the battery. Its charging current is kept constant until the battery voltage increases up to the maximum value; then the voltage is kept constant whilst the charging current decreases to zero. Therefore, the battery behaves as a resistor, with resistance value that starts from a minimum value and continues to increases as the charging process goes on. The resistance representing the battery must then be referred to the receiving load to obtain RL. As an example, Fig. 6.5 reports the idealized charging process of the electric city car discussed in [3], where RB is given by VB/IB. The figure indicates that RL increases of about 100 times during the charging process. Therefore it is of interest to evaluate the characteristics of the resonant WPTSs under varying load.

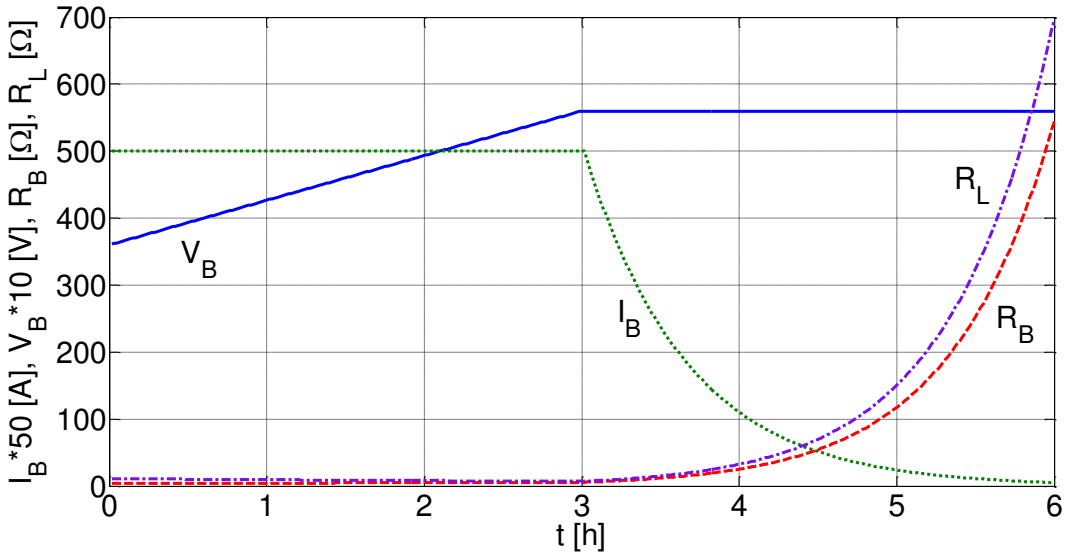

Fig.6.5. Example of change in the equivalent load resistance during the charging process of electric vehicle batteries.

6.4.1 Characteristics under varying load

(i) SS and SP topology

A varying load changes the quality factor of the receiving section while that one of the transmitting section remains constant. Then, the characteristics have been evaluated (and graphed) as a function of Q_R and for three different values of Q_T, namely 100, 300 and 1000. The coupling coefficient has been set at 0.2, which is common value for EV battery charging application. The characteristics of the inductive WPTSs have been also graphed, according to the expressions found in Chapter 3. They have been used as a point of reference for the resonant WPTSs.

The graphs of the characteristics are traced according to the following convention: solid blue lines for the resonant WPTSs with SS topology, dashed red lines for the resonant WPTSs with SP topology, and dotted green lines for the inductive WPTSs.

Fig. 6.6 reports the graphs of the efficiency for the resonant topologies. The graphs are symmetrical around Q_R=1, with the efficiency of the SS topology that outdoes the SP topology for high values of Q_R whilst the opposite occurs for low values of Q_R. In particular, the efficiency of the SS topology increases with Q_R, tending to 1 for high values of Q_R. The increase rate is fast for Q_R around 0.1 and reduces at both lower and higher values of Q_R. The graphs, moreover, show that the efficiency increases with Q_T for both the topologies.

The graphs of the efficiency of the inductive WPTSs, as obtained from (3.19), are also reported in Fig.6.6. They show that the inductive WPTSs have a lower efficiency over all the range of Q_R, the value of Q_T being equal. For instance, the maximum efficiency of the inductive WPTSs, reached for Q_R=1, is

$$\eta_{I,max} = \frac{k^2 Q_T}{2+k^2 Q_T} \qquad (6.22)$$

and is still less than the efficiency of the resonant WPTSs for Q_R=1, given by

$$\eta_{SS,SP} = \frac{k^2 Q_T}{1+k^2 Q_T} \qquad (6.23)$$

Furthermore, the graphs in Fig. 6.6. point out that the SS topology has an efficiency a little higher than the inductive WPTSs at low values of Q_R but the spread increases with Q_R up to become very large at high values of Q_R; again, a dual behavior is exhibited by the SP topology.

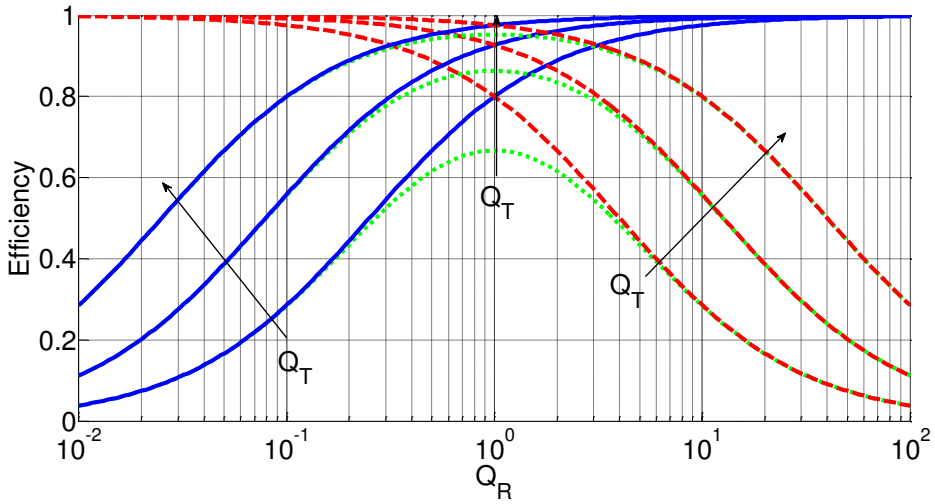

Fig.6.6. Efficiency of resonant WPTSs with SS and SP topology, and of an inductive WPTS vs. Q_R for different values of Q_T.

Fig. 6.7 reports the graphs of the PSSF. They show that i) the PSSF of the SS topology decreases as soon as Q_R and Q_T increase, and ii) the PSSF of the SP topology is nearly independent on Q_T and its behavior vs. Q_R is the opposite of the SP topology. Regarding the inductive WPTSs, their PSSF is nearly independent on Q_T and takes a much higher value over all the range of Q_R. This means that, even if operated at the maximum efficiency, i.e. at Q_R=1, the power supply of the inductive WPTSs must be sized for an apparent power 49 times the active power transferred to the load. Instead, for Q_R=1, the power supply of the SS topology must be sized for an apparent power that, depending on Q_T, is between 1 to 1.25 times the active power transferred to the load, and for the SP topology is between 1.4 to 1.6.

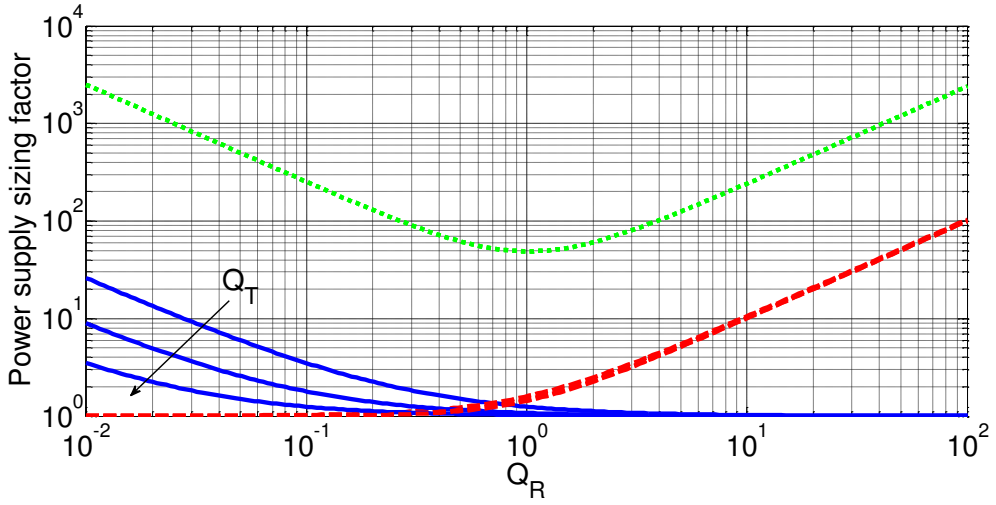

Fig.6.7. PSSF of resonant WPTSs with SS and SP topology, and of an inductive WPTS vs. Q_R for different values of Q_T.

Fig. 6.8 reports the graphs of the RCSF. As for the efficiency, the graphs of the RCSF are symmetrical around Q_R=1. In particular, the RCSF of the SS topology tends i) to 1 for low values of Q_R, and ii) to Q_R for high values of Q_R. Note that the RCSF of the inductive WPTSs is equal to 1, irrespectively of Q_R.

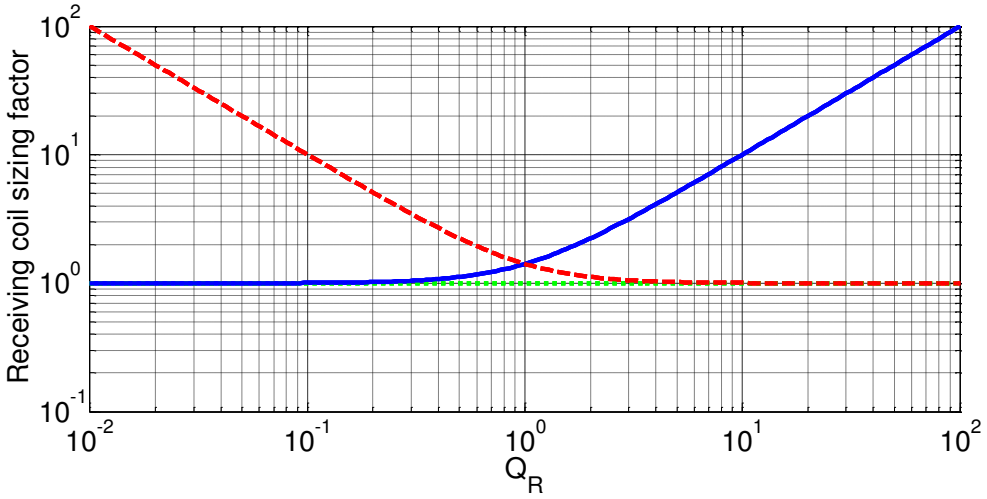

Fig.6.8. RCSF of resonant WPTSs with SS and SP topology, and of an inductive WPTS vs. Q_R for different values of Q_T.

Fig. 6.9 reports the graphs of the PUMLRC. They show that the PUMLRCs of both the resonant WPTSs tend to 1 for high values of Q_R, irrespectively of Q_T. Instead, for low values of Q_R, the resonant WPTSs have a quite different behavior, with the PUMLRC of the SS topology that exceeds the SP topology and becomes higher and higher as the value of Q_T for the SS topology increases, the SP topology having a PUMLRC nearly independent of Q_T. Regarding the inductive WPTSs, their PUMLRC is nearly independent of Q_T and, as a function of Q_R, its behavior is like that of the SP topology but at much lower values.

Incidentally, a WPTS with a nearly constant PUMLRC has the feature of requiring only a small adjustment of the voltage of the power supply to keep constant the current into a varying load.

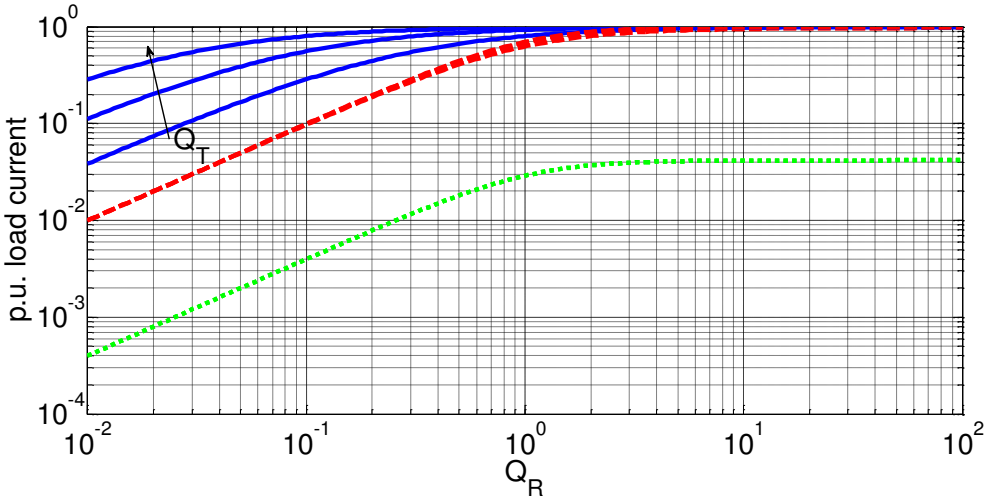

Fig.6.9. PUMLRC of resonant WPTSs with SS and SP topology, and of an inductive WPTS vs. Q_R for different values of Q_T.

(ii) PS and PP topology

The characteristics of PS and PP topologies are evaluated under load and coupling variations. For this section solid blue and dotted red lines represent PS and PP topology respectively.

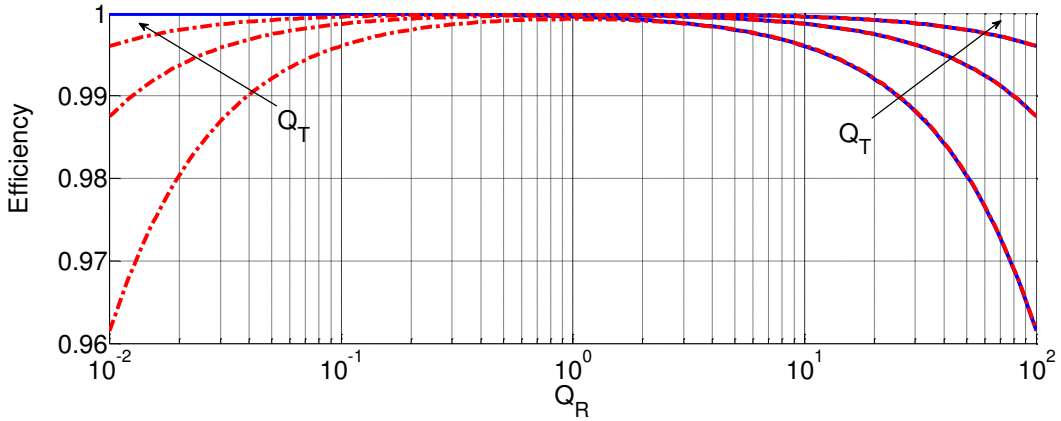

Fig.6.10. Efficiency of resonant WPTSs with PS and PP topology vs. Q_R for different values of Q_T.

The efficiency of PS and PP topologies reported in Fig.6.10, which shows the efficiency of PS topology is higher (unity) for a lower value of Q_R. It is constant up to Q_R=1, and decreases monotonically for higher values of Q_R. Efficiency of PP topology is lower compared to PS

topology for the lower values of Q_R and, at Q_R=1,efficiency is maximum for both topologies. Efficiency of PP topology shows same behavior of PS topology for higher values of Q_R.

Fig. 6.11 reports graph of PSSF, where it shows that (i) for PS topology it is independent of Q_T and almost constant for all values of Q_R, (ii) for the PP topology, PSSF decreases up to Q_R=1 and increases at higher values of Q_R. The PSSF of this topology takes much higher values for all range of Q_R.

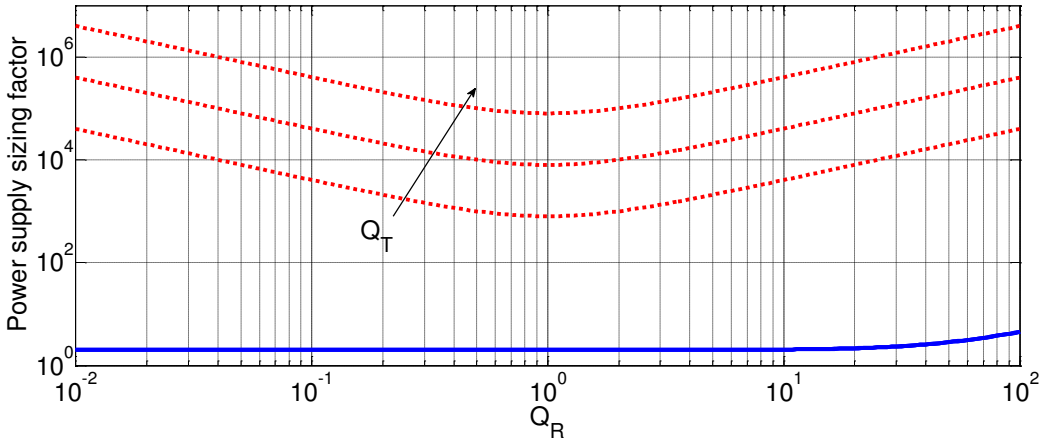

Fig.6.11. PSSF of resonant WPTSs with PS and PP topology vs. Q_R for different values of Q_T.

RCSF of PS and PP topologies are the same as SS and SP topologies respectively as RCSF depends only on receiving coil parameters only. PUMLRC of PS and PP topologies as a function of Q_R is reported in Fig.6.12. They show that PUMLRC of PS topology is increasing with Q_R and reaches up to 1 for Q_R = 100. On the other hand PUMLRC of the PP topology is constant for the lower value of Q_R, it continues its behavior up to Q_R = 1 and increases monotonically for the higher values of Q_R. For all the values of Q_R, PUMLRC of PS topology is higher than PP topology.

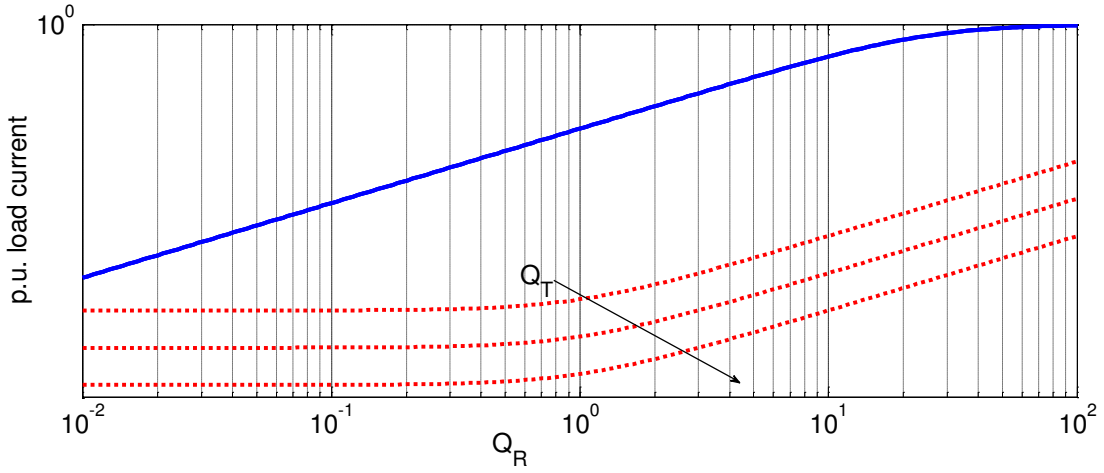

Fig.6.12. PUMLRC of resonant WPTSs with PS and PP topology vs. Q_R for different values of Q_T.

6.4.2 Characteristics under varying k

EVs may be not parked just above the charging slots and, consequently, the transmitting coil may be not perfectly aligned along the receiving coil. This leads to a coupling coefficient lower than the expected one. Since most of the figures of merit (i.e. efficiency, PSSF and PUMLRC) are affected by the coupling coefficient, it is also of interest to evaluate the characteristics of the resonant WPTSs under varying coupling coefficient. The characteristics are evaluated for three values of Q_R, i.e. Q_R=0.1, 1 and 10, and for Q_T=316, and the relevant graphs are traced according to the convention previously used for the line color and style.

(i) SS and SP topologies

The graphs of the efficiency of the resonant WPTSs as a function of the coupling coefficient are reported in Fig. 6.13 together with those of the efficiency of the inductive WPTSs. The graphs show that the efficiency of the resonant WPTSs with SS topology sharply increase with k when Q_R is greater than 1. A sharp increase also occurs for the resonant WPTSs SP topology when Q_R is lower than 1 as well as for the inductive WPTSs for Q_R=1. The increase is much less sharply for values of Q_R beyond the mentioned ones.

Regarding the inductive WPTSs, inspection of (3.19), (3.28) and (6.6) shows that their efficiency is about equal to the resonant WPTSs with SS topology for small values of Q_R, and to the resonant WPTSs with SP topology for high values of Q_R. This explain why the graphs are superimposed for Q_R=0.1 and for Q_R=10, respectively. Moreover, it can be recognized from (3.19) and Fig. 6.6 that the efficiency of the inductive WPTSs takes the same value for a given value of Q_R and for its inverse $1/Q_R$, irrespectively of the value of k. Consequently, the graph of the efficiency of the inductive WPTSs for Q_R =0.1 coincides with that one for Q_R =10.

As per physical perceptions, the efficiency for both the resonant WPTSs and the inductive WPTSs increases with the coupling coefficient monotonously. For k=1, from (3.28), (6.6) and (3.19), the efficiencies of the resonant WPTSs are respectively.

$$\eta_{SS} = \frac{Q_R Q_T}{1+Q_R Q_T} \qquad (6.24)$$

$$\eta_{SP} = \frac{Q_T}{Q_R+Q_T} \qquad (6.25)$$

whilst that one of the inductive WPTSs is

$$\eta_I = \frac{Q_R Q_T}{1+Q_R^2+Q_R Q_T} \qquad (6.26)$$

which is evidently lower than both (6.24) and (6.25).

The sensitivities of the efficiencies of the resonant WPTSs with respect to the coupling coefficient are given by

$$\frac{\delta\eta_{SS}}{\delta k} = 2k\frac{Q_R Q_T}{(1+k^2 Q_R Q_T)^2} \qquad (6.27)$$

$$\frac{\delta\eta_{SP}}{\delta k} = 2k\frac{Q_R Q_T}{(Q_R+k^2 Q_T)^2} \qquad (6.28)$$

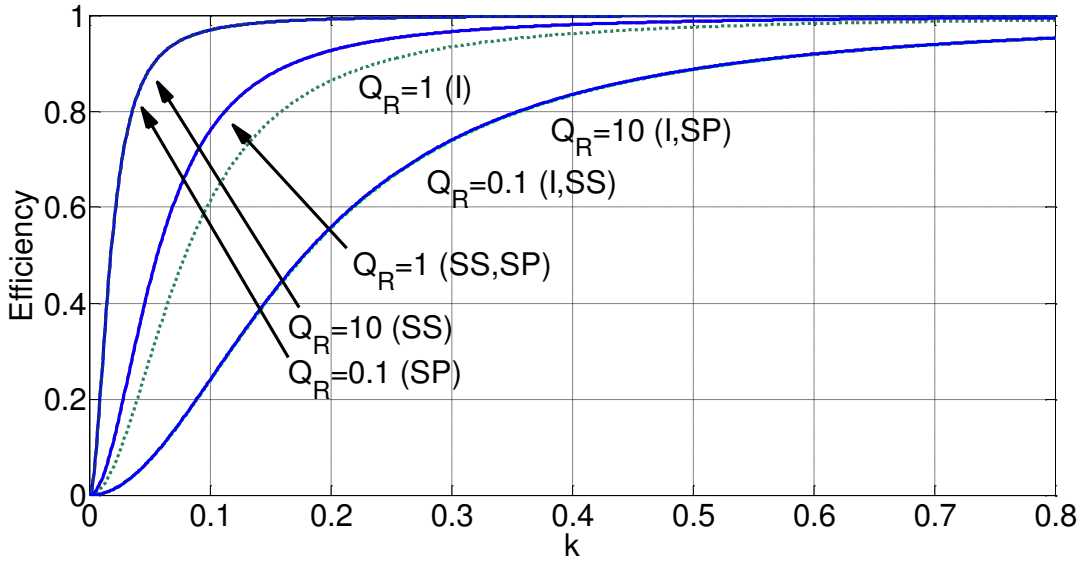

Fig. 6.13. Efficiency of resonant WPTSs with SS and SP topology, and of inductive WPTSs vs. k.

The graphs obtained by (6.27) and (6.28) are reported in Fig. 6.14 as a function of the coupling coefficient together with those of the sensitivity of the efficiency of the inductive WPTSs, which is given by

$$\frac{\delta\eta_I}{\delta k} = 2k\frac{Q_R Q_T(1+Q_R^2)}{(1+Q_R^2+k^2 Q_R Q_T)^2} \qquad (6.29)$$

The graphs of Fig. 6.14 show that the sensitivity of the efficiency with respect to the coupling coefficient is higher for both the resonant and the inductive WPTSs when k ranges between 0 and 0.1. As regards the resonant WPTSs, the maximum of the sensitivity increases with Q_R for the SS topology whilst the opposite occurs for the SP topology. For the inductive WPTSs the maximum sensitivity is reached for Q_R=1.

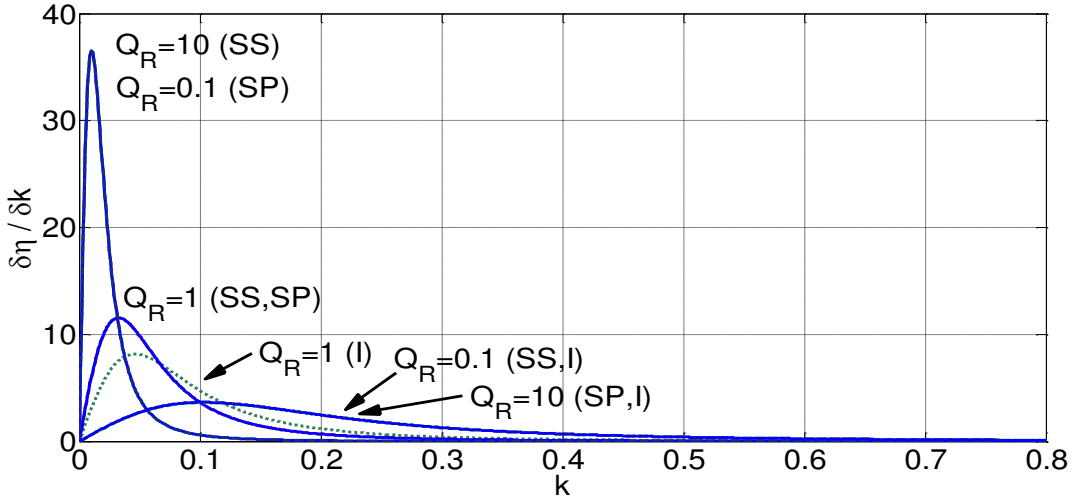

Fig. 6.14. Sensitivity of the efficiency of resonant WPTSs with SS and SP topology, and of inductive WPTSs vs. k.

Fig. 6.15 reports the graphs of the PSSF as a function of the coupling coefficient. They show that i) the PSSF decreases with k for both the resonant and the inductive WPTSs, ii) the resonant WPTSs. with the SS topology have a PSSF lower than the SP topology; as a return, they are more sensitive to the changes of k in the range of k between about 0.05 and 0.3, and iii) for given values of QR and QT, the PSSF of the resonant WPTSs outdoes the inductive WPTSs over all the range of k.

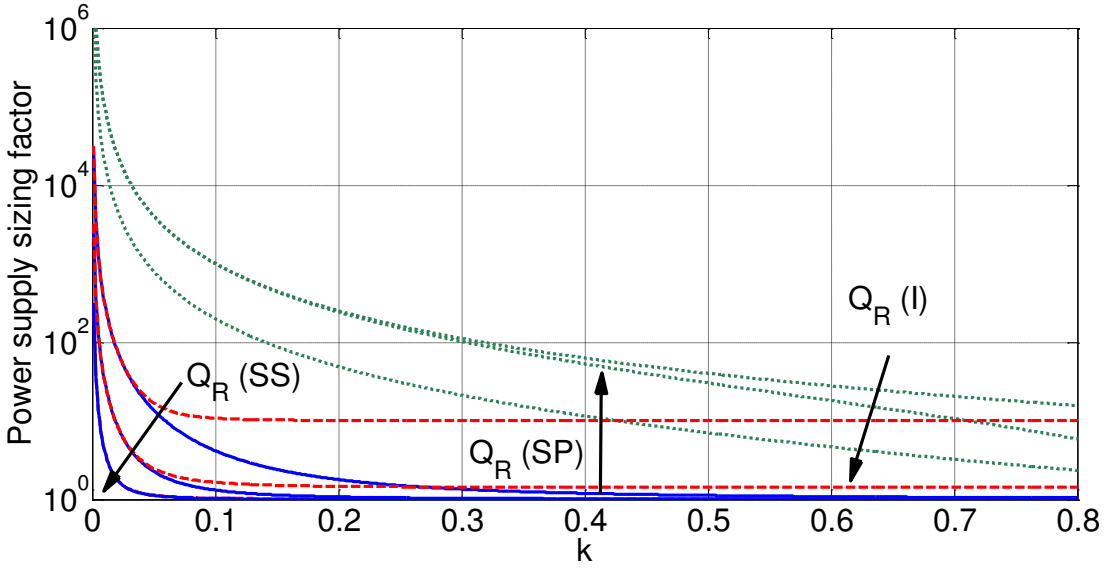

Fig. 6.15. PSSF of resonant WPTSs with SS and SP topology, and of inductive WPTSs

Fig. 6.16 reports the graphs of the PUMLRC as a function of the coupling coefficient. They show that the PUMLRC of the WPTSs, whether resonant or inductive, has a behavior comparatively similar to that of the PSSF in Fig. 6.12, by matching the decreasing values of the PUMLRC with the increasing values of the PUMLRC.

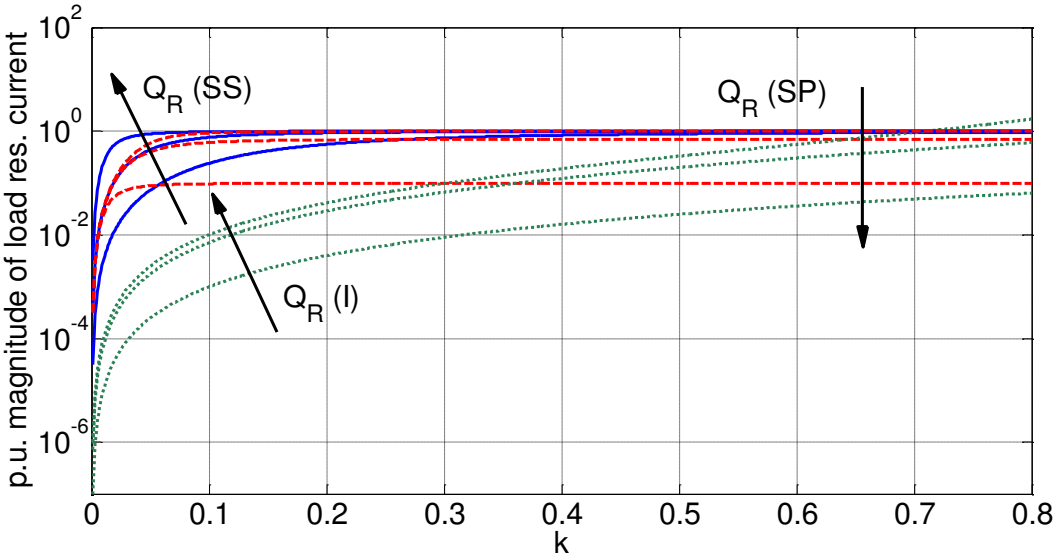

Fig. 6.16. PUMLRC of resonant WPTSs with SS and SP topology, and of inductive WPTSs vs. k

(ii) PS and PP topologies

The analysis under varying k is analyzed in the same manner as SS and SP topologies for PS and PP topologies. The graphs of efficiency against coupling coefficient for different values of Q_R is plotted in Fig.6.17. The graph shows for lower values of k efficiency is higher

and decreases for increasing value of k. All the topologies show the same behavior for all values of k.

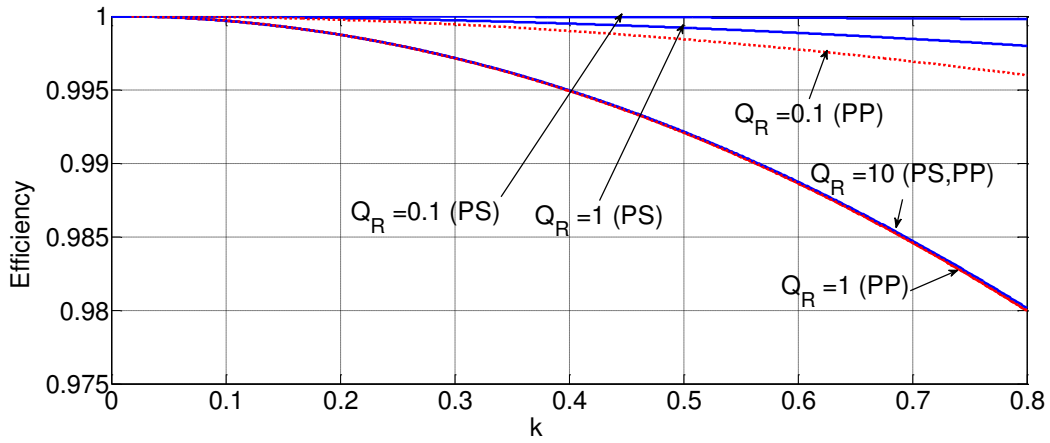

Fig.6.17. Efficiency of resonant WPTSs with PS and PP topology vs. k.

Fig.6.18 reports the graph of PSSF against coupling coefficient. They show that for the lower values k, PSSF of PS is constant across k for lower values of Q_T, but at higher value of k, for Q_T=1000 the PSSF is slightly higher compared to other values of Q_T. PSSF of the PP topology, is increasing with the increasing k. and it takes much higher values compared to PS topology.

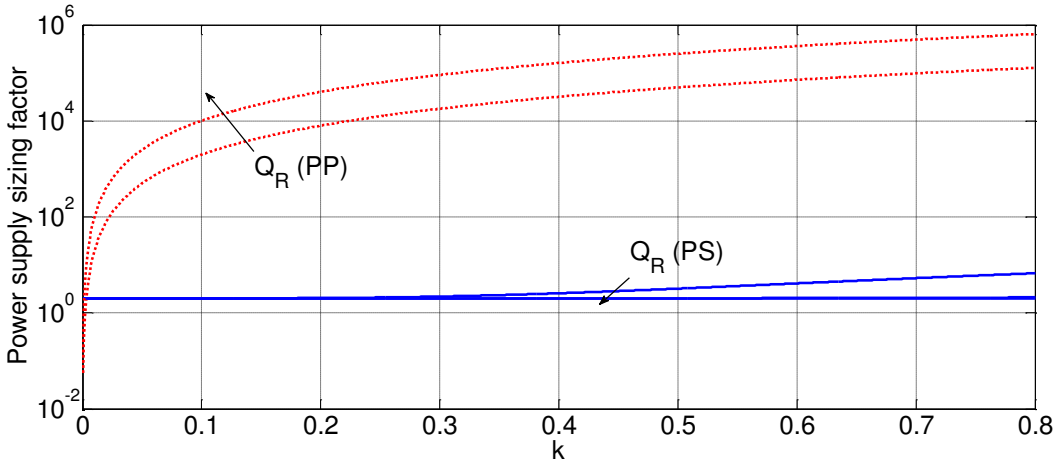

Fig.6.18. PSSF of resonant WPTSs with PS and PP topology vs. k.

PUMLRC of PS and PP topologies as a function of k are plotted in Fig. 6.19. For the starting values of k, PULMRC is sudden increasing then increasing with increasing values of k for PS topology. And for PP topology it increases suddenly for very low values k and then remains constant for the increasing values of k.

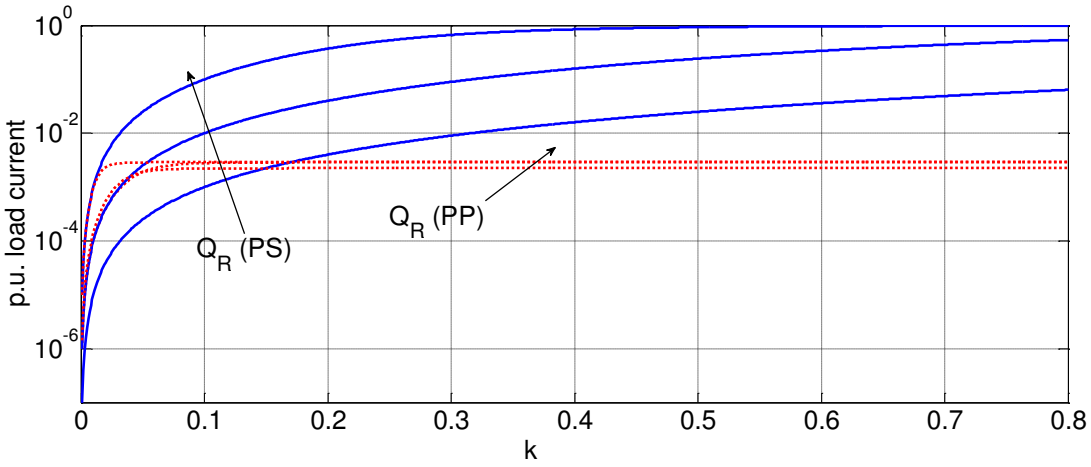

Fig.6.19. PUMLRC of resonant WPTSs with PS and PP topology vs. k.

6.5. Comparative analysis of different topologies

Comparative analysis of different topologies are performed to select the best suitable one for the WPTS. Fig.6.20 reports the graph of efficiency against Q_R. By observing the graph for the lower values of Q_R, efficiency of SP and PS topologies are high. For SS topology efficiency increases for the higher values of Q_R and PS and PP topologies maintains higher efficiency most of the value of Q_R.

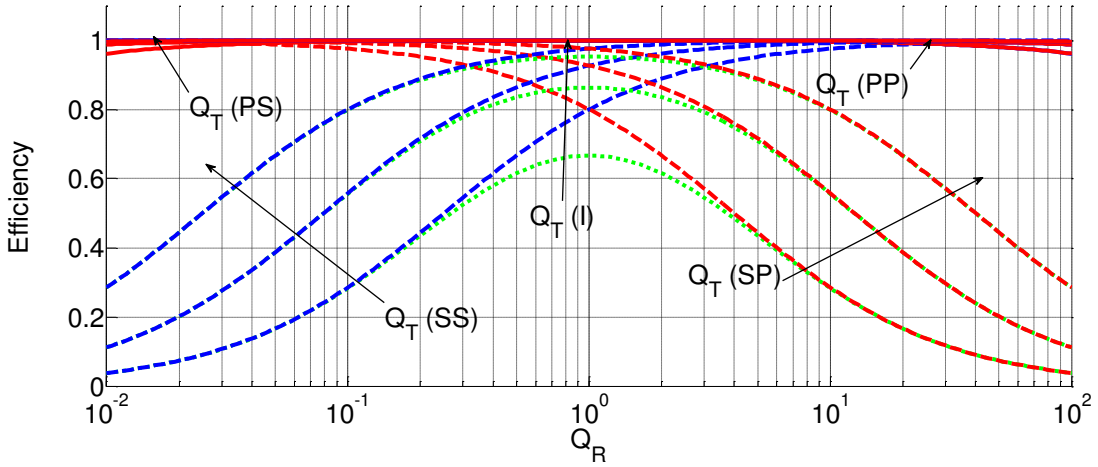

Fig.6.20. Efficiency of different topologies and of inductive WPTSs vs. Q_R.for different Q_T

Fig.6.21 reports performance of efficiency under varying k, for different values of Q_R. From the graph PS and PP topologies maintains higher values throughout k and the SS topology behavior is the same as PS and PP for the for higher values of k. SP and inductive coupling follow the same behavior of SS but efficiency is less.

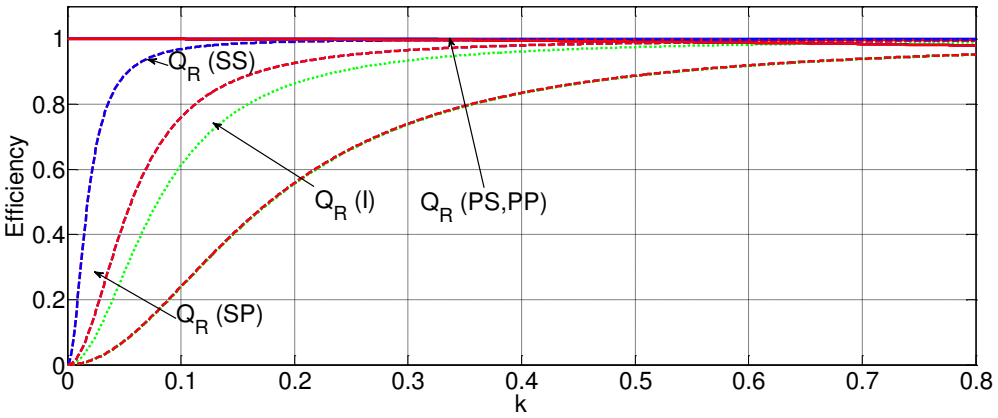

Fig.6.21. Efficiency of resonant WPTS and inductive WPTSs vs. k for different Q_R

Performance evaluation of PSSF against Q_R is observed in Fig 6.22. The graph shows that, except for PS and SP topology, the remaining ones decreases up to Q_R and only SS topology continues its behavior even for the higher values. The PSSF of PS topology is constant and little increases for the value above 10. On the other hand by observing the plot reported in Fig.6.23, for the initial value of k PSSF is quite high and then decreases monotonically for increased value of k except for SP topology. SP topology shows opposite behavior of other topologies. PS topology follows the same behavior of under varying load.

PUMLRC is increasing with the increasing Q_R except for PP topology up to value Q_R =1. For the value beyond 1 PUMLRC is increasing for all topologies except inductive where it takes the constant value. For the varying k, behavior of PUMLRC increases with increasing values of k except PP topology where it stays constant for the values after k=0.05. This is well shown in Fig.6.24 and Fig.6.25 respectively.

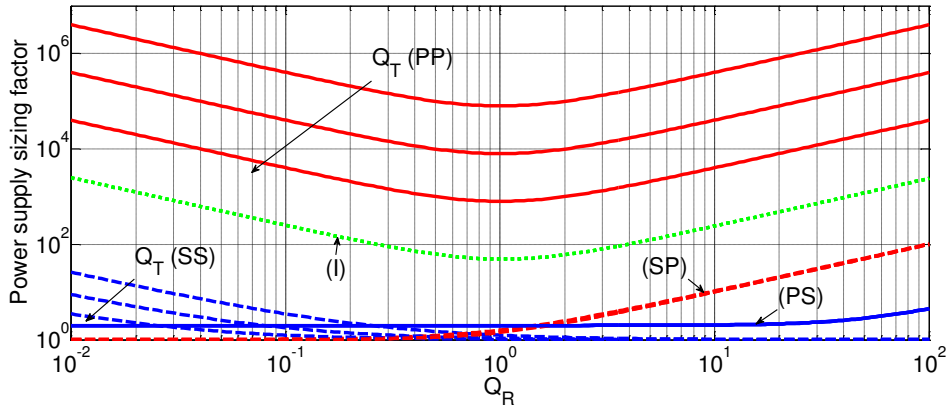

Fig 6.22. PSSF of resonant WPTS and of inductive WPTSs vs. Q_R for different Q_T

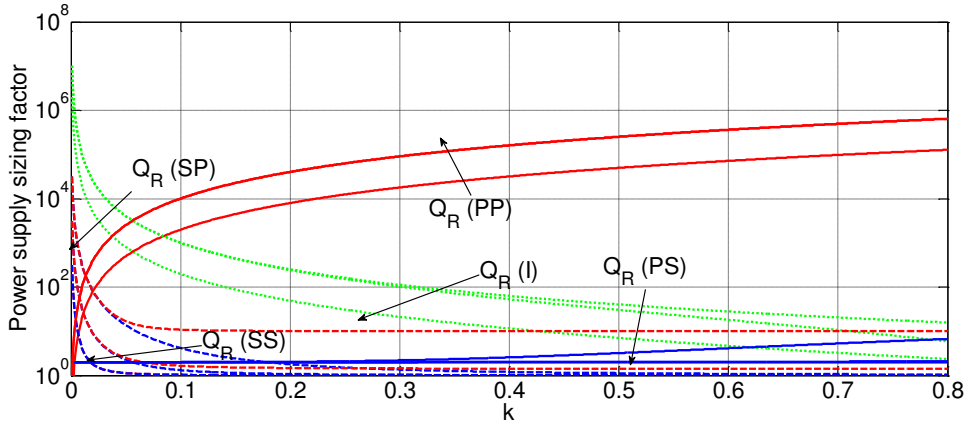

Fig.6.23. PSSF of resonant WPTS and of inductive WPTSs vs.k for different Q_R

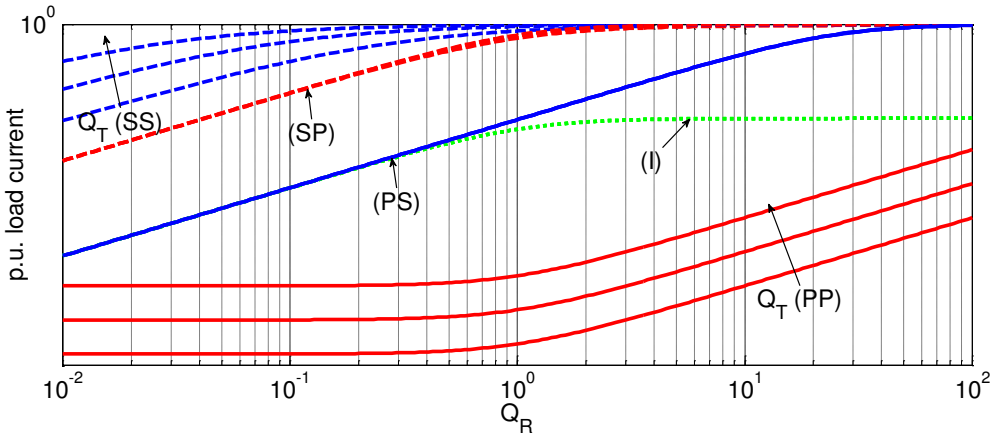

Fig.6.24. PUMLRC of resonant WPTS and of inductive WPTSs vs. Q_R for different Q_T

6.6. Conclusion

This chapter has dealt with the characteristics of resonant WPTSs intended to charge the batteries of the EVs. The figures of merit defined in chapter 3 is taken to evaluate the characteristics of a WPTS, analytical expressions of them have been worked out for the resonant WPTSs with all four topologies, and -as a point of reference- for the inductive WPTSs. Then a thorough evaluation of the characteristics, expressed in terms of quality factors of the receiving and transmitting sections, have been carried out under varying load and coupling coefficient. From the comparison of the characteristics, it has appeared that the resonant WPTSs with the SS topology are the best overall choice because they feature many merits such as higher efficiency, lower power supply sizing factor, higher p.u. magnitude of the load resistance current, and lower sensitivity of the figures of merit to both the quality factor of the receiving section and the coupling coefficient. The only shortcoming is the higher receiving coil sizing factor, that increases with the quality factor of the receiving section.

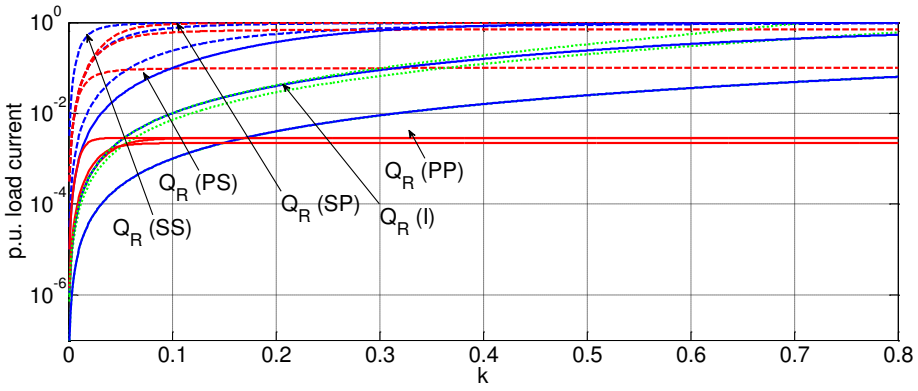

Fig.6.25. PUMLRC of resonant WPTSs and inductive WPTSs vs. k. for different Q_R

6.7. References

[1] S.Chopra, " Power transfer for electric vehicle charging application," TU Delft Institutional Repository, 2011.

[2] C.S.Wang, O.H.Stielau and G.A.Covic, "Design considerations for a electric vehicle battery charger," *IEEE Trans on Industrial Electronics*, vol. 52, pp. 1308-1314, 2005.

[3] M.Bertoluzzo, G.Buja and K.N.Mude, "Characteristic Evaluation of Wireless Battery Chargers for Electric Vehicles," Proceedings of IEEE Electro motion conference, 2013, pp.1-6.

[4] S.Chopra and P.Bauer, "Analysis and design considerations for a power transfer system," Proc. of Telecommunications Energy Conference (INTELEC), 2011, pp. 1–6.

[5] C.S.Wang, G.A.Covic and O.H.Stielau, "Power transfer capability and bifurcation phenomena of loosely coupled inductive power transfer systems," *IEEE Trans on Industrial. Electronics*, vol. 51, no. 1, pp. 148–157, 2004.

[6] K.N.Mude, M.Bertoluzzo, and G.Buja, "Design of battery charger for electrical vehicle," Proceedings of IEEE International Conference of AFRICON, 2013, pp.1091-1096.

Chapter 7

Power Supply for WPTS

Summary

This chapter provides a general overview of the power supply requirements for operating the WPT coils. To start, basic analysis and operation of wide band gap devices such as SiC and GaN and converter/ inverter sections required for WPT system is introduced. Supply requirements such as high frequency converter and requirement of power factor correction (PFC) rectifier are explained. Consideration of effect of losses in power electronic components in various stages of a WPT system are also discussed.

7.1. Introduction

For effective wireless power transfer a high frequency alternating current is necessary. This frequency is in the order of 10 kHz to 100 kHz, which is much higher than the 50 Hz of the electrical grid. The desired frequency is achieved by combining a rectifier with an inverter. In order to keep losses at a minimum soft switching was preferred (today WBG devices), where the transistors of the inverter only switches on or off when the current is zero. The inverter produces a square voltage waveform, but since it is connected to a resonant circuit the current will be sinusoidal [1].

One of the objectives of this chapter is to introduce the power supply requirements for the WPT systems and the topologies that will be considered are based on the full bridge converter in order to achieve the highest power transfer efficiency. The classical hard-switching converter and its versions with resonant transitions were not well adapted to the requirements of the WPT applications.

The rate of change of the magnetic field is equal to the primary current frequency *f*, higher signal frequency enhances the power transfer capabilities of the system. The function of the power converter on the primary is to electronically synthesize the high frequency current at its output by using modern switching elements and converter topologies. Although there have been some attempts to achieve direct *ac-ac* conversion from the grid to the high frequency output, most topologies are based on the well-known two-stage *ac-dc-ac* conversion. Modern WPT systems make use of voltage-fed, full-bridge resonant topologies, taking advantage of modern wide band gap (WBG) switches such as SiCMOSFET and SiCIGBT switches and by applying modular parallel design of the primary converter.

7.2. Wide band gap switches

There are two main categories in the WBG switches, one is Silicon carbide (SiC) and Galinium nitride (GaN) [2].

SiC offers several advantages as a semiconductor material over conventional Si. The SiC materials allow to develop a high capacity, low loss power transistor devices. The power converters that are designed by SiC devices are able to reduce the significant amount of losses as compared to conventional one. The SiC devices have the advantages like high efficiency, high operating frequency and wide range of operating temperature, which permit

to think beyond the range of conventional devices. The SiC transistors are unipolar devices i.e. junction filed effect transistor (JFET), bipolar junction transistor (BJT) and the metal oxide silicon filed effect transistor (MOSFET). In future it may possible to have bipolar devices, but present availability of 1200 V SiC BJTs behave as unipolar devices because in practical there no dynamic effects associated with build up or removal of excess charges. The reason for this is that the doping levels of 1200 V SiC transistors are so high that any considerable carrier injection is superfluous for the conduction mechanism. The market of the SiC devices is still on growing stage and today available SiC switches are the JFET, BJT and MOSFET only. There is no mass production for SiC devices for commercial purposes. Therefore, the cost of these devices more as compared to Si devices. The SiC devices available for the voltage rating in the range of 1200 V and current ratings in the range of few tens of amperes. The driver circuit for these devices must be design in the manner so that devices can be used for high efficient power converters. SiC has the following advantages over Si are

- Wide band gap
- High critical and electric fields
- High velocity saturation and Low permittivity
- Smaller size and weight
- High thermal conductivity
- Bipolar

In the other end second type devices GaN has very high breakdown voltages, high electron mobility and very high saturation velocity as compared to Si. These tremendous advantages made it an ideal candidate for high-power and high-temperature applications. The large band gap means that the performance of GaN transistors is maintained up to higher temperatures than silicon transistors. These devices were designed to replace power MOSFETs in applications where switching speed or power conversion efficiency is critical. These transistors, also called eGaN FETs, are built by growing a thin layer of GaN on top of a standard silicon wafer. This allows the eGaN FETs to maintain costs similar to silicon power MOSFETs, but with the superior electrical performance GaN. When these devices are under operation, the self-heating problem severely limits their performance and lifetime. It is of great importance to prudently assess the device heating problem if a reliable power electronic device is to be developed.

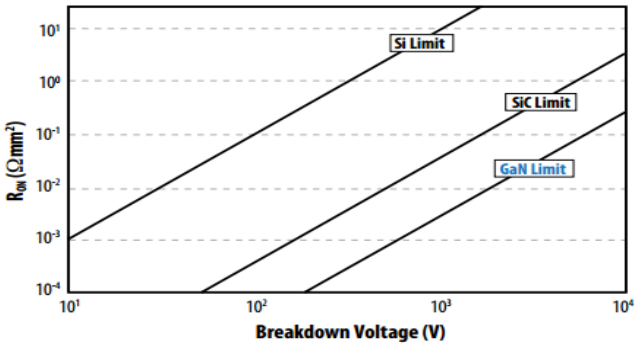

Fig. 7.1 On-resistance vs blocking voltage capability for silicon, silicon-carbide, and gallium nitride

Fig. 7.1 shows the on-resistance versus blocking voltage capability for silicon, silicon carbide and gallium nitride. The on resistance of the power devices play important role for measuring the conduction losses.

The GaN is more advantageous over silicon and silicon carbide to reduce the power loss as compared. Advantages of GaN are as follows

- reduce carrier concentration
- better dynamic response
- low on-resistance
- faster switch, high frequency
- Smaller size and weight
- high power and better heat dissipation.

7.3. Comparative properties of wide band gap semiconductors

Table 7.1. Properties of various WBG semiconductors [4]

Property	Si	6H-SiC	4H-SiC	GaN
Bandgap Eg(eV)	1.1	3.03	3.26	3.45
Dielectric Constant, ε_r	11.9	9.66	10.1	9
Breakdown Field, E_c(kV/cm)	300	2500	2200	2000
Electric mobility, μn (cm^2/V-s)	1500	500	1000	1250
Hole mobility, μn (cm^2/V-s)	600	101	115	850
Thermal Conductivity, λ (W/cm-K)	1.5	4.9	4.9	1.3
Thermal Expansion (x10^{-6})/^{0}K	2.6	3.8	4.2	5.6
Saturated E-Drift velocity, V_{sat} (x10^7cm/s)	1	2	2	2.2

The different parameters of several semiconductor materials are shown in Table 7.1, where clearly shown the wide bandgap semiconductors have lot of advantages over Si. Among all the semiconductors GaN has the widest bandwidth and it also has the highest electric breakdown field. The performance of GaN is very similar to SiC but based on some advantageous characteristics SiC is generally preferred over GaN. Due to the wider bandgap, SiC and GaN semiconductor devices required higher activation energy in results these devices can operate at very high temperature. As we can observe from Table 7.1, SiC and

GaN devices having very high Electric Breakdown Field as compared to Si. Therefore, these devices can generate the carriers through impact mechanism. The on resistance of SiC polytypes and GaN is approximately ten times less than of Si devices that result in lower conduction losses. Therefore, overall converter efficiency of SiC and GaN devices is very high as compared to Si devices. These wider bandgap devices can be operate at very high frequency due to very high saturation drift velocity, which is directly proportional to the switching frequency. The WBG devices have higher thermal conductivity. Therefore, high thermal conductivity of SiC allows more efficient heat transfer from heat sink and yields lower junction temperature.

7.4. Converter/Inverter for WPT

Converters are commonly used to generate a high frequency current on the primary side of a WPT system. Practically, there are two approaches to achieve high frequency current generation: linear amplifiers or switch mode power converters. In the former case, the semiconductor devices are operated in a linear region. Even though the development of different classes of linear electronics amplifiers provides various improvements, the nature of high power loss in linear region limits a linear amplifier to low power applications, where power efficient is not so important. Comparing to linear amplifiers, switch mode power converters can achieve high efficiency by fully on/off control [3]. Therefore switch mode power converters are widely used to generate high frequency track currents for medium or large WPT applications, where the power efficiency is one of the major concerns [4].

Numerous switch mode power converters are currently being deployed to generate high frequency track currents for WPT systems. The input power source for a switch mode high frequency power converter can be either a DC or directly from AC mains [4]. Thus, the switch mode power converter for an WPT system can be commonly classified further into two categories according to the type of their input sources. They are DC-AC inverters and direct AC-AC converters. Practically, because a direct DC source is not ubiquitous for accessing to generate high frequency currents, at present most of the power converters used for WPT systems are two stage AC-DC-AC converters. To obtain a constant DC power source, a front-end AC-DC rectifier is needed. In addition, energy storage elements are necessary to link the rectification circuits and the DC-AC inverter to buffer the difference between the instantaneous input and output power within a two-stage converter. In order to meet the requirements of international standards and improve efficiency, many methods are applied to the AC-DC conversion stage, such as synchronous rectifiers, filters, power factor correction circuits, etc. Once a stable DC power is obtained, a second stage DC-AC inverter is required for the high frequency track current generation.

A PWM hard switching technology is commonly used in the design of power converters. Using such a switching technique, the on and off transients of the switches may take place at non zero voltage or current instants leading to a hard switching operation. In addition, during the on and off switching transients, the semiconductors have to withstand high voltage and current simultaneously resulting in high switching losses and stress. Although passive inductive or capacitive components can be used as snubbers of semiconductor switches to reduce the switching *dv/dt* and *di/dt*. Any variation of the dead time caused by the switching

control will cause an incomplete charging/discharging of the snubber capacitors. As a result, the residue voltage will be shorted, which may cause devices to fail. Soft switching techniques, which combine conventional PWM technology with resonant concepts, offer another switching technique for WPT converters. Such soft switched converters have similar switching waveforms to those of conventional PWM converters except that the rising and falling edges of the waveforms are smoothed without transient spikes. Soft switched converters usually utilize the resonance in a controlled manner [5].

7.5. Full-Bridge Inverter

The inverter considered in this thesis is a full bridge inverter shown in Fig.7.2, based on an existing Phase shift full bridge inverter, where the phase shift is driven to be as close to 100% as possible. This inverter is designed for a higher voltage and power level but approximately the same load current [6]

.

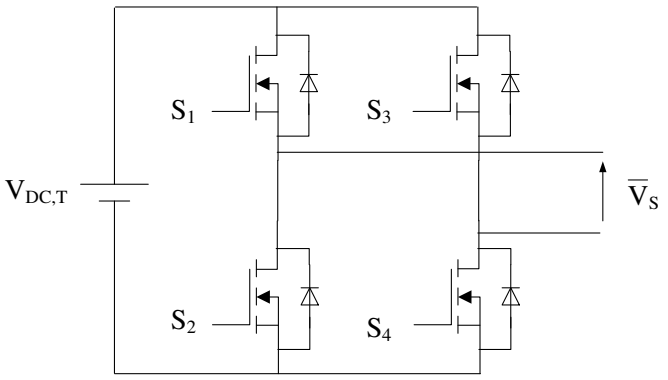

Fig. 7.2 Full bridge inverter

The term phase shifted full bridge relates to a control scheme where both legs are separately driven to a duty ratio very close to 50% and then phase shifted against each other than the 180 degrees shift between the two legs' waveforms there is also a delay between the turn off of one transistor and the turn on of the other one in the same leg. Primarily this ensure that the full bridge doesn't suffer from current shoot through, which it otherwise would have issues with at time periods where both the upper and the lower transistor in the same leg are open, i.e. the supply is short circuited. The main point about phase shifted control in comparison with using conventional pulse width modulation (PWM) waveforms is the possibility to not only control the duty cycle but also add some degree of control of the switching losses. In the proposed full bridge, it is not possible to reach quite 100% phase shift, but one can get very close, around 99%. The basic switching waveforms are shown in Fig 7.3. The switching schedule illustrated in Fig 7.4 is broken down into time intervals and explained below.

t1-t2

At this point, the load current flows in the positive reference direction through S_1 and S_4, as shown in Fig 7.4 (a). Power is being delivered to the load and the overall full bridge is in an on-state.

t2-t3

At t_2, S_4 is turned off case of Fig. 7.4 (b). During the turn-off of S_4, its current commutates to the body diode of S_3. This interval is the part of the dead-time controlled by the phase shifted gate pulse control and often referred to as the freewheeling interval

t3-t4

At t_3 S_1 is turned off and the decreasing current through it, if any, commutates to the body diode of S_2, Fig 7.4 (c). The description of this stage depends on the load condition and the inductance of the converter circuit. If the full load current reaches zero of period t_2-t_3, the current will simply be zero until t_4. If not, the time between t_3 and t_4 is set by the time it takes for the current to reach zero at full, reversed supply voltage.

t_4-t_5

At t_4 the case of Fig 7.4 (d) starts as the current has reversed and is actively driven in the negative reference direction through S_2 and S_3, which are turned on Similar to period t_1-t_2 this goes on until t_5 where S_3 is turned off.

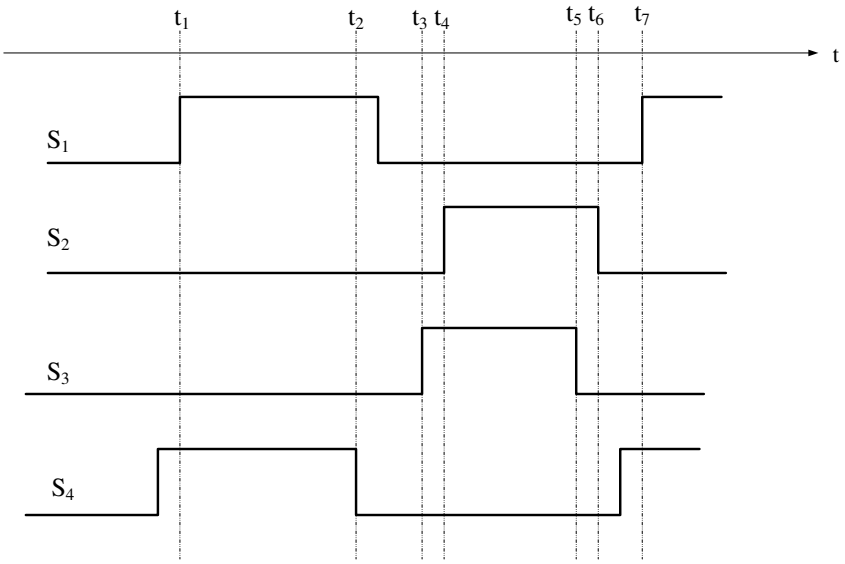

Fig. 7.3 switching pattern of Full bridge inverter silicon-carbide, and gallium nitride

t_5-t_6

As in the other half period, the current previously in the right leg of switch commutates to the body diode of the opposite transistor in the same leg, in this case the current through S_3 commutates to the body diode of S_4, as shown in Fig 7.4 (e). After another delay t_6 is reached.

t_6-t_7

At t_6 S_2 is turned off, while S_2 is turned on and the current through S_2 commutates to the body diode of S_1. This stage ends at t_7, where the case of Fig 7.4 (f) has begun. The current reversal is completed and S_1 and S_4 is turned on as the switching scheme is repeated from t_1.

7.6. Losses

Loss analysis is very important for any power electronics system. Due to the increasing use of power electronics in a wide range of applications, power loss measurement with high accuracy is of great importance in the design process to assess system performance and optimize design characteristics. To measure the total loss of the system it is necessary to have the idea of losses of individual devices of the system.

Losses in the converter have two types, namely the conduction losses and switching losses. When switching the inverter at the resonance frequency, resonant switching takes place i.e., ZCS and ZVS can be accomplished thereby reducing the switching losses during the switching on and/or switching off. This also makes it possible to operate the converter at high switching frequencies when compared to hard switching PWM converters.

The other losses associated with the converter are the conduction losses which are dependent on the type of switches used. In case of SiCMOSFETs, the conductions losses are dependent on the current flowing through the switch and the on state drain to source resistance.

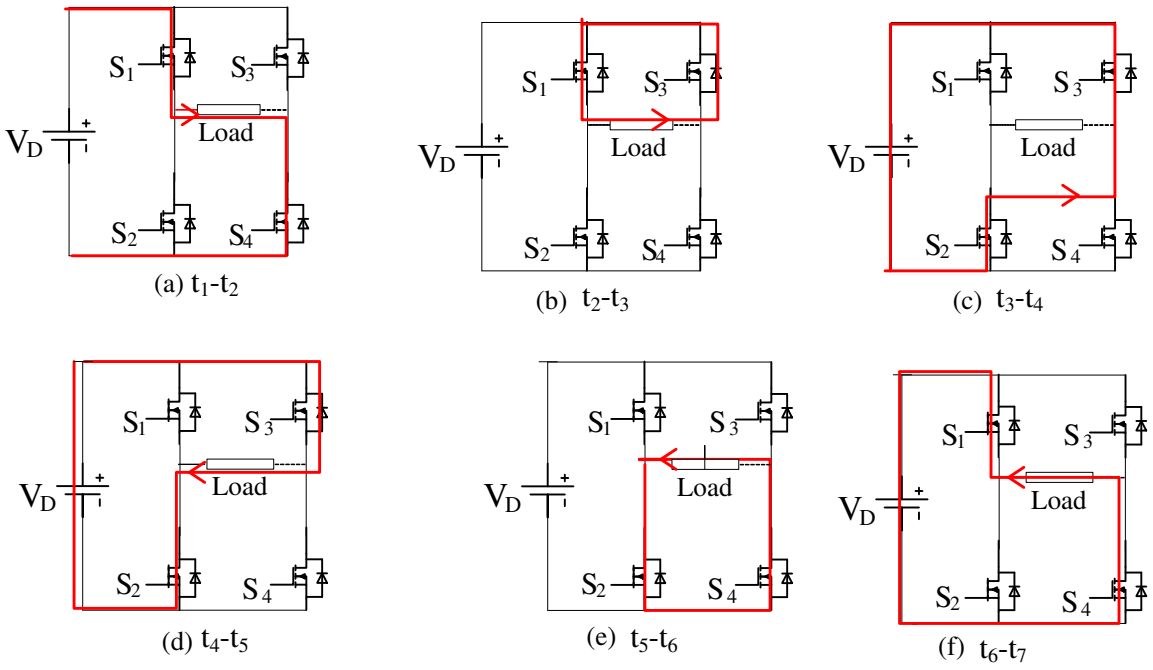

Fig. 7.4 Switching schedule of phase shift full bridge inverter

7.6.1. Power loss calculation in diode

The total power loss in diode is the sum of the total conduction loss and switching loss.

Total conduction loss,

$$P_{cond} = P_{on} + P_{off} = V_f I_{on} + V_{off} I_{rev} \approx 0 \quad (7.1)$$

Total switching loss,

$$P_{sw} = \frac{V_{AK} f_s (t_r + t_{rr}) I_{on}}{2} \qquad (7.2)$$

Total power loss given by

$$\mathrm{P} = \mathrm{P_{cond}} + P_{sw} = V_f I_{on} + V_{off} I_{rev} + \frac{V_{AK} f_s (t_r + t_{rr}) I_{on}}{2} \approx \frac{V_{AK} f_s (t_r + t_{rr}) I_{on}}{2} \qquad (7.3)$$

7.6.2. Power loss calculation in SiCMOSFET

Hence, the total power loss in SiCMOSFET is the sum of total conduction loss (P_{cond}) and total switching loss (P_{SW}). So total losses calculated as follows

Total conduction loss,

$$P_{cond} = P_{on} + P_{off} = R_{ds\,(on)} I^2{}_{on} + V_{DS} I_{DS} \quad (7.4)$$

Total switching loss,

$$P_{sw} = \frac{V_{DS} f_s (t_{on} + t_{off}) I_{on}}{2} \qquad (7.5)$$

Total power loss,

$$\mathrm{P} = \mathrm{P_{cond}} + \mathrm{P_{sw}} = \mathrm{R_{ds\,(on)}} \mathrm{I^2_{on}} + \mathrm{V_{DS}} \mathrm{I_{DS}} + \frac{\mathrm{V_{DS}} \mathrm{f_s} (\mathrm{t_{on}} + \mathrm{t_{off}}) \mathrm{I_{on}}}{2} \quad (7.6)$$

7.7. Power factor correction (PFC) Rectifier

The grid supply supposed to be cleaned and free from high voltage spikes and current harmonics, in order to ensure good quality. Discontinuous input current that exists on the grid caused by the non-linearity of the rectification process which further cause reduction of power factor. In order to increase power factor of the system, a Boost chopper added to Diode rectifier to minimize the reactive power demand from the utility grid and maximizes the current waveform quality by reducing the distortions. SiC diodes can be employed for high frequency operation as they have a very low reverse recovery current but then their forward bias voltage drop is quite significant and thereby increases the conduction losses.

Among the three basic choppers buck, boost, buck-boost the boost chopper is the most suitable for use in implementing PFC. Because the boost inductor is in series with the line input terminal, the inductor will achieve smaller current ripple and it is easier to implement average current mode control. Buck chopper has discontinuous input current and would lose control when input voltage is lower than the output voltage. The buck-boost chopper can achieve average input line current, but it has higher voltage and current stress, so it is usually used for low-power application.

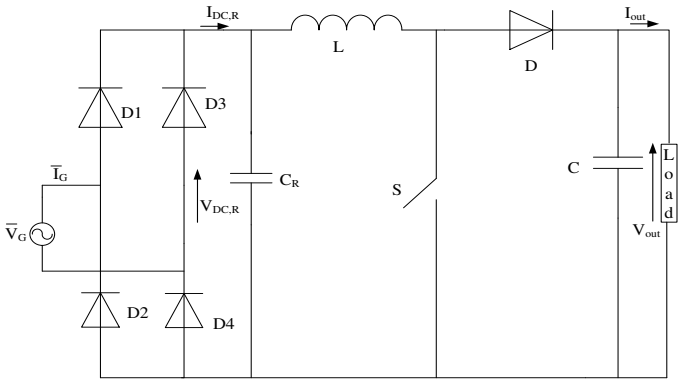

Fig. 7.5 PFC-Boost Rectifier

Fig. 7.5 shows the schematic diagram of PFC boost chopper added to diode rectifier. The design values of PFC boost chopper is as follows. The input design data is considered from Tab.7.2.

Table. 7.2

Grid input voltage V_G	230 V_{rms}
Minimum value of Grid input voltage $V_{G,min}$	207 V_{rms}
Maximum value of Grid input voltage $V_{G,max}$	253 V_{rms}
output voltage V_{out}	370 V
Minimum output voltage $V_{out,min}$	350 V
Maximum output voltage $V_{out,max}$	390 V
Grid frequency f_G	50 Hz
Minimum Grid frequency $f_{G,min}$	47 Hz
Switching frequency f_{sw}	85 kHz
Considered power factor	0.99
Efficiency at full load	0.92
I_{ripple}	10%
V_{ripple}	6%
Maximum output power $P_{out,max}$	700 W

To find out the inductor and capacitor values of the boost chopper, preliminary values of currents and voltages is necessary and it can be found as below

Maximum value of the output current can be calculated as (7.7)

$$I_{out,max} = \frac{P_{out,max}}{V_{out}} \qquad (7.7)$$

and its value comes out to be 1.89 A_{rms}. The grid current can be calculated as

$$I_G = \frac{P_{out,max}}{\eta V_{in} PF} \quad (7.8)$$

By substituting its values in (7.8), it comes out to be 3.71 $_{Arms.}$ Peak value of grid current as (7.9)

$$I_{G,pk} = \sqrt{2}\, I_G = 5.25 \text{ A} \quad (7.9)$$

and average value of grid current is given as

$$I_{G,avg} = \frac{2.I_{G,pk}}{\pi} = 3.34 \text{ A} \quad (7.10)$$

By considering 10 % current ripple of peak grid current, the ripple current will be 0.525 And minimum value of rectified DC voltage

$$V_{DC,R,min} = \sqrt{2}\ V_{G,min} = 294.7 \text{ V} \quad (7.11)$$

Maximum ripple value of grid voltage is 6% of rectified minimum dc voltage and its comes out to be 17.56 V. Input filter capacitance can be obtained as

$$C_R = \frac{I_{Ripple}}{8\, f_{sw} V_{G,ripple,max}} = 44 \text{ mF} \quad (7.12)$$

And the duty cycle obtained as

$$D = \frac{V_{out} - V_{DC,R,min}}{V_{out}} = 0.209 \quad (7.13)$$

The inductor value obtained as

$$L > \frac{V_{out} \cdot D\,(1-D)}{I_{ripple} \cdot f_{sw}} = 1.37 \text{ mH} \quad (7.14)$$

By considering Turn-on time (t_{on}), of 20 ms, The value of the capacitor calculated as

$$C > \frac{2\, t_{on} P_{out}}{V_{out}^{\,2} - V_{out,on}^{\,2}} = 0.597 \text{ mF} = 0.6 \text{ mF} \quad (7.15)$$

7.8. Chopper

A chopper is a static power electronic device that converts fixed dc input voltage to a variable dc output voltage. As chopper involves one stage conversion, these are more efficient, during the period T_{on}, chopper is on and load voltage is equal to source voltage Vs. During the period T_{off}, chopper is off, load voltage is zero.

7.9. Conclusion

This chapter has dealt with the power supply requirement of the WPTS system. At first started with the basic introduction of WBG switches, showing how they are efficient compared with conventional devices. PFC rectifier, H-bridge inverter and with phase shift

control technique has been addressed. At the last the issues pertaining to circuitry required for the receiving side of WPT, rectifier and chopper are addressed.

7.10. References

[1] K.N.Mude, M.Bertoluzzo and G.Buja "Design of contactless battery charger for electric vehicle", Proc. of IEEE AFRICON, 2013, pp.1099-1104.

[2] J.Millan, P.Godignon, X.Perpina, A.P.Tomas, and J.Rebollo, "A survey of wide bandgap power semiconductor devices", *IEEE Trans. on Power Electronics*, Vol. 29, no. 5, pp. 2155-2163, 2014.

[3] H.Abe, H.Sakamoto and K.Harada, "A noncontact charger using a resonant converter with parallel capacitor of the secondary coil," Proc. of Applied Power Electronics Conference and Exposition Fukuoka, Japan, 1998, pp. 136-141.

[4] J.M.Barnard, J.A.Ferreira and J.D.VanWyk, "Linear contactless power transmission systems for harsh environments," Proc. of *IEEE AFRICON*, 1996, pp.711-714.

[5] A.P.Hu, G.A.Covic and J.T.Boys, "Direct ZVS start-up of a current-fed resonant inverter," *IEEE Transactions on Power Electronics*, vol. 21, pp. 809-812, 2006.

Chapter 8

Implementation of WPTS

Summary

This chapter deals with the implementation of coil coupling system and power electronics circuit for WPTS discussed in earlier chapters. At first the procedure and measurement of spiral coil coupling with the measurement of inductive parameters and magnetic flux density is discussed. Then Power electronics arrangement together with coil system are presented. At the last both systems are integrated and series of measurements were performed under different load conditions.

8.1. Implementation of coil coupling system

From the results of the FEM analysis, spiral coils with outer diameter of 0.38 m and formed by 15 turns spaced of 7 mm is selected for the coil-coupling setup of the study case. For simplicity, current specification is fixed equal to 10A (rms) for the two coils.

8.1.1. Coupling coil

The coils are made up of copper Litz wire to reduce the skin and proximity effects; the wire has a circular cross section with a diameter of 5.2 mm so that the internal diameter of the coil is 184 mm. Each coil lays on the core and the core-coil structure is covered on the two sides by plates for protection purposes. The cores are made up of 16 square planar elements with dimensions 100mm × 100mm × 6mm, placed side by side to form a square with a side of 0.4 m. The core elements are manufactured by Ferroxcube co with part number BLK/100/100/6-3C95. Fig. 8.1 gives the picture of one coil without the upper plate and with the I-core covered by a pink thin layer

Fig. 8.1. Spiral coil-coupling setup with I core.

8.1.2. Inductive parameters measurements

The inductive parameters of the coil-coupling setup have been measured by an LCR meter of InSTEK Co., model LCR-819. For the measurement, the instrument applies sinusoidal voltage of amplitude 1 Vrms and frequency within a predefined set to the coil. Since the selection of 85kHz frequency is not available in the instrument, the inductive parameters of the coils have been measured at the frequencies of 66 kHz and 100 kHz, obtaining almost equal values. At first the two coils, set at a distance of 0.15m, are excited separately and their self-inductances are measured in 118μH and 119 μH. The mutual inductance is determined by measuring the self-inductance L_{ser} at the terminals of the series connection of the two coils. Then, from the expression

$$L_{ser} = L_T + L_R + 2M \qquad (8.1)$$

M is derived as

$$M = \frac{[L_{ser} - (L_T + L_R)]}{2} \qquad (8.2)$$

and comes out to be equal to 29 μH. Parametric sweeps of the coil distance and coil misalignment are carried out to measure the change of the inductive parameters. The measured values are tabulated in Tab. 8.1. and Tab. 8.2, respectively

Table 8.1. Coil-coupling setup measurements		
Coil distance [m]		
0.1	0.15	0.2
L_T=122 μH L_R=125 μH M=47 μH k=0.382	L_T=118 μH L_R=120 μH M=29 μH k=0.245	L_T=112 μH L_R=117 μH M=14 μH k=0.116

Table 8.2. Coil-coupling setup measurements		
Misalignment [m]		
0	0.1	0.2
L_T=118 μH L_R=120 μH M=29 μH k=0.245	L_T=117 μH L_R=120 μH M=20 μH k=0.168	L_T=119 μH L_R=116 μH M=5.87 μH k=0.05

The measurements agree very well with the results of the analysis as it can be verified from Figs. 5.4, 5.5 and 5.8. The minor mismatch between the self-inductance of the two coils can be ascribed to construction tolerances whilst the small deviations of the self-inductances and mutual inductance from the expected values are due to usage of a squared core instead of a circular one as it has been proved with a successive FEM analysis.

8.1.3. Electromagnetic field measurements

The measurements of the electromagnetic fields with regard the human exposure have been done according to the procedure described in the standard IEC 62233. The coils have been supplied and loaded with a prototypal power circuitry and the fields have been measured using the wide-band probe EHP200 produced by Narda Co. Tab. 8.3 reports the measured intensity of the magnetic flux density in the 9 points of the testing plane shown in Fig. 5.9. Tab 8.4 reports the measured intensity of the electric field in the three central points, where it takes the highest values. The data show that the maximum magnetic flux density is of about 8.8μT and the maximum electric field is of about 128 V/m. Both these value are within the prescribed limits.

Table 8.3. Magnetic flux density

Measurement Point	B [μT]
1	3.7
2	4.0
3	3.6
4	6.7
5	8.8
6	6.5
7	3.6
8	3.9
9	3.3

Table 8.4. Electric field

Measurement Point	E [V/m]
4	110.8
5	127.8
6	109.9

8.2. Power electronics system implementation of WPT

8.2.1. Resonance capacitors

The resonance capacitors were made by connecting by the series-parallel combination of EPCOS B32652A1153. Each of them has a capacity of 15 nF and supports a voltage of about 300 V to a working frequency of 85 kHz. Therefore, the required value of capacity was obtained by connecting in parallel eight strings of capacitors each formed by 4 capacitors in series. Therefore, the maximum voltage was 1200 V.

8.2.2. High frequency inverter

The high frequency inverter is built as per Fig. 7.3. The H-bridge has been designed using two legs of the three-phase power module CCS050M12CM2, manufactured by CREE and shown in Fig.8.2. The characteristics are tabulated in Tab. 8.4.

Fig. 8.2. H-bridge inverter module CREE CCS050M12CM2 [1]

Table 8.4. Specifications of the CCS050M12CM2	
Voltage	1200 V
Current	50 A
Conduction resistance	25 m Ω

8.2.3. Diode Rectifier and chopper

The diode rectifier for transmitter and receiver and the chopper for receiver have been designed with the usual procedures. For the diode rectifier in the transmitter the single-phase bridge rectifier KBPC606 has been used. The output capacitor of the rectifier has a capacity of 4.7mF and a capacitor voltage of 400V. For the diode rectifier for receiver, SiC Schottky diodes have been used (SCS240AE2HR), while for the chopper SiC MOSFET (SCT2120AF) and a freewheeling diode SiC Schottky (SCS220AE2) have been used. The output capacitor of the rectifier has a capacity of 220mF and a rated voltage of 160 V. The characteristics of devices is tabulated in Tab.8.5.

Table 8.5. Devices and their data			
Device	Voltage	Current	Producer
KBPC606	600 V	6 A_{AV}	Vishay

SCT2120AF	650 V	29 A_{DC}	Rohm
SCS220AE2	650 V	20 A_{DC}	Rohm
SCS240AE2HR	650 V	40 A_{DC}	Rohm

8.2.4. Interface of power cards

The WPT charger consists of two converters, one is high frequency inverter to transmitter and other one is chopper in the receiver. The control is performed by two electronics control unit (ECU) arranged in two stages and built around the DSP TMS320F282335. They generate the control signals for the two converters (and handle the operations of the battery charger, including protection) as a function of the values assumed by the voltages $V_{DC,T}$ and $V_{DC,R}$ and of the currents I_T, I_R and I_B. shown in Fig. 1.1.

The generated commands from the DSP were applied to the gates of the transistors of the inverter. For the implementation of appropriate circuitry, the acquisition of the voltages and currents by the DSP is required. The similar operations should carried out in transmitter and receiver so single interface card is enough can realized for two stages of charger. The power boards for the two stages required a design and an ad-hoc realization since they use different types of converters.

8.2.5. Current sensing

To measure the current in the transmitter and receiver (I_T, and I_R) Hall effect sensors model LTSP 25-NP produced by the firm LEM is used and shown in Fig. 8.3. It has a full scale of 25 A rms and a bandwidth of 300 kHz. The Hall effect sensors generate an output (on a resistor of known value) a current proportional to that to be measured and the voltage across the resistor is thus proportional to the current to be transferred.

Fig. 8.3. Current sensor LTSP 25-NP

8.2.6. Control algorithm and management

Two different algorithms of control and management for the transmitter and receiver were developed. Both manages the user interface and the serial communication mode with virtually identical but differ in the control of the power boards. When the system initializes all peripherals of the DSP involved in the operation of the charger, in particular, set the mode of generation of the control signals of the transistors, the ADC is initialized, are set to the communication mode of the RS232 and SPI; through this port I/O is also initialized. Only after completing all the initialization operations, it is possible, using a button on the user

interface, enable the control algorithm which controls the transistors of the high frequency inverter and the chopper.

In the transmitter, the control algorithm processes the value of the DC voltage $V_{DC,R}$ that feeds the chopper in the receiver and generates the commands to the transistors of the high frequency inverter so as to adjust the voltage $V_{DC,R}$ of 65 V. In a first stage of development of the control algorithm, using the fact that the current supplied to the battery charger acts as a disturbance on $V_{DC,R}$ and varies slowly during the charging process. It is speculated to operate in conditions of quasi steady-state. Consequently, the control loop of the voltage $V_{DC,R}$ is designed so as to have a very slow dynamic, which has allowed to omit the implementation of the control of the current in the transmitter and receiver. Moreover, the interface card already includes circuits transduction and acquisition of the currents and therefore, in addition to the operations of protection, the ECU also performs current control. The output of the voltage regulator is the amplitude of the fundamental component of the voltage generated by the high frequency inverter. From this reference and a function of the DC voltage $V_{DC,T}$ which feeds the inverter, the DSP calculates the timing of the phase cancellation for the control of the transistors of the high frequency inverter . The control algorithm of the receiver side has the purpose of loading the accumulator pack with the usual procedures such as first constant current and then at constant voltage. The algorithm is formed by two control loops nested in one another. The outer control loop employs a controller that processes the error voltage, given by the difference between the maximum charging voltage $V_{B,M}$ and the current voltage to the terminals of the package accumulators, to generate the current reference for the charge. This reference, limited to the value of specific I_B, constitutes the input of the control loop that generates internal controls for the transistor of the chopper. In the first phase of the charging process, the external controller enters saturation and the charge is carried out with a constant current equal to I_B. When the error voltage becomes small, i.e, when the voltage accumulators is approximately equal to $V_{B,M}$ then one can enter the second phase of the charging process during which the terminal voltage of the accumulator pack is maintained constant. In correspondence of the reference current is reduced until it reaches the minimum value of current $I_{B,m}$, the charging process terminates.

8.2.7. Interface

The interface card is arranged for the connection with the development board of the DSP (Texas F282335) is shown in Fig. 8.4. The power boards are designed for the mounting of the driving modules of the SiC MOSFET transistors. The modules shown in Fig. 8.5, are produced by the company CREE. They amplify the current and voltage control signals generated by the DSP and these signals further applied to the gates of the transistors.

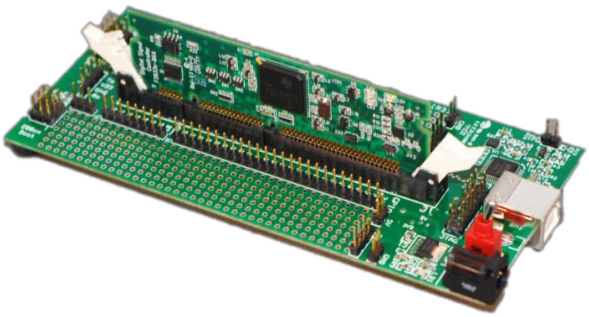

Fig. 8.4. DSP development board of the Texas F282335

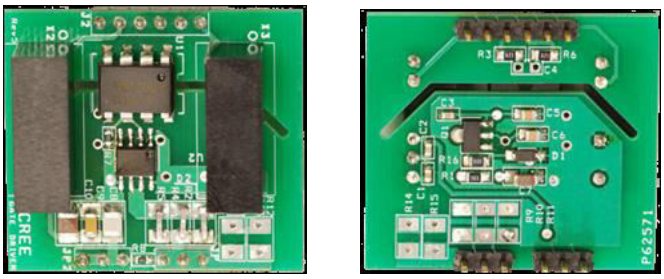

Fig. 8.5. Driving module of the SiC MOSFET.

8.2.8. Programing in DSP

The implementation of the management and control algorithms performed by Code Composer Studio (CCS) v5, provided by Texas Instruments. In such an environment it is possible to write the code for the DSP in the C language and perform the steps of compilation and linking. The code debugging can be done with the simulator software that is part of CCS. The execution time is programmed to be performed asynchronously with respect to the algorithm of control and period of acquisition of inputs and outputs are about 1 ms. The control algorithms are implemented in the interrupt service routine at the end of the ADC conversion and begin to develop new standards of voltages and currents. The start of the conversion is dictated by a timer that operates at a frequency 21-25 kHz. It coincides with the frequency of execution of the control algorithm and is equal to a quarter of the operating frequency of high frequency inverter. The refresh rate of data exchanged via serial may not be as high as that of the timer due to the limited transmission speed of the serial port and was set at about 5.3 kHz, a value that considerate the dynamics of the process of loading is adequate with an update request.

8.3. Assembling the prototype example of the turning tests

The realization of printed circuit boards has been entrusted to an outside firm and the assembly of all electronic components has been carried out in the laboratory.

Fig. 8.6, shows the power board of the transmitter mounted on the heat sink and equipped with the driving modules of the four transistors SiC MOSFET. Vertical connectors for connection to the interface card are visible in fore side while on the far side of the card are mounted capacitors blue color output of the diode rectifier. Under the capacitors, on the opposite side of the printed circuit and in direct contact with the heat sink is mounted on the power module. Behind the capacitors can be glimpsed two sensors of the current I_T (in fact one of them has been installed for future developments).

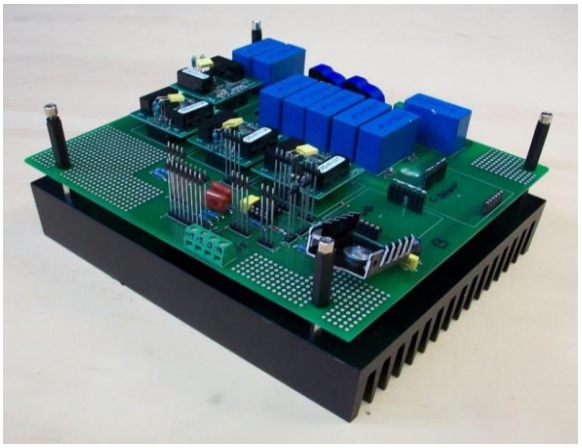

Fig. 8.6. Transmitter power board

Fig. 8.7 shows the power board of the receiver. In the foreground, on the right side, DC/DC converters of small power which adapt the DC voltage $V_{DC,R}$ to the value required to power the circuitry of the signal of the power board and, through the vertical connectors, the card interface are visible. The SiC Schottky diodes and SiC MOSFETs which constitute respectively the rectifier and the chopper are mounted under the printed circuit in contact with the heatsink. The voltage $V_{DC,R}$ is supported by the three capacitors in black while the black cylinder in front of them is the inductor filter placed at the output of the chopper. Behind the capacitors and inductor filter placed on the top of the two current sensors that transduce I_L and I_B .

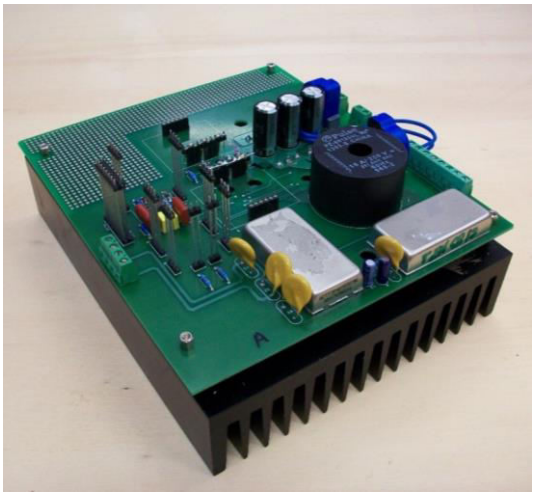

Fig. 8.7. Receiver power board

The interface card is shown in Fig. 8.8. It is known as analog circuits are arranged as far as possible from the power module or from the chopper in order to reduce the effects of electromagnetic noise produced by the switching of SiC MOSFET. On the far side of the board are willing LEDs and terminals that give access to the terminals of the relay user interface. The four buttons of the user interface and the sockets for the cable and serial communication for the CAN bus are located on the left side of the card.

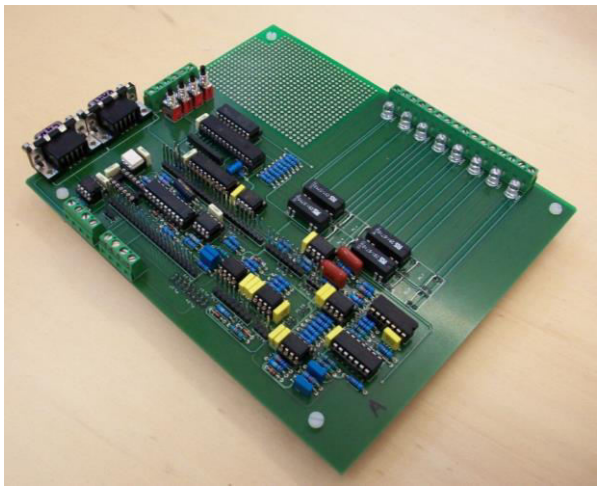

Fig. 8.8. Interface card.

The development board DSP is finally installed on the interface card, the layout shown in Fig. 8.9. As one can see, even the details of the DSP is installed as far away as possible from the SiC MOSFET to mitigate the effects of electromagnetic interference.

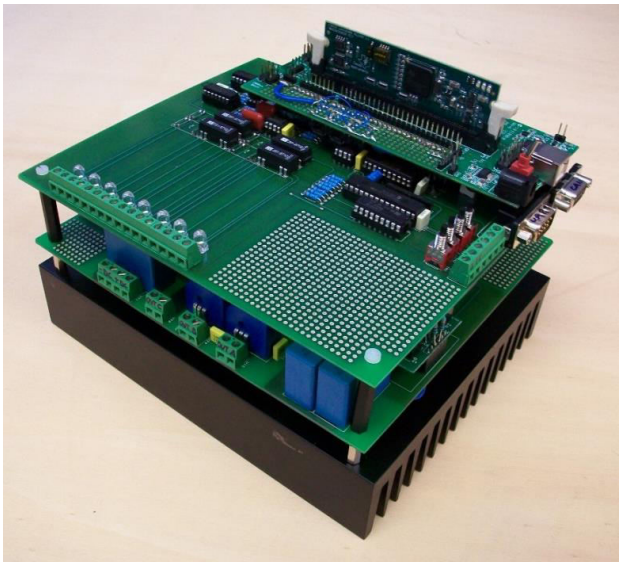

Fig. 8.9. Complete transmitter system

Experimental prototype setup was built in laboratory. In this first phase the power of the transmitter has been provided by means of a variac in order to expose the device to stress gradually. The interface cards are been fed by a stabilized power supply. As load was employed a rheostat which allowed to simulate different operating points along the charging characteristic of a battery. The layout of the prototypal test bench is shown in Fig.8.10.

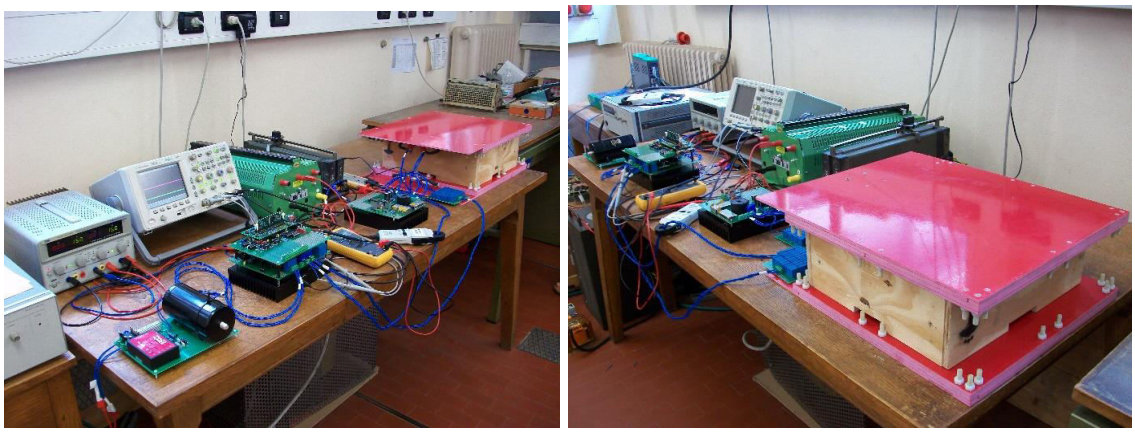

Fig. 8.10. Layout of test bench.

Experimental results obtained by bringing the charger to operate in proximity of the maximum values of power for which has been sized. The Fig. 8.11 shows the waveforms of the voltage applied to the transmitter coil and the current that runs through it. The voltage varies between about -80V and + 80V while the current amplitude is approximately 6 A. It is known as the current is almost in phase with the voltage and in agreement with the theory behind the design of the resonant coils. The corresponding waveforms of current and voltage are shown in Fig. 8.12. It is practically in quadrature with the supply voltage of the primary coil and its amplitude is about 13A, as expected during the dimensioning phase of the charger.

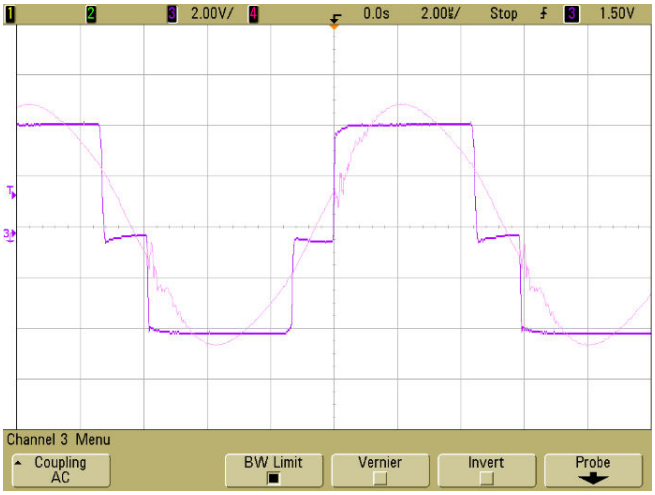

Fig. 8.11. Voltage and current of the transmitter coil

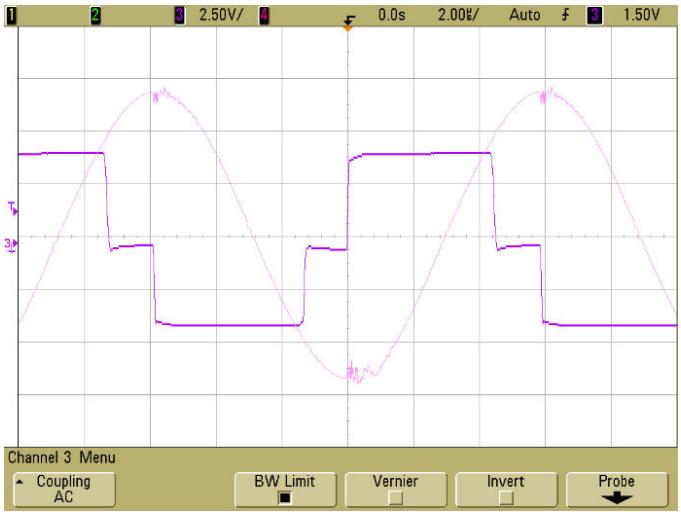

Fig. 8.12. Voltage and current of the receiver coil

8.4. Conclusion

This chapter presented the Prototypal arrangement of WPTS. At first step, coil setup is arranged and series of experimentation performed to measure inductive parameters and magnetic field measurement and after that power circuit added to complete setup. The analytical and simulations studies developed in the previous chapters was verified on the prototype for both aligned and misaligned cases to check their performances. The complete setup is operated with different load conditions and series of experiments are performed to verify the simulation analysis.

8.5. References

[1] www.**cree**.com/~/media/Files/**Cree**/Power/.../**CCS050M12CM2**.pdf (Data sheet).

[2] Current sensor LTSP 25-NP

Chapter 9

On-Line Electrical Vehicle (OLEV)

Summary

One of the biggest issues around the world in recent years are the environmental problems. Every country tries to adopt green technologies which offer the potential to improve the air quality in currently polluted environment and which will save money by reducing fossil fuel consumption. The use of electric cars is expected to significantly reduce the aforementioned problems of air pollution and fossil fuel consumption costs. Numerous studies on electric vehicles have been performed over a long period of time and some electric vehicles are currently sold by several vehicle manufacturers worldwide.

The On-line Electric Vehicle (OLEV) developed by Korean advanced institute of science and technology (KAIST) is an electric transport system, in which the vehicles absorb their power from power lines underneath the surface of the road. Even though the basic concept was invented in 1970's [1], the circuit system and power transfer system are completely different. Rather than relying on battery technology, OLEV picks up a charge using a wireless charging method in which a power source is placed underneath the road surface and power is wirelessly picked up by the vehicle itself. The aim of this chapter to present basic overview of OLEV.

9.1. OLEV System

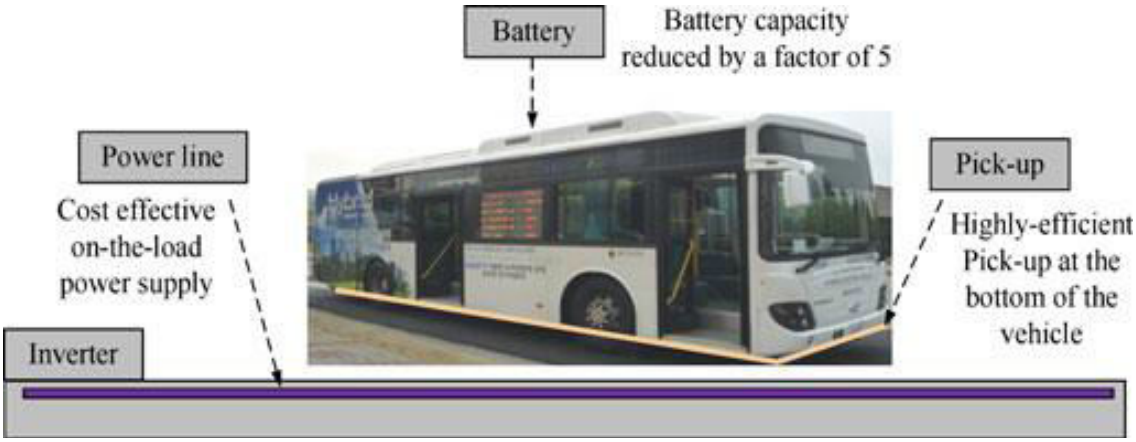

Fig 9.1 Concept of online electrical vehicle [1]

KAIST has introduced a novel OLEV, in which the vehicle constantly recharges via power lines beneath the surface of the road. The OLEV has a minimal battery capacity (about 20 % compared to that of conventional battery-powered electric vehicles), which minimizes the weight and price of both the vehicle and the power station. The OLEV power transfer system consists of an inverter, power lines, pick-up modules, rectifiers, regulators, batteries, and motors, as shown in Fig. 9.1. The inverter converts 60Hz power from electric grid to 20 kHz, 260A current. The inverter is designed to provide consistent current. The power lines carry the current and generate magnetic flux which links with pick-up modules.

The pick-up modules which are at 25cm higher than power lines capture the magnetic flux from the power lines and generate AC power. The rectifiers convert AC power to DC power and the regulators control output voltage which is input voltage of the batteries and the motors. Some of the generated power is used to operate the motors, and the remaining is used to recharge the batteries. When OLEV bus is stops and the motors do not need any power, all of the power is consumed to recharge the batteries.

The design of the power lines and pick-up module determines the performance of the power transfer system and leakage in the electromagnetic field [1]. One of the key design requirements is suppression of the leakage of magnetic flux from power lines and the pick-up module in order to maintain high efficiency of the system and meet the OLEV's total power needs. This chapter introduces the wireless power transfer technology applied to OLEVs, and show the techniques for improving electrical performance. Optimization methodology of the coils design and the shielding of the electromagnetic field are analyzed. The design of the power lines and pick-up module determines the performance of the power transfer system. The magnetic flux generated from the power lines is gathered at the pick-up module to generate DC power for the vehicle's motor. The non-contact power transfer that occurs between the power lines and the pick-up module generates a huge magnetic flux. Therefore, the proper design of the power lines and the pick-up module are the key technologies for effective power transfer and solving the electromagnetic field (EMF) problems.

OLEV system consist of two types of power transfer –mono type power transfer and dual type power transfer with opposite current directions beneath the road surface forming a current loop. Due to the current in the power lines, a magnetic flux is induced around each power line.

9.2. Dual type and mono type power transfer systems

9.2.1 Dual type power transfer systems

In dual type power transfer system, there are two power lines with opposite current directions and an array of ferrite core blocks underneath the road surface, as shown in Fig. 9.2(a). There are two magnetic flux loops in a dual type power transfer system. The magnetic flux from the two power lines are added between them. The ferrite core blocks of shape E around power lines and of pick-up modules increase intensity of the magnetic flux and shape the magnetic flux loop. Voltage and current are induced by the magnetic flux through copper coils of pick-up modules. Dual type power transfer system has larger output power of copper and ferrite core due to better coupling coefficient [2].

9.2.2 Mono type power transfer systems

In mono type power transfer system, there are two power lines and an array of ferrite core blocks underneath the road surface. One power line is on the ferrite core blocks and the other power line is under the ferrite core blocks, as shown in Fig.9.2(b). There is one magnetic flux loop in mono type power transfer system. The shapes of ferrite core blocks are C around power lines and of pick-up modules perform the same role as dual type system. The power line on the ferrite core generates magnetic flux and transfers power to pick-up module.

However, the other power line under the ferrite core is not helpful in transferring power and just returns the current to the inverter. In the same way as dual type system, voltage and current are induced by the magnetic flux through copper coils of pick-up modules [2].

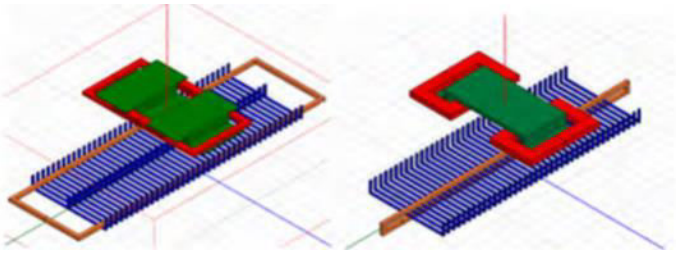

Fig 9.2 (a) Dual Type and (b) Monotype power transfer systems [2]

9.3. Winding Types

The magnetic flux generated from the power lines is gathered at the pickup module to generate DC power for the motor of the vehicle. Generally, two types of power line/pickup module pairs are designed for wireless power transfer according to the direction of the magnetic flux at the pickup module: vertical magnetic flux type and horizontal magnetic flux type [3].

9.3.1 Vertical magnetic flux type

Fig.9.3 shows the vertical magnetic flux type of power lines and pickup module. There are two power lines with opposite current directions underneath the road surface forming a current loop. Due to the current in the power lines, magnetic flux is induced around each power line. Between the power lines, the magnetic fluxes from the two power lines are added. The pickup module catches the vertical magnetic flux through copper coils around the ferrite core. This type has the advantage of efficient power transfer because the direction of the magnetic flux from the power lines is the same as the direction of the flux to the pickup module.

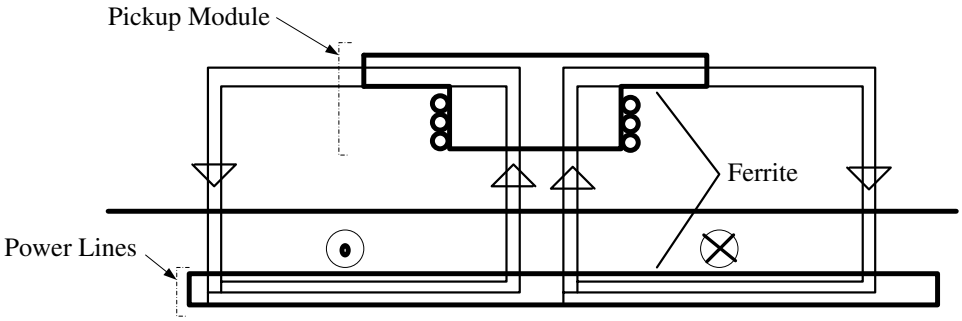

Fig. 9.3 Vertical magnetic flux type

9.3.2 Horizontal magnetic flux type

Fig.9.4 shows the horizontal flux type of power lines and pickup module. In this type, there are four power lines forming two current loops. As two center conductors are placed close together, there are three magnetic flux loops. The copper coils around the horizontal ferrite core catches the horizontal magnetic flux to generate power for vehicles. This type has a disadvantage that the power transfer is less efficient. However, because there are more power lines that have opposite current directions, the magnetic flux density levels cancel each other.

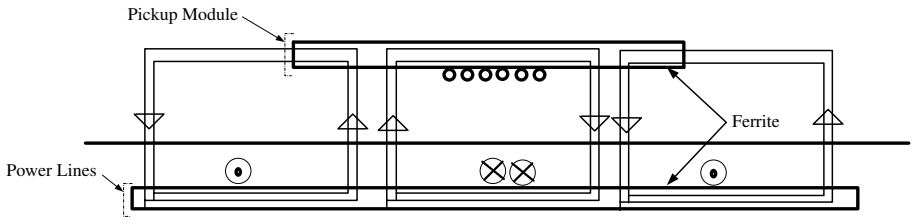

Fig 9.4 Horizontal magnetic flux type

9.4. Core Structures of OLEV

OLEV deployed in four generations termed as first, second, third and fourth, the general description are as follows [4]

9.4.1. 1st generation

The 1st generation of OLEV uses E-type core. Basically its structure is similar to E-type cored transformer. Primary core is E-type segmented structure with mechanical supporter, and secondary pick-up is conventional E-type structure. As a transformer, lateral misalignment of both cores severely degrades output power. This misalignment can happen frequently during driving if it were not for mechanical lateral position control for pick-up with 3mm accuracy. Using these structures, 80% system power efficiency is obtained at 1cm air gap. Data of monotype developed by OLEV are as follows. At primary side, the nominal frequency is 20 kHz and rated current is 100 A. At secondary side, rated load is 2 Ohm and 3 kW per pick up.

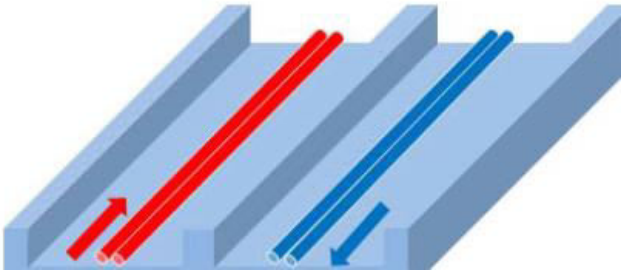

Fig 9.5 E core Type used in OLEV

9.4.2. 2nd generation

The air gap or lateral misalignment is large for the 1st generation of OLEV, so that the power efficiency sharply decreases. Since at least 12cm air gap is needed for freely driving

vehicles, the 1st generation of OLEV is not proper to actual road situations. To overcome this problem, the 2nd generation of OLEV is designed. Fig. 9.6 (a) shows primary coil and pick-up coil of the 2nd generation of OLEV. The distinction of the 2nd generation of OLEV is the direction of magnetic flux. For the ultra slim U-type mono rail structure, the direction of magnetic flux at center position is parallel to the ground and that at each end position has lots of fringe effect. As shown in Fig. 9.6 (b) the pole width of primary core (W_P) is much smaller than the length of pick-up coil so the effective pick-up width (W_{eff}) increases as the air gap increases. Therefore the magnetic flux transferred from primary coil to pick-up coil is proportional to the square root of the air gap.

Fig. 9.6 (c) shows the transferred magnetic flux, which is approximately proportional to the root of air gap. These effects make it possible to increase air gap from 1cm to 17cm. The big difference between the width of primary core (W_P) and the length of pick-up coil desensitize to the misalignment of primary coil and pick-up coil. As shown in Fig. 9.6 (c), the maximum allowable lateral misalignment is roughly the half of the length of primary core (W_C). The designed core structure makes it possible about 50% power transfer from primary coil to pick-up coil with 20cm misalignment as shown in Fig. 9.6 (c). So the 2nd generation of OLEV needs no mechanical control apparatus. The nominal frequency of power supply is 20 kHz, primary rated current is 200A, the rated load is 6 kW per pick-up and the total output power of 52 kW with 10 pick-ups and 72% power efficiency is accomplished at 17cm air gap. For efficiency calculation, all power losses between input power for inverters and battery stage at vehicles (inverter switching loss, rail, pick-up losses, regulator loss and so on) are considered. Power efficiency is very low when output power is small because of base power consumption, and is at maximum when output power is about 30 kW.

9.4.3. 3rd generation

In the 3rd generation of OLEV, by adopting fish bone like core structure depicted in Fig.9.7, the amount of core is reduced to 1/5th compared to the 2nd generation of OLEV, Where the output power is improved to 17 kW per pick-up. By adopting this structure, the concrete pouring method is now applicable. It means that the mechanical durability of primary coil is substantially increased. The decrease of magnetic flux transferred from primary coil to pick-up coil due to the bone structure is negligible.

9.4.4. 4th generation

The WPT technology for OLEVs developed in three generations requires a wide rail width to provide a large air gap, resulting in a strong EMF for pedestrians. Apart from the EMF problem, the allowable lateral displacement of the previous system was less than 20cm, which is too small to guarantee free driving by OLEVs. To solve these problems, a new system with a very narrow power supply rail width of 10cm and alternating polarity magnetic poles along the road is considered as shown in Fig. 9.8, where the name “I-type” stems from the front shape of the power rail. Each magnetic pole consists of ferrite cores, turned cables and the poles are connected to each other with ferrite cores. The polarity of B at each pole is reversed according to the current direction of each pole. Hence, the main magnetic flux is circulating through the nearest poles. A large air gap can be achieved by

arranging each pole in proper distance if necessary. Due to this alternating magnetic polarity of adjacent poles, the EMF for pedestrians around the power supply rail can be drastically reduced and this is a result of EMF cancellation by neighborhood poles with the opposite polarity. Large lateral displacement can also be achieved by the wide pickup, where a width as small as 80cm due to the narrow power supply rail of the proposed [5].

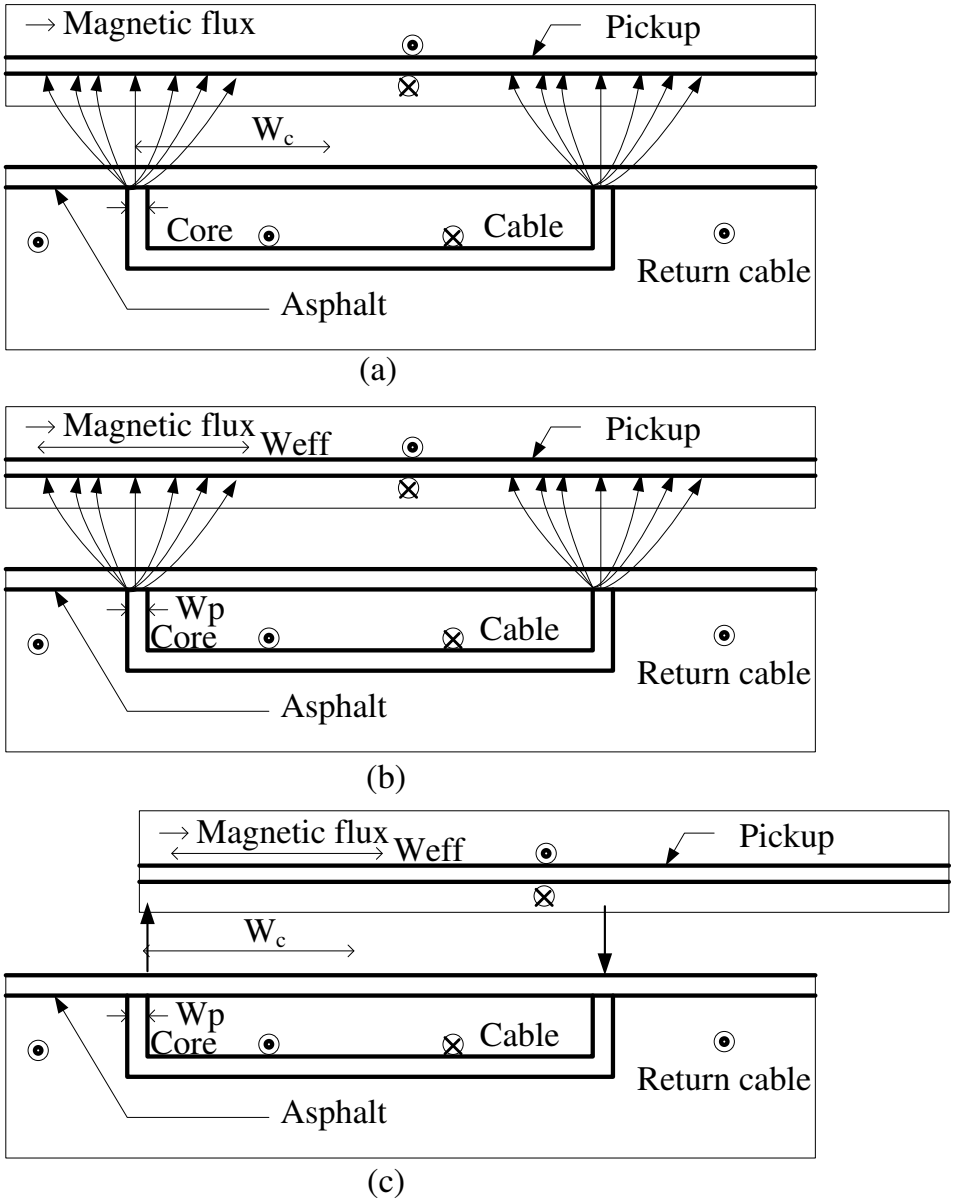

Fig 9.6 (a) second generation: (a) Ultra slim U-type primary coil and pickup coil (b) Effective pickup area with larger air gap (c) Maximum allowable misalignment

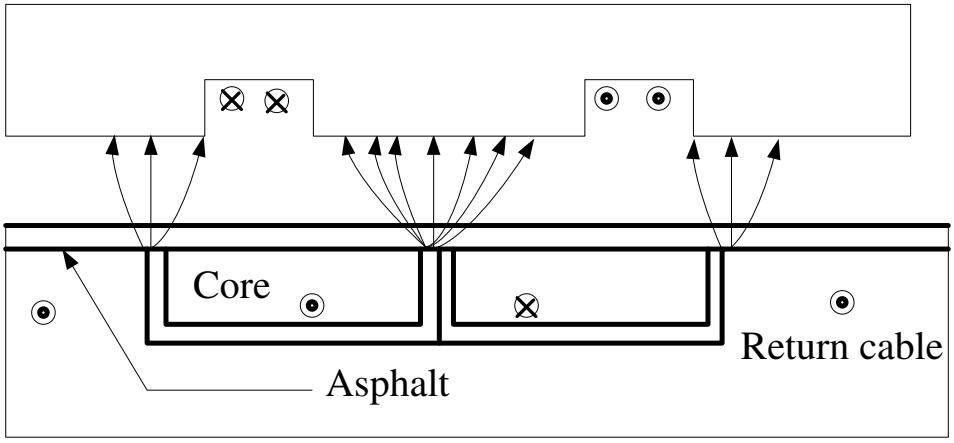

Fig.9.7 Ultra slim W type core structure

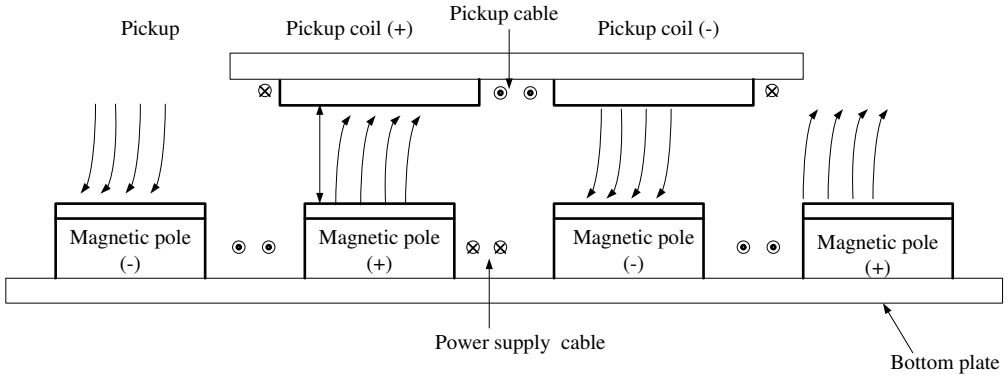

Fig 9.8 Concept of I-type core

9.5. Segmentation of power rails

The power line of the OLEV system is divided into several power line segments, as shown in Fig. 9.9. To mitigate inefficient power supply, the inverter turns on only the segment on which a vehicle is located. A sensor in a segment senses the approach of the vehicle and sends a message to the inverter, and then, the inverter turns the segment on. If the vehicle moves to the next segment, the inverter turns the previous segment off and the next segment on. This segment operation method reduces power loss in the cables. It also blocks EMF exposure to people on and near the powered road.

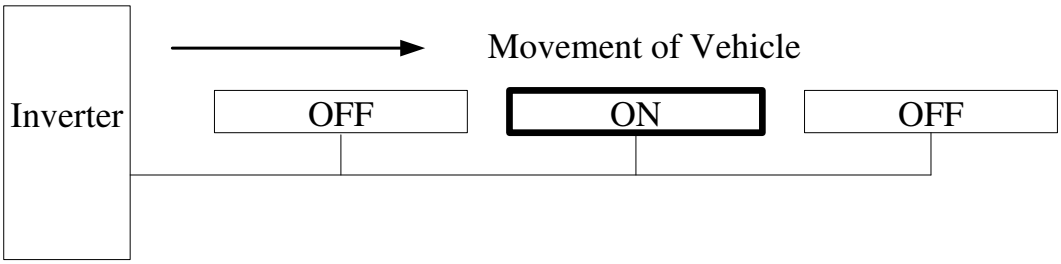

Fig 9.9 Concept of power line segmentation method.

There are two types of the segmented power supply rails, developed for the OLEV, one is the centralized switching type and the other is the distributed switching type. The centralized switching power supply rail consists of a few subrails, a bundle of supply cables and a centralized switch box, as shown in Fig.9.10 (a). The inverter is connected to one of several pairs of supply cables through the switch box at a time.

Assuming the inlet l_0 and the gap l_2 are much smaller than the length of a subrail l_1 , the total length of cables *lc* can be expressed as

$$l_c = n(n+1)l_1 \qquad (9.1)$$

where *n* is the number of subrails. One of the drawbacks of this method is that only a subrail can be activated by the inverter at a time. In the distributed switching power supply rail, as shown in Fig. 9.10 (b), the system is composed of a few subrails, a pair of common power supply cables, and multiple switch boxes. Based on the assumption that the inlet l_0 and the gap l_2 are much smaller than the length of a subrail l_1 , the total length of cables l_d for Fig. 9.10 (b) can be determined as

$$l_d = 2(2n-1)l_1 \qquad (9.2)$$

From (9.1) and (9.2), it is found that the total length of cable for the distributed switching segmentation can be reduced compared to the centralized one, i.e., $l_c \geq l_d$ for $n \geq 1$ and the reduction effect becomes significant for large *n*. For example, only 34.5% of cable is required for the distributed one when *n*=10. The distributed switching power supply rail, however, requires the common power supply cables which increase the construction cost and conductive power loss, where the cables are protected by the fiber reinforced polymer pipes. Regarding to the control capability of subrails, it still has the same problem as the centralized switching one.

As the remedy for the aforementioned problems, a new cross segmented power supply rail (X-rail) is proposed. The proposed X-rail consists of segmented subrails, auto compensation switch boxes, control signal lines, and roadway harnesses, as shown in Fig. 9.11. Furthermore, the inverter should be able to drive multiple road powered electrical vehicles (RPEVs). Regarding the bundle of two half-current-rating cables as a cable, for fair comparison, the total length of the cable *lx* is found, in a similar way of (9.1) and (9.2), as follows

$$l_x = 2nl_1 = \frac{l_d}{2} \qquad (9.3)$$

From (9.3), it is clearly identified that the cable cost of the proposed X-rail is nearly halved compared to the distributed switching segmentation of (9.2). The cable length reduction effect of the proposed scheme becomes severe as the number of segmented subrails increases.

In order to realize the X-rail, three versions of power rail types are considered. They are U-type core mono rail, W-type core dual rail and I-type core power rail [7], which have been developed since 2009 for OLEV. The detailed scheme of the W-type dual power supply rail, having two pairs of power cables, is shown in Fig. 9.12, which explains activation procedures of a subrail. The cross-sectional and top views of the dual rail in activation mode are shown in Fig. 9.12 (a), where the current directions of the cables in a bundle are same. Thus, appropriate magnetic flux is generated and passes through the pickup, whereas little magnetic flux is generated when the current directions of the cables in a bundle are opposite, as shown in Fig. 9.12 (b) and it is called silence mode.

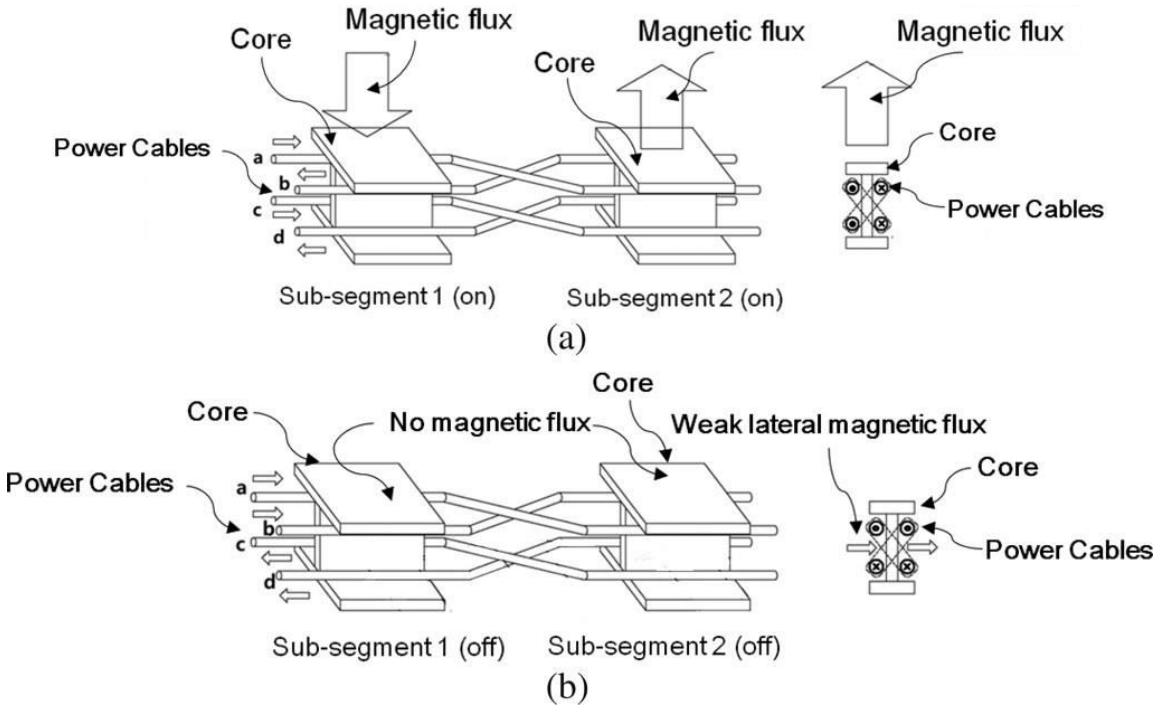

Fig 9.10 Segmentation of power rails (a) Centralized switching power supply rail (b) Distributed switching power supply rail

The switch box of the proposed X-rail should change the current direction of a cable of the bundle by controlled switches. Each switch box is controlled individually by its control signal, and the current direction of a pair of power cables is changed by the two sets of power switches; thus, the status of next subrail is changed accordingly. To get auto compensation capability against the inductance change of next subrails, a few capacitors and a coupling transformer are used. The inverter for the X-rail is assumed to be operating at the switching frequency *fs,* which is slightly higher than the resonant frequency *fr* of the X-rail. This frequency discrepancy makes the rail always inductive so that zero-voltage switching (ZVS) is guaranteed.

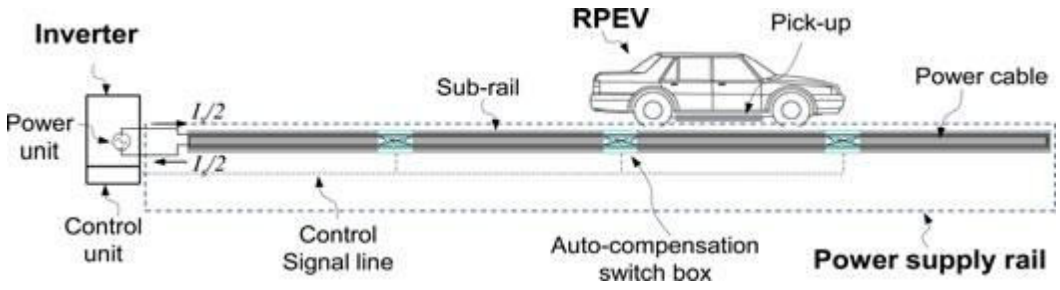

Figure 9.11 Concept of X-rail segmentation [7]

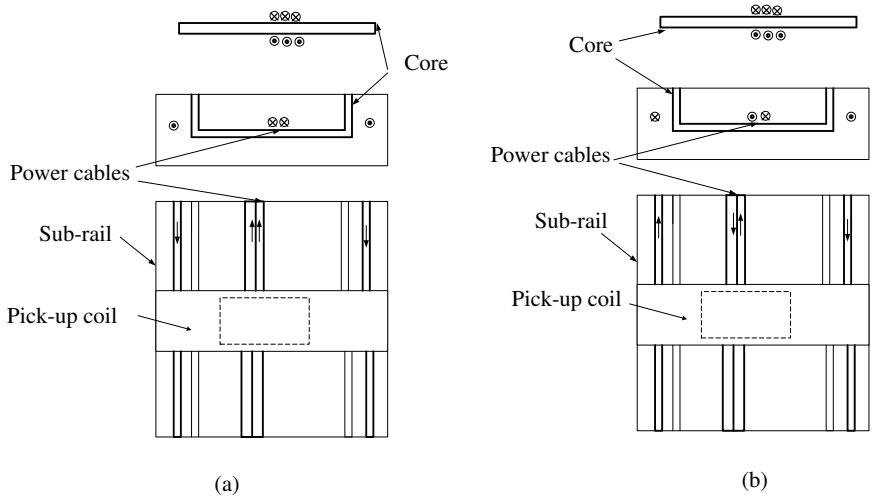

Figure 9.12. X-segmentation for mono-rail on activation and silence modes: cross sectional view (top) and plane view (below) (a) Activation mode (b) Silence mode

9.6. References

[1] N.P. Suh, D.H. Cho, and C.T. Rim, "Design of on-line electric vehicle (OLEV)," presented at the Plenary Lecture at the 2010 CIRP Design conference, Nantes, France, 2010.

[2] J. Huh and C.T. Rim, "KAIST wireless electric vehicles—OLEV," presented at the JSAE Annual congress, Yokohama, Japan, 2011.

[3] S. Ahn, et al, "Low frequency electromagnetic field reduction techniques for the On-Line Electric Vehicle (OLEV)," IEEE International Symposium on Electromagnetic Compatibility, 2010, pp. 625-630.

[4] S.W. Lee, J. Huh, C.B. Park, N.S. Choi, G.H. Cho, and C.T. Rim,"On-line electric vehicle using inductive power transfer system," Proc.IEEE Energy Convers. Congress Expo, 2010, pp. 1598–1601.

[5] J. Huh, S.W. Lee, W.Y. Lee, G.H. Cho and C.T. Rim, "Narrow-width inductive power transfer system for online electrical vehicles," *IEEE Trans.on Power Electronics*, vol. 26, no. 12, pp. 3666–3679, 2011.

[6] S. Choi, J. Huh, S. Lee and C.T. Rim, “New Cross-Segmented Power Supply Rails for Roadway Powered Electric Vehicles,” *IEEE Trans. on Power Electronics*, Vol. 28, no. 12, pp. 5832-5841, 2013.

[7] C. T. Rim, “The difficult technologies in wireless power transfer,” *Journal of KIPE*, Vol. 15, no. 6, pp. 32-39, 2010.

Chapter 10

Magnetic shielding

Summary

Magnetic shielding is emerging technologies of WPT system apart from the OLEV. This chapter discusses about magnetic shielding and techniques used for the mitigation of shielding effects.

10.1. Magnetic shielding in WPTS

The design of the magnetic field distribution is also a significant factor in a WPT system, particularly in a high-power transfer system. As a magnetic flux of more than thousands of mill tesla from the current of thousands of amperes is generated between the transmitter and receiver coils, even 0.1% of leakage from the main flux can be hundreds of milli tesla, which is several times larger than the magnetic flux regulation suggested by the International Commission on Non-Ionizing Radiation Protection [1]. Therefore, it is essential to control the leakage magnetic flux for a WPT applications.

The shielding will be mainly added under transmitter and above the receiver is important for the safe operation of WPT. Without shielding, following problems may occur: i) the magnetic field may interfere with the device or other objects, ii) may cause battery heating and iii) it may circulate current in metallic parts.

There are two basic methods for shielding against low to medium frequency magnetic sources which includes diversion of the magnetic flux with high-permeability materials [2] and the generation of opposing flux via Faraday's law [3]. Assuming the external medium is free space with $\mu=\mu_0$ and the shield is constructed of a ferromagnetic material having $\mu_r>>1$, the magnetic field will tend to concentrate in the low-reluctance ferromagnetic path, and as such will be diverted from affecting the free space region. To achieve this effect, the ferrite plate has to be thick enough, otherwise, the leakage flux into free space is considerable. An alternative is the mentioned above. is the field distribution when an aluminum sheet is attached to the ferrite plate. According to Faraday's law, a current circulates in the aluminum sheet and associated magnetic flux is generated. The induced magnetic flux is of a polarity or direction as to counteract the original incident magnetic field, and so the net magnetic field in the vicinity of the loop is reduced.

Fig.10.1, shows the magnetic flux lines behavior when without shielding case. From that, it can be observed that most of the magnetic flux lines are outside the secondary coil. Fig.10.2, shows the passive method of shielding, where ferrite cores are placed below the transmitter and above the receiver, from this method it can be observed that most of the magnetic flux lines are concentrated towards the receiver coil and the magnetic flux lines intensity reduced out of the receiver coil boundary. This method requires thick core structure which require high amount of core material which is more cost effective. To reduce cost and improve the magnetic field direction further, an aluminum is added to the existing structure,

the aluminum divert the magnetic flux lines within the boundary of transmitter and receiver. This behavior can be observed from Fig.10.3.

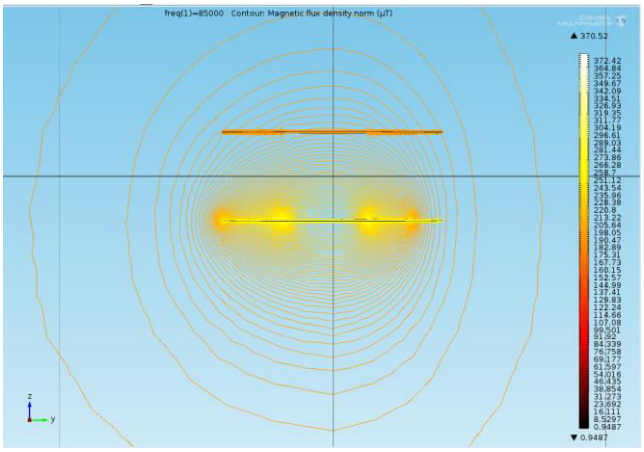

Fig.10.1. without shielding

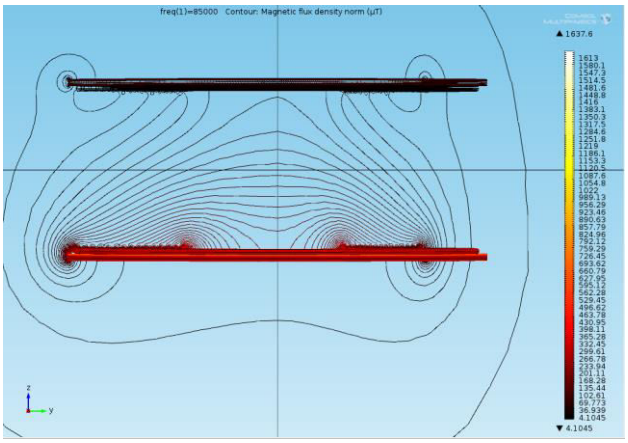

Fig.10.2. with shielding of ferrite (Passive shielding)

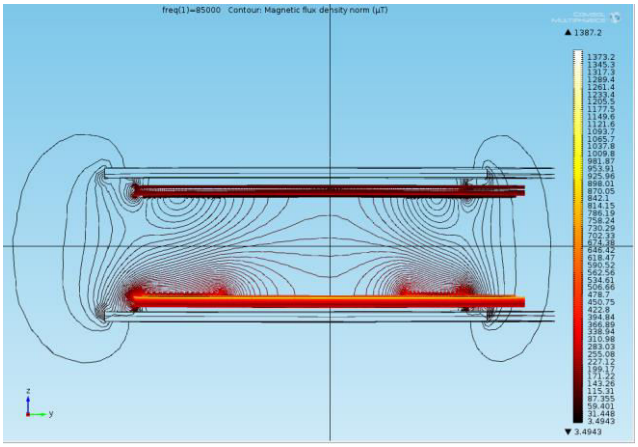

Fig.10.3. with Ferrite and Aluminum (active shielding)

10.2. References

[1]. J.Kim, S.jong, H.Kim and S.Y.Ahn, “Coil design and shielding methods for a magnetic resonant wireless power transfer system,” *Proc. IEEE*, vol. 101, no. 6, pp.1332 -1342, 2013.

[2]. C.Buccella and V.Fuina, “ELF magnetic field mitigation by active shielding,” Proc. IEEE Int. Sympoium on Industrial. Electronics, pp.994 -998, 2002.

[3]. M.L.Hiles and K.L.Griffing, “Power frequency magnetic field management using a combination of active and passive shielding technology,” *IEEE Transactions on power delivery*, vol. 13, no. 1, pp.171-179, 1998.

Chapter 11

Standards in WPT operation

Summary

In recent times, interest is growing in transferring energy at medium-high power between coils at a somewhat far distance. This, for instance, is the case of the wireless charging of the batteries of the electric vehicles (EVs). The following firms working for the development of WPT system for electrical vehicle

11.1. Firms working for WPT

11.1.1. KAIST and OLEV Technology

KAIST (formally Korean Advanced Institute of Science and Technology) has developed a method for wirelessly transferring power to busses. Their method consists of having two parallel conductors in segments, which are turned on only when a bus is driving over them. This protects from subjecting people around the power lines with magnetic field when no bus is near, and increases the efficiency. The receiver is put under the bus and is located 20 cm above the road, whereas the power lines in the road are placed 15 cm below the surface, resulting in a total distance of 35 cm. Because of the distance pickup modules need to be quite large (width of 80 cm) and several modules are needed to be able to make the transfer of 100 kW possible. The system is single phase and runs a 200 A current with the frequency 20 kHz and has an 80 % efficiency. Because of the continuous power transfer, for the case considered the need for batteries can de decreased to 20 % of an electric bus not capable of wireless charging. In addition, only part of the bus route needs to have these power lines and where there are none, the battery suffices. Together with OLEV (On line electric vehicle) technologies, this solution is being commercialized and now exists in a few places in South Korea [1].

11.1.2. Qualcomm Halo

Qualcomm Halo WEVC (Wireless electric vehicle charging) technology is based on years of internal investment along with decades of technical and commercial development by the University of Auckland, an acknowledged pioneer in wireless power transfer. The technical specifications are shown in Tab.11.1 [2].

Market status:

- Qualcomm and Delta Motorsport Announce Integration of Wireless Electric Vehicle Charging into Delta E-4 Coupé Electric Vehicles for London Trial
- Qualcomm Becomes Founding Technology Partner of FIA Formula E Championship

Table.11.1. Technical specifications of Qualcom Halo

Attribute	Specifications
Input voltage	240 V AC
Output voltage	300 V DC
Output power	3 kW
Physical separation	180mm+/-30mm
Lateral tolerance	+/- 150 mm
Efficiency	85%
Physical size	800mm*400mm*30mm
Output specifications	250 V to 300 V in 10 steps
Nominal resonant frequency	20 kHz

11.1.3. WiTricity corp

WiTricity Corporation designs, develops, manufactures, and markets patented technology for wireless energy transfer. Founded in 2007, the company is commercializing technology invented by a team of MIT physicists in 2006. The WiT-3300 Deployment Kit is a wireless "Park-and-Charge" self-charging system for electric vehicles. Technical specifications are as follows [3]

Table.11.2. Technical specifications of WiTricity Corp (WiT-3300)

Attribute	Specifications
Operating Frequency	145 kHz, nominal
Lateral Positional Tolerance	±20 cm in vehicle side to side axis ±10 cm in vehicle bumper to bumper axis
Output Power	DC: 300 watts-3.3 kilowatts, continuously variable
Output Voltage	DC: 350 VDC- 400 VDC at 3.3 kW, 18 cm resonator-resonator distance
Source Module Enclosure	50 cm x 50 cm x 3.75 cm; 12.5 kg
Capture Module Enclosure	50 cm x 50 cm x 3.75 cm; 12.5 kg
RF Amplifier Assembly	22 cm x 33 cm x 13 cm; 4.2 kg
On-Vehicle Rectifier Assembly	20 cm x 28 cm x 7 cm; 3.6 kg

Market Status: Commercialization of this technology is still under consideration. WiTricity working on setting up standards before they launch in the market. Recently Toyota inc. decided to adopt the Witricity technology for their newly developed cars

11.1.4. Delphi Wireless charging system

Delphi initially started devolvement of the WPT system in 2011 with its own specification of 3.3 kW output power with an input voltage range between 85 V to 265 V AC, 60 Hz supply [4]. Delphi Automotive has equipped several test vehicles in Munich. It has reached an agreement with WiTricity corp to develop automatic wireless charging products for hybrid and electric vehicles. The collaboration between the two companies will help establish a global infrastructure of safe and convenient charging options for EV.

11.1.5. Primove (Bombardier)

The innovative PRIMOVE system provides a wireless power source for all types of electric transport from light rail and bus networks to commercial vehicles and cars. PRIMOVE does not only work for wireless charging of busses, but also for cars and trams as well as. For busses, the planned stops are ideal locations for charging the batteries and can be distributed among the stops to minimize the need for way side infrastructure. If there is a steep hill along the bus route, additional dynamic charging sections can be installed to give extra energy and avoid the battery losing too much power. Using this solution for trams provides an extra bonus since no cable wires are needed and therefore do not cause any visual pollution. Just like with busses, a mix of static and dynamic charging works best, and minimizes the need for batteries and wayside infrastructure. PRIMOVE solution uses a three-phase system which is divided into segments to avoid unnecessary magnetic field around the roads and maximize its efficiency. An antenna is used to communicate with the road so that only the segments directly under the vehicle are on. The vehicle has a control unit which decides how to best utilize the power, for charging of the batteries, for propulsion or for both. PRIMOVE technology is already used in Augsburg, Lommel and Braunschweig [5]. Technical specifications are given in Tab.11.3.

Table.11.3. Technical specifications of PRIMOVE corp

Location	Augsburg	Lommel (Belgium)	Braunschweig
Vehicle considered	Bi directional low floor tram	1 Van Volvo bus, 1 C30 car	Solaris urbino 12 electric (12 m), and Solaris urbino18 electric (18 m)
Length of test track (route)	800 m	125 m	12 m and 18 m
Power supply network	750 V DC	400 V AC or 750 V DC	400 V AC or 750 V DC
Charging power	200 kW	40 kW & 80 kW (bus) and 22 kW (car)	200 kW
Power transfer efficiency	95 %	90%	90 % for both vehicles
Max speed	50 km/h	N/A	N/A

11.1.6. Oak Ride National Laboratories

ORNL researchers have made wireless power transfer more efficient by using an air core transformer loosely coupled to a storage battery. By reconfiguring the transformer and altering the resonance frequency, power is transferred to the battery with little energy loss and fewer demands on the primary circuit. The technology can be used for wireless charging of stationary electric vehicles in garages and parking lots or in-motion vehicles on the roadway [6]. They demonstrated and tested in a laboratory with 90-94% transfer efficiency at 25 cm airgap for 4 kW and research is targeted for high power range.

11.1.7. TBD

Siemens and BMW announced at Hannover 2011 that they will be testing a prototype that will use inductive energy charging to charge electric vehicles. EVs would be able to roll over charging stations and need not to plug in a cord, which would be ideal for service cars like taxi cabs because it works even during a short stop. The system therefore generates a magnetic field whose strength in and around the vehicle is far below the internationally recommended limit of 6.25 microtesla [7].

11.1.8. Plugless power

Plugless power manufactured by USA based firm providing wireless energy transfer for electrical vehicle specially designed for Chevrolet Volt and the Nissan Leaf. The technical specifications of the plugless power are below [8].

Table.11.4. Technical specifications of Plugless power

Attribute	Specifications
Input voltage	208/240 V AC
Output power	3.3 kW
Nominal gap	4” (10 cm)
Ground clearance	6.5” (16.5 cm)
On board weight	10 pounds to the weight of vehicle
Operating Temp	18 C to 50 C (0 to 122 F)
Efficiency	90%
Coil Type	Circular

11.1.9. Stanford university wireless charging

Stanford University researchers announced that they have designed a road-based, high-efficiency wireless charging system for electric vehicles. They used mathematical simulations to prove that by bending the copper coils at a 90 degree angle and attaching them to a metal plate, up to 10 kilowatts of electricity can be transferred at a efficiency of 97% [9].

Table.11.5. Competitive Differentiation

Product Name	Manufacturer	Relevance
OLEV	KAIST	Tested in grand Seoul park, Seoul, Korea, and its runs on inner city roads in Korea. This system is commercializing in more parts in south Asia is in progress
Qualcomm Halo	Qualcom Halo	This technology under deployment and running several test runs in all over world
WiT-3300	WiTricity	Toyota begins testing WiTricity technology
Delphi wireless charging system	Delphi Partner with startup WiTricity. WiTricity also engaged with Toyota	Sharply resonant magnetic coupling (not inductive), 3.3 kW across 20 cm air gap. Product is in development.
Tram, Van Volvo bus, C30, Solaris urbino	Bombardier	OEM wireless charging solution
ORNL Project	Oak Ride National Laboratories, USA .	90-94% transfer efficiency @25cm airgap;
TBD	Siemens & BMW	90% transfer efficiency @ 15 cm; for 3.6 kW; in development with prototypes deployed
Plugless Power	Evatran with partner Yazaki	PEV retrofit solution. 3.3 kW output with 90 % transfer efficiency claimed (earlier reports indicated 70%); product launched in April 2012. projected installed price is $ 5000
Stanford University Project	Stanford University	They proved mathematical analysis and implementation for highway systems is in devolpment stage

11.2. Standards for Wireless Power transfer for Electric Vehicle

11.2.1 Static WPT

11.2.1.1. Standards

a) IEC Standards

The following standards are being developed by IEC/TC69:

[1]. IEC 61980-1, Electric vehicle wireless power transfer (WPT) systems – Part 1: General requirements, is targeted for publication by February 2015.
[2]. IEC 61980-2, Electric vehicle wireless power transfer (WPT) systems – Part 2: specific requirements for communication between electric road vehicle (EV) and infrastructure with respect to wireless power transfer (WPT) systems, is targeted to have a committee draft (CD) available by the end of January 2015.
[3]. IEC 61980-3, Electric vehicle wireless power transfer (WPT) systems – Part 3: specific requirements for the magnetic field power transfer systems, is targeted for publication by January 2017.

b) SAE J2954 Standards

Since launching in late 2010, the taskforce has now grown to comprise six sub teams: Alignment and communications (in coordination with SAE Hybrid Communications and SAE DSRC committees and the US Department of Transportation (DOT)), testing and validation, verification of wireless charging regarding performance, safety, interoperability and communication, interoperability, WPT frequency determination and Bus wireless charging. There are a number of topics under the aegis of J2954, as follows

[1]. Classification of different charging types and minimum efficiency per charging type
[2]. Interoperability including center operating frequency of charging
[3]. Communications & software (harmonize with SAE conductive charging)
[4]. Validation testing (vehicle, charger, system)
[5]. Parking alignment between the vehicle secondary coil and the primary coil of the wireless charging unit (EV Supply Equipment, EVSE)
[6]. Location on vehicle and orientation of charger
[7]. Safety items, including obstacle detection, both organic and inorganic, magnetic field levels, charging battery state of charge levels and rate, temperature development tests and electric shock
[8]. Design validation test and wireless charging verification test.

A common frequency of operation for WPT is essential for interoperability. The SAE team has determined this nominal frequency of 85 kHz (81.38-90.00 kHz) for SAE J2954. This frequency lies within an internationally available frequency band. In addition, the SAE J2954 Team has also determined three power classes for light duty vehicles, WPT 1, 2 and 3. as 3.3 kW, 7.7 kW and 22 kW respectively. These limits are defined by the maximum input Wireless Power Transfer.

The SAE International Task Force is currently working on completing the remaining interoperability topics, including factors such as the minimum coupling factor "*k*", alignment, and coil geometries.

In addition, SAE J2954 is working together with UL (Underwriters Laboratories) to create a validation test and link the efforts for design validation (SAE J2954) to verification of safety and performance (UL 2750) of wireless charging. A jointly developed test fixture is under planning to provide a means for verification of performance (such as minimum efficiency with alignment) while keeping within safety limits (ICNIRP magnetic field levels, temperature limits).

IEC 61980-3 is analogous to SAE J2954. There will be an attempt to harmonize IEC 61980-2 and SAE J2954. ISO /TC 22/SC 21/WG1 is working on ISO PAS 19363, Electrically propelled road vehicles – Magnetic field wireless power transfer – Safety and interoperability requirements. UL 2750 is still in development on basic safety requirements. It will not be completed until the design documents SAE J2954 and IEC 61980 are finished. There is no specific target date for publication.

c) Communications in support of WPT

In terms of communications standards for wireless power transfer, relevant work in development includes: IEC 61980-2 SAE J2836/6™, Use Cases for Wireless Charging Communication for Plug-in Electric Vehicles, and SAE J2847/6, Wireless Charging Communication between Plug-in Electric Vehicles and the Utility Grid. Communications for wireless charging will use DSRC (Dedicated Short Range Communications). This is a coordinated effort between US DOT, SAE DSRC Committee as well as the SAE Communications Committee, and will open up numerous opportunities also for electric vehicle communications (V2Grid, V2V) as well as billing and smart grid, Schneider notes.

[1]. ISO 15118-6, Road vehicles - Vehicle to grid communication interface -- Part 6: General information and use-case definition for wireless communication
[2]. ISO 15118-7, Road vehicles - Vehicle to grid communication interface -- Part 7: Network and application protocol requirements for wireless communication
[3]. ISO 15118-8, Road vehicles - Vehicle to grid communication interface -- Part 8: Physical layer and data link layer requirements for wireless communication

Gap: Coordination of wireless charging communication standards. Automotive manufacturers do not want to support three separate activities dealing with the same issue. An initiative is underway to understand how the work can be done once or divided between ISO, IEC and SAE. There is no clear cut technology solution right now.

11.2.1.2. *Electromagnetic compatibility (EMC) in relation to wireless charging*

Issues related to wireless charging of electric vehicles include EMC measurement and immunity, safety from shock, and safety from human exposure to radio frequency (RF) radiated emissions. On-board or off-board charging may create disturbances to radio services. There also may be safety concerns for people who are in or next to an electric vehicle that is being charged through wireless power transfer.

The SAE J2954 task force is speaking with the Federal Communications Commission (FCC) about EMC and the Food and Drug Administration (FDA) about emissions absorption rates. The FCC has asked the SAE J2954 task force to coordinate closely with ANSI IEEE C63.4, an emission measurement procedure (and the FCC Measurement Procedure, MP-5). Work under SAE J2954 may lead to new procedures being referenced in ANSI IEEE C63.4. The IEC is also in discussion with the FCC. IEC/TC 106 addresses human exposure aspects.

Gap: Wireless charging. Standards and guidelines for wireless charging are still in development.

11.2.2 Dynamic WPT charging

IEEE has begun pre-standardization work on dynamic wireless charging. The communications requirements will be different than for stationary wireless charging.

[1]. To choose the minimum efficiency level, power level and frequency, the taskforce is investigating the ideal method to specify interoperable coil geometries. The taskforce is evaluating a number of options to accomplish this from specifying coils to creating a "magnetic coupling" performance test.

[2]. Proposed alignment methods that are being investigated include triangulated RFID positioning, magnetic coupling positioning, or combination positioning. The general principle of RFID positioning is to use signal strength by multiple RFID readers and tags to triangulate vehicle position.

[3]. One possibility for magnetic coupling positioning is to send a magnetic ping, the most sensitive secondary resonant circuit component is measured for voltage or current. Coupling coefficient estimation or "sweet spot" detection is used to determine relative magnetic alignment.

[4]. Another possibility is combination positioning which uses RFID to determine vehicle proximity or relative position, while magnetic coupling is used to help determine magnetic "sweet spot".

11.2.3. Industry involvement.

There is heavy involvement from industry and government in the effort. WPT suppliers include Conductix-Wampfler, Evatran, HaloIPT, Momentum Dynamics, LG, Qualcomm, Samsung, SEW and WiTricity. Other infrastructure companies include Better Place, NRG Energy and Southern California Edison. Auto OEMs participating include Audi, BMW, Chrysler, Coda, Daimler, Fisker, Ford, GM, Honda, Mitsubishi, Nissan, Phoenix and Toyota. Bus manufacturers Volvo and Proterra are also participating. Tier 1 suppliers in the mix include Delphi, Magna, Maxwell, Panasonic and Yazaki. Finally, government and research organizations involved include US Department of Energy (DOE) and its national labs (ANL, INL, ORNL, etc.), US Environmental Protection Agency (EPA), US Department of Transportation (DOT) and Energy Dynamics Laboratory (EDL), a government research institution and technology provider owned by the Utah State University Research Foundation. JARI (Japan), EPRI, KAIST (Korea), University of Tennessee, Underwriters Laboratories, TÜV North America and the California Department of Transportation are also involved.

11.3. References

[1] http://olev.kaist.ac.kr/en/ Accessed: 21/02/2014.

[2] http://www.qualcommhalo.com/ Accessed: 22/02/2014.

[3] http://www.witricity.com/pages/ev-charging-system.html Accessed: 22/02/2014.

[4] https://delphi.com/about/news/media/pressReleases/pr_2010_09_29_001/ Accessed: 22/02/2014.

[5] http://primove.bombardier.com/references/ Accessed: 22/02/2014.

[6] http://web.ornl.gov/adm/partnerships/events/Dec_Spark/Paulus_Wireless%20Power%20Transmission%20Presentation%20-%20Paulus%20v2.pdf Accessed: 22/02/2014.

[7] http://www.bmwblog.com/2011/04/15/bmw-and-siemens-partnering-for-wireless-charging-electric-vehicles/ Accessed: 22/02/2014.

[8] http://www.pluglesspower.com/go-plugless/ Accessed: 22/02/2014.

[9] http://www.stanford.edu/group/gcep/cgi-bin/gcep-research/all/safe-wireless-power-transfer-to-moving-vehicles/ Accessed: 22/02/2014.

Appendix - A

Ferrite and its properties

The difference in properties and performance of ferrites as compared with most other magnetic materials is due to the fact that the ferrites are oxide materials rather than metals. Ferromagnetism is derived from the unpaired electron spins in only a few metal atoms, these being iron, cobalt, nickel, manganese, and some rare earth elements. It is not surprising that the highest magnetic moments and therefore the highest saturation magnetizations are to be found in the metals themselves or in alloys of these metals. The oxides, on the other hand, suffer from a dilution effect of the large oxygen ions in the crystal lattice. In addition, the net moment resulting from ferromagnetic alignment of the atomic spins is reduced because a different, less efficient type of exchange mechanism is operative. The oxygen ions do serve a useful purpose, however, since they insulate the metal ions and, therefore, greatly increase the resistivity. This property makes the ferrite especially useful at higher frequencies [1]. This appendix mainly describes the comparison of ferrite with other magnetic materials and basic study of different core geometries.

A.1 Comparison of magnetic materials v/s ferrite

Tab.A.1 compares the different magnetic core material characteristics and Fig.A.1 shows the graph of characteristics of materials. As can be seen, the material that provides the highest flux density (supermendur) would result in the smallest component size, and tins would influence the choice if size were the most important consideration. Magnetic materials selected for transformers or inductors cannot be chosen by flux alone. There are other parameters, such as frequency and core configuration that must be taken into consideration.

TABLE A.1. Magnetic Core Material Characteristics [2]

Material Name	Composition	Initial Permeability (μ_i)	Flux density tesla (Bs)	Curie Temp (^oC)	DC coercive force H_C ostereds	Density grams/cm^3 δ
Magnesil	3% Si 97% Fe	1.5 k	1.5-1.8	750	0.4-0.6	7.3
Supermendur	49% CO 49% Fe 2% V	0.8 k	1.9-2.2	940	0.15-0.35	8.15
Orthonol	50% Ni 50% Fe	2k	1.42-1.58	500	0.1-0.2	8.24
Sq. permalloy	79% Ni 17% Fe 4% MO	12k-100k	0.66-0.82	460	0.02-0.04	8.73
Supermalloy	78% Ni 17% Fe 5% MO	10k-50 k	0.65-0.82	460	0.003-0.008	8.76
Amorphous	81% Fe	3k	1.5-1.6	370	0.03-0.08	7.32

2605-SC	13.5% B 3.5% Fe					
Amorphous 2714 A	66% CO 15% Si 4% Fe	20k	0.5-0.58	205	0.008-0.02	7.59
Ferrite	**MnZn**	**0.75-15k**	**0.3-0.5**	**100-300**	**0.04-0.25**	**4.8**

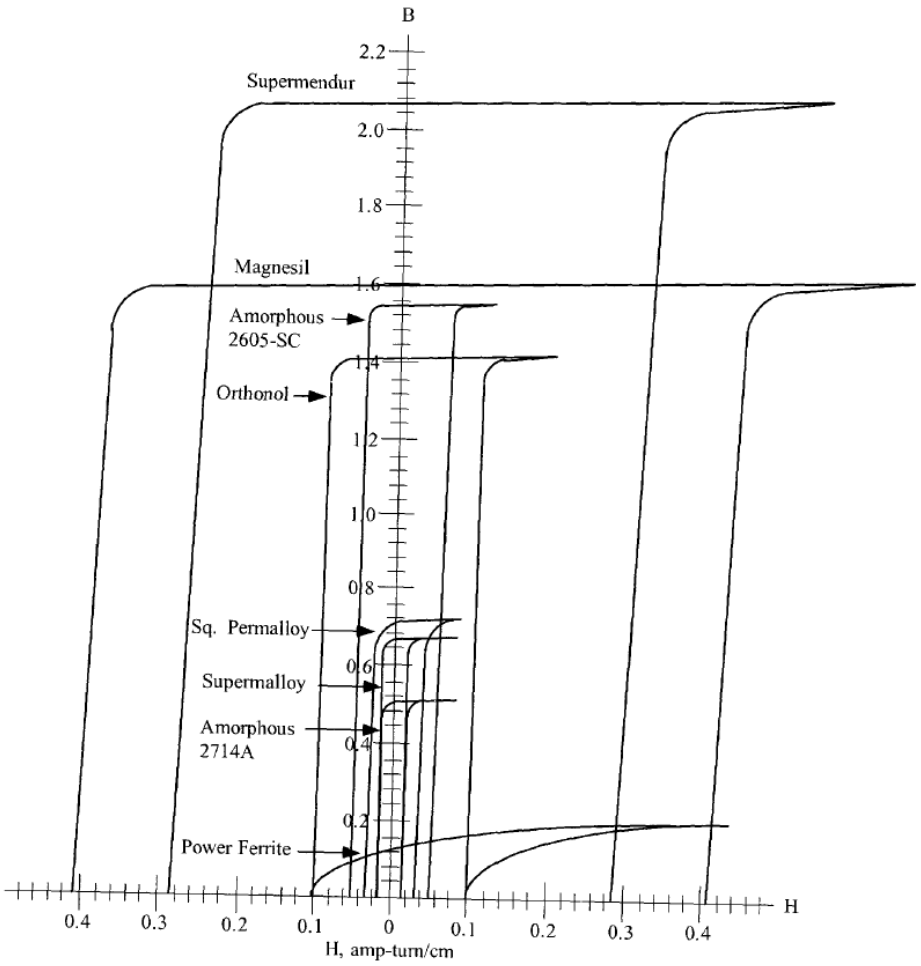

Fig.A.1. Magnetic core material characteristics [2]

Usually, inverter transformer design is aimed at the smallest size, the highest efficiency and adequate performance under the widest range of environmental conditions. Unfortunately, the core material that can produce the smallest size has the lowest efficiency and the highest efficiency materials result in the largest size. Thus, the transformer designer must make tradeoffs between allowable transformer size and the minimum efficiency that can be tolerated. Then, the choice of core material will be based upon achieving the best characteristic on the most critical or important design parameter, and upon acceptable compromises on the other parameters.

After analysis of a number of designs, most engineers choose size rather than efficiency as the most important criterion, and select an intermediate loss factor on core material for their

transformers. Consequently, as the frequency is increased, ferrites have become the most popular material.

At high frequencies, ferrites have substantial advantages over conventional metallic materials, either in lamination forming technology. Ferrites offer additional mechanical features as well. Ferrites can be shaped in a variety of different core geometries optimized for specific applications. For example, cores can be designed for ease of assembly, or made self-shielding where required.

A.2 Core geometries

A.2.1. Pot cores

Pot cores, when assembled, nearly surround the wound bobbin. This aids in shielding the coil from pickup of EMI from outside sources. Both plain and printed circuit bobbins are available as are mounting and assembly hardware. Because of its design, the pot core is a more expensive core than other shapes of a comparable size. Pot cores for high power applications are not readily available [3].

A.2.2. Double Slab and RM cores

Slab sided solid center post cores resemble pot cores, but have a section cut off on either side of the skirt. Large openings allow large size wires to be accommodated and assist in removing heat from the assembly. RM cores are also similar to pot cores, but are designed to minimize board space, providing at least a 40% savings in mounting area. The solid center post generates less core loss and this minimizes heat buildup.

A.2.3. E cores

E cores are less expensive than pot cores and have the advantages of simple bobbin winding plus easy assembly. Gang winding is possible for the bobbins used with these cores. Lamination size E shapes are available to fit commercially available bobbins previously designed to fit the strip stampings of standard lamination sizes. E cores can be pressed to different thickness, providing a selection of cross-sectional areas. Bobbins for these different cross sectional areas are often available commercially. E cores can be mounted in different directions and if desired provide a low-profile. Printed circuit bobbins are available for low-profile mounting. E cores are popular shapes due to their lower cost, ease of assembly and winding, and the ready availability of a variety of hardware.

A.2.4. EC, ETD and EER cores

These shapes are a cross between E cores and pot cores. Like E cores, they provide a wide opening on each side. This gives adequate space for the large size wires required for low output voltage switched mode power supplies. It also allows for a flow of air which keeps the assembly cooler. The center post is round, like that of the pot core. One of the advantages of the round center post is that the winding has a shorter path length around it (11% shorter) than the wire around a square center post with an equal area. This reduces the losses of the windings by 11% and enables the core to handle a higher output power. The round center post also eliminates the sharp bend in the wire that occurs with winding on a square center post.

A.2.5. PQ cores

PQ cores are designed especially for switched mode power supplies. The design provides an optimized ratio of volume to winding area and surface area. As a result, both maximum inductance and winding area are possible with a minimum core size. The cores thus provide maximum power output with a minimum assembled transformer weight and volume, in addition to taking up a minimum amount of area on the printed circuit board. Assembly with printed circuit bobbins and one piece clamps is simplified. This efficient design provides a more uniform cross-sectional area; thus cores tend to operate with fewer hot spots than with other designs.

A.2.6. EP cores

EP Cores are round center-post cubical shapes which enclose the coil completely except for the printed circuit board terminals. The particular shape minimizes the effect of air gaps formed at mating surfaces in the magnetic path and provides a larger volume ratio to total space used. Shielding is excellent.

A.2.7. Toroids

Toroids are economical to manufacture; hence, they are least costly of all comparable core shapes. Since no bobbin is required, accessory and assembly costs are nil. Winding is done on toroidal winding machines. Shielding is relatively good.

A.3 References

[1]. www.astro.uvic.ca/~tatum/elmag/em12.pdf. Accessed online : 01/09/2014.
[2]. http://nptel.ac.in. Accessed online: 29/08/2014.
[3]. http://www.mag-inc.com/products/ferrite-cores/ferrite-shapes: Accessed online :05/09/2014.

Appendix - B

Electric city car

B.1 Introduction

An electric mini-car, called Biro and produced by Estrima, is considered as a case of study and platform for the experimental verification of the WPT systems. The WPT under design is aimed at charging the battery of the two-seat electric city car shown in Fig. B.1. The car is supplied by a 48V lead battery pack, formed by four modules of 12 V connected in series. Two in-wheel motors are fitted in the rear wheels, each of them propelling the car with a rated power of 2 kW. Maximum speed and average range of the car are 50 km/h and 50 km, respectively. Nominal battery capacity is 100 A·h and nominal charging current during the constant current stage is 10 A. Being the battery voltage in full charge condition equal to 56 V, the power injected into the battery at the end of the constant current charging stage is 560 W

Electric city car [1]

B.2 Storage system in mini-electric car

Electric mini car under consideration uses four LPC12-100 (12V, 100Ah) Valve Regulated Lead Acid (VRLA) batteries as an energy source. LPC12-100 contains 6 cells connected in series with the nominal voltage of 2V. Each cell and hence the battery has defined lower and upper threshold values for the terminal voltages. As for the present case during the discharge, if terminal voltage of the battery falls below 36V, supply should be disconnected from the load. Similarly in the case of charging or regenerative braking if terminal voltage rises above 56V battery should be disconnected from the charger or load.

B.3 References

[1] M.Bertoluzzo, G.Buja, G.Pede and A.Puccetti, “Hybrid battery-supercapacitor storage system for electric city cars”, Proc. of European Electric Vehicle Congress (EEVC), CD, no. 2284905, 2011, pp. 1-8.

Appendix – C

Inductive sensing

C.1. Introduction to inductive sensing

An inductive sensor is an electronic proximity sensor, which detects metallic objects without touching them. The sensor consists of an induction loop. Electric current generates a magnetic field, which collapses generating a current that falls asymptotically toward zero from its initial level when the input electricity ceases. The inductance of the loop changes according to the material inside it and since metals are much more effective inductors than other materials the presence of metal increases the current flowing through the loop. This change can be detected by sensing circuitry, which can signal to some other device whenever metal is detected. Common applications of inductive sensors include metal detectors, traffic lights, car washes, and a host of automated industrial processes. Because the sensor does not require physical contact it is particularly useful for applications where access presents challenges or where dirt is prevalent.

Inductive sensing works by establishing a resonant circuit that uses the inductance of a coil and capacitor. Once a metal object is sensed, the resonant frequency is altered. The focus of the technology is on applications that need to detect moving parts prevalent in such sectors as industrial, automotive, medical, white goods, and consumer. These applications typically use Hall sensors, which require expensive magnets, and that have inherent drift challenges over time and temperature.

The LDC1000 shown in Fig.1. uniquely combines all of the external circuitry on chip that is normally required to simultaneously measure the impedance and resonant frequency of an LC resonator. It then regulates the oscillation amplitude in a closed loop to a constant level, while it monitors the dissipated energy of the resonator. This leads the accurate measurement of inductance of the front-end LC circuit, which enables precise measurement of linear/angular position, displacement, motion, compression, vibration, metal composition and new applications which will be conceived by designers. All of this can be done in the presence of oil, dust, dirt and moisture unlike most other solutions [1].

Inductive sensors can detect metal objects without touching them. They are sometimes used as a proximity detector or position sensor in factory automation and other areas. The operating principle is the use of a coil and an oscillator to create a magnetic field surrounding the sensing surface. The metallic object or “actuator” causes a dampening of the amplitude of the oscillation which can be used and detected in various ways to manage, position and control a process. Inductive sensing technology enables precise measurement of linear/angular position displacement, motion, compression, vibration, metal composition, and many other applications in markets [2].

C.2. How do LDCs enable inductive sensing?

An alternating magnetic field is generated by an oscillating LC tank; when a conductive material comes in the vicinity of the tank, eddy currents are generated in the metal or

conductor. This creates losses in the tank and also changes the total inductance of the system. Using the LC tank as a sensor, LDCs measure both the losses and the oscillation frequency of the tank. Losses in the tank are measured in terms of a resistor parallel to the coil, the parallel resonance impedance (Rp). The oscillation frequency of the tank is used to measure inductance.

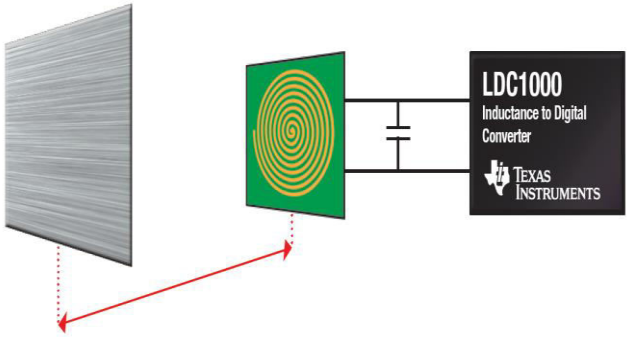

Fig.10.1. LDC 1000 Inductance to digital converter

C.3. Advantages of LDC1000

- Enables sub-micron resolution in position-sensing applications with 16-bit resonance impedance and 24-bit inductance values
- Offers contactless sensing that is immune to nonconductive contaminants such as dirt and dust
- Allows the sensor to be located remotely from the electronics, where PCBs cannot be placed
- Uses low-cost sensors and targets so no magnets required
- Supports pressed foil or conductive ink targets, offering endless opportunities for creative and innovative system design
- Consumes less than 8.5 mW during standard operation and less than 1.25 mW in standby mode.

C.4. Specifications of LDC 1000

Inductive sensing uses the oscillation frequency and oscillation amplitude and their values are 5 kHz to 5 MHz and 1,2,4 V_{PP} respectively.

Eddy current losses (RP) measurement	Inductance (L) measurement
• Range: 798 Ω to 3.93 MΩ • RP resolution: 16-bit	• L resolution: 24-bit • Maximum output data rate: 78 kHz • Supply current: 1.7 mA • Package: SON-16 • Interface: SPI

C.5. References

[1]. http://en.wikipedia.org/wiki/Inductive_sensor (online), Accessed on 02/12/2014.

[2]. http://www.ti.com/lit/ml/slyb212/slyb212.pdf (online), Accessed on 02/12/2014.

List of Publications

Peer-reviewed International conferences (IC):

[1]. M.Bertoluzzo, **K.N.Mude** and G.Buja, "Preliminary investigation on contactless energy transfer for electric vehicle battery recharging", Proceedings of IEEE International Conference on Industrial and Information Systems (ICIIS), pp.1-6, 2012.

[2]. **K.N.Mude,** M.Bertoluzzo and G.Buja, "Design of contactless battery charger for electrical vehicle", Proceedings of IEEE International Conference of AFRICON 2013, pp.1091-1096, 2013.

[3]. M.Bertoluzzo, and G.Buja and **K.N.Mude,** "Characteristic Evaluation of Wireless Battery Chargers for Electric Vehicles", Proceedings of 10th Jubilee International Symposium on Advanced Electromechanical Motion Systems, 21-22 October 2013.

[4]. **K.N.Mude**, M.Bertoluzzo and G.Buja, "Inductive Characteristics of Different Coil-Coupling Set-ups for Wireless Charging of an Electric City-Car," Proceedings of IEEE IEVC 2014, 2014, pp.1-7.

[5]. **K.N.Mude**, H.Dashora, M.Bertoluzzo, and G.Buja, "From Wired to In-moving Battery Chargers for Electric Vehicle", Proc.of DEEE'14, 2014, pp.33-40.